POLITECNICO
MILANO 1863

SCUOLA DI INGEGNERIA INDUSTRIALE
E DELL'INFORMAZIONE

Modelling of plasma facing component thermal response to runaway electron impact

Tesi di Laurea Magistrale in
Nuclear Engineering - Ingegneria Nucleare

Author: **Tommaso Rizzi**

Student ID: 993817
Advisors: Alessandro Maffini (PoliMi) & Svetlana Ratynskaia (KTH) & Panagiotis Tolias (KTH)
Academic Year: 2022-23

Abstract

The achievement of limitless clean energy production by means of nuclear fusion has fascinated the scientific community for more than half a century. Decades of combined theoretical and experimental work have been dedicated to confine a plasma in which the fusion reactions are self-sustained; facing and suddenly overcoming some of the most arduous challenges ever taken on. With the upcoming realization of the ITER project, mankind has never been so close to succeed, despite many technical and engineering problems awaiting to be solved.

Among those, runaway electrons represent one of the most biggest threats to the integrity of the plasma facing components of tokamak fusion devices. In fact, these high energy electron beams, generated in the course of the evolution of plasma instabilities, eventually impact the containing vessel leading to extreme heating and strong temperature gradients. The kinetic energy of runaway electrons is large enough to guarantee deep penetration and volumetric energy deposition. Deep melting, splashing or explosive material detachment might follow seriously compromising the life-time and power handling capabilities of these sensitive components.

This thesis project aims at developing a rigorous flexible tool to simulate, through Monte-Carlo (MC) transport methods, runaway electron energy deposition inside condensed matter. The physics involved in describing the interactions of primary and secondary particles is intricate and therefore deserves a proper validation activity against the most accurate experimental data to avoid inaccuracies.

In parallel to the benchmarking tests, applications to real case scenarios are presented, which concern the controlled exposure of a graphite dome to runaway electrons produced in the DIII-D tokamak. In particular, the consistency of the predicted temperature profile and vaporization losses with experimental observations is reported.

Keywords: nuclear fusion, runaway electrons, Monte Carlo transport, energy deposition, electron backscattering

Abstract in lingua italiana

L'idea di produrre energia pulita e rinnovabile tramite la reazione fisica nota come fusione nucleare ha affascinato la comunità scientifica ormai per più di metà secolo, rappresentando una delle più ambite soluzioni al problema dell'approvvigionamento energetico. Per decenni molteplici campagne sperimentali si sono susseguite con lo scopo di realizzare macchine per il confinamento del plasma e la creazione di un sistema auto sostenibile di reazioni di fusione, affrontado sfide tecnologiche tra le più ardue mai intraprese. Con l'imminente realizzazione del progetto ITER, l'uomo non è mai stato così vicino al raggiungimento di tale obiettivo, nonostante le complessità ingegnerestiche da risolvere siano ancora numerose. Tra queste, il problema dei *runaway electrons* rappresenta uno degli ostacoli maggiori nella realizzazione dei componenti strutturali che confinano il plasma nelle macchine con configurazione a tokamak. Infatti, fasci di particelle cariche ad alte energie, generati a seguito di instabilità nel plasma, rischiano di impattare sui materiali da confinamento, causando notevoli carichi termici e gradienti di temperatura. La componente cinetica di questi elettroni è elevata a tal punto da penetrare nel profondo richiedendo un'analisi 3D per comprendere come l'energia sia depositata. Tra le principali conseguenze si trovano lo scioglimento, l'esplosione o l'evaporazione con il rischio di compromettere irrimediabilmente la vita di questi delicati componenti.

Questo progetto di tesi si pone l'obiettivo di sviluppare uno strumento rigoroso ma flessibile, basato su metodi Monte-Carlo, per simulare il trasporto di elettroni ad alte energie all'interno della materia solida, prevedendo una mappa di energia depositata tridimensionale. La fisica che descrive interazioni di particelle primarie e secondarie risulta vasta e complicata, richiedendo pertanto un opportuno lavoro di validazione, tramite confronto con i più affidabili dati sperimentali presenti in letteratura.

In parallelo a questa attività di benchmarking, vengono presentate anche applicazioni a casi concreti, con lo scopo di ottenere profili di temperature e stime di perdite per evaporazione, in particolare relativamente al campione di grafite esposto al plasma del tokamak DIII-D.
Parole chiave: fusione nucleare, metodi Monte-Carlo, analisi comparativa, deposito di energia

Contents

Introduction

Since the very early days of industrial revolution, the problem of energy supply has been a key aspect for progress and development of the human society. For centuries, the main power source is represented by coal, a fossil fuel with a low thermal capacity but a moderate cost of processing as well as significant availability and accessibility. However, the environmental impact brought by the massive use of fossil fuels is today one of the main factors responsible for anthropological climate changes, which are leading to dramatic effects in daily life (global warming) and with even more drastic scenarios predicted for the future years, unless a serious and determined action is followed to invert this trend.

A lot has been done already in this direction and the locution "green transition" has become a key word in most of the new scientific research and industrial investment, to develop a society able to coexist and respect the planet. A focal aspect in this evolution is represented by renewable sources of energy, characterized by a very reduced environmental impact in terms of CO_2 emissions and air pollution. Despite a massive effort to install "green" sources of power like solar and wind energy, the target of net zero emissions remains a distant goal. That is why, in the last decades, the scientific research focused on a new possible way to produce "clean" energy in a massive and non intermittent way, using the reaction known as nuclear fusion, where two lighter atoms react creating an heavier atom and releasing heat in terms of kinetic energy of a secondary product (usually a neutron). Several possible elements can serve as the fuel for nuclear fusion, even though the most famous and interesting is the deuterium-tritium (D-T) reaction. The viability of such a physical process exploitable to produce "green" energy has to face a large number of physics problems, technical complexities and engineering issues, which make it one of the biggest challenges mankind has ever dealt with. Power exhaust, specifics of the materials, blanket and first wall, RAMI (Reliability, Availability, Maintainability and Inspectability) represent all examples at the heart of fusion community research.

Despite a large number of fusion machines operating today under experimental conditions, the path to demonstrate the feasibility of nuclear fusion as a renewable source of energy is still long and circuitous. More than 40 years of R&D will culminate with the construction and operation of an experimental reactor, called ITER (International Thermonuclear

Experimental Reactor) that will provide invaluable experience for the licensing and operation of future fusion power plants while the realization of DEMO (DEMOnstration Power Plant) will open the way to an industrial and commercial exploitation.

However, the road is still long and to achieve such an ambitious goal a vast amount of obstacles need to be overcome. This thesis project aims at being a useful contribution to the fusion research community, providing a new reliable and rigorous tool for predictions of plasma induced damage on structural components of the operating devices; today one of the most hostile problems to be tackled. The work is structured into six chapters: an introductory chapter where the basis of nuclear fusion are discussed and the problem of runaway electrons is introduced, a central body (chapter 2,3,4 and 5) where a physics background is provided, the methodologies are analyzed, the code validation is reported and an application to a real case scenario is shown, the final chapter where the results are summarized and a future outlook is provided.

1 | Background and motivation

This chapter begins with a general introduction to the field of nuclear fusion for energy production, describing the current status of fusion devices, their basic classification (in terms of confinement method and magnetic field configuration) and their main working principles. Next, the issue of long preservation of the integrity of plasma-facing components is presented, which constitutes one of the most complex challenges to be addressed in the path towards realization of nuclear fusion energy from tokamaks. Then, the problem of runaway electrons and associated volumetric heat deposition is discussed along with experimental evidence of the respective damage inflicted to the vessel. Moreover, the current state-of-the-art regarding available predictive models of runaway electron induced damage is briefly examined. Finally, the goals of this project are explained together with the expected outcomes.

1.1. Nuclear Fusion

In the interior of the sun and in the other stars, energy is constantly generated through nuclear fusion reactions, which have inspired the vision of a power-producing fusion reactor based on controlled thermonuclear reactions for more than half a century.

Atomic nuclei consist of protons and neutrons, but their mass is in general less than the sum of the individual masses of their constituents. This "mass defect", which can be converted to energy according to Einstein's equation $E = mc^2$, represents the energy required to disassembly the nucleus into its nucleons. Fig.1.1 summarizes the binding energies normalized with respect to the total number of nucleons, $\epsilon = E/A$, for all known elements as a function of their mass numbers. The fusion of light elements such as hydrogen isotopes (H, D and T) and helium (He^3) with low binding energy into heavier elements leads to the release of the energy represented by the mass defect.

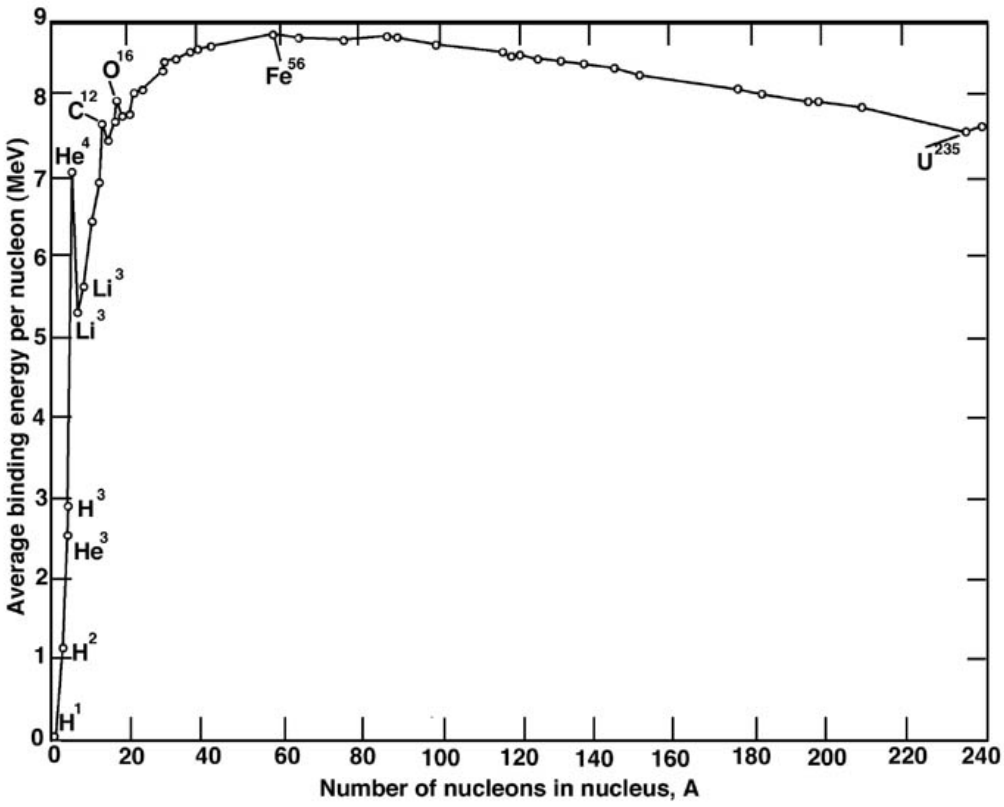

Figure 1.1: Average binding energy per nucleon as function of the number of nucleons. Adopted from Ref.[1].

There are several possible fusion reactions which might be employed for a sustainable energy production, namely the deuterium-tritium reaction (D-T), deuterium-deuterium re-

action (D-D), deuterium-helium three reaction (D-He^3) and the reactions involving boron and lithium. The fusion reactions are expressed as follows [2]:

- **D-T** $D + T \longrightarrow \alpha(3.5\,\text{MeV}) + n(14.1\,\text{MeV})$
- **D-D** $D + D \longrightarrow T(1.01\,\text{MeV}) + p(3.02\,\text{MeV})\ (50\%)$
- **D-D** $D + D \longrightarrow^3 He(0.82\,\text{MeV}) + n(2.45\,\text{MeV})(50\%)$
- **D-^{3}He** $D +^3 He \longrightarrow \alpha(3.6\,\text{MeV}) + p(14.7\,\text{MeV})$
- **B-p** $p +^{11} B \longrightarrow 3\alpha(8.7\,\text{MeV})$
- **Li-n** ${}^6_3Li + n \longrightarrow T + \alpha + 4.8\,\text{MeV}$
- **Li-n** ${}^7_3Li + n(2.5\,\text{MeV}) \longrightarrow T + \alpha + n$

where α denotes a charged helium ion ($^4He^{2+}$), p a proton and n a neutron. However, the conditions for such fusion reactions are very harsh, in fact two positively charged nuclei need to overcome the Coulomb repulsion to approach a sufficiently close distance of around 10^{-15}m, requiring a fuel kinetic temperature of around 10 to 100 keV, corresponding to 100 to 1000 million Kelvin. Fig.1.2 shows the thermal fusion reactivity $\langle\sigma v\rangle$ against the ion temperature, for the previously described fusion reactions. The D-T reaction has a higher cross-section at lower temperatures, which makes it the most considered for power plant applications. However, this one is not necessarily the most desirable due to the production of a 14.1 MeV neutron, which leads to neutron activation and hardening in the surrounding materials.

In 1955, J.D.Lawson summarized a list of necessary physical conditions to build a self-sustainable fusion machine [3]. He defined the energy gain Q as the ratio between the energy released by fusion events and the total energy given to the system to heat the fuel and sustain the fusion chain reactions. He concluded that Q needs to depend on the fuel temperature T as well as the product of the fuel density n and the confinement time τ ($n\tau$ is also known as Lawson parameter). Moreover, a fusion plasma that is self heated by charged fusion products, exceeding all the losses, is stated to have achieved the ignition condition. A precise temperature and Lawson parameter are required, constituting the Lawson criterion, declassified and published in 1957 [4]. Achieving high values for the combination of T, n and τ marks the distance of a given fusion experiment to the ideal gain condition. A mathematical and physical derivation of the Lawson criterion can be found in [5], where multiple definitions of gain used nowadays by researchers are provided.

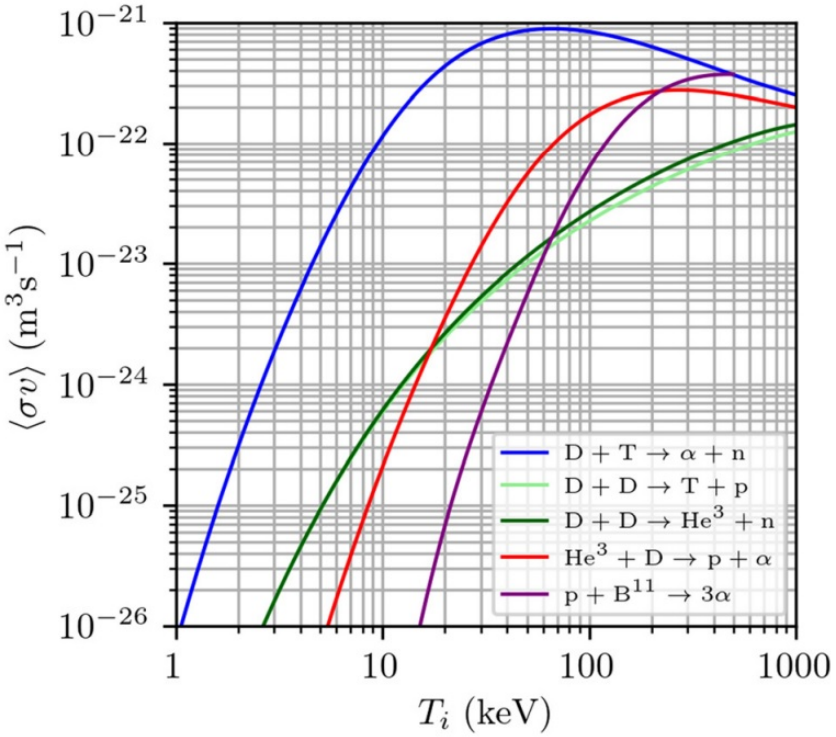

Figure 1.2: Thermal fusion reactivities vs. T_i, from [5]

1.2. Tokamak configuration

There are three basic ways through which plasma confinement can be achieved: *gravitational confinement*, only happening in stars, *magnetic confinement*, exploiting the Lorentz force acting on charged particles, and *inertial confinement* compressing the fuel to very high temperature and density for a relative short amount of time during which fusion reactions take place. The experimental configurations that are capable of reaching sufficient T and $n\tau$ are indeed laser driven inertial confinement fusion (ICF) and tokamak-based magnetic confinement fusion (MCF), even though several more set ups have been studied and successfully built such as the stellarator [6, 7], spheromak [8] or magnetic mirror [9]. The progress registered in the past six decades has been summarized in Fig.1.3 and Fig.1.4, where the most relevant fusion experiments, according to the implemented configuration, are reported in terms of the inferred Lawson parameter.

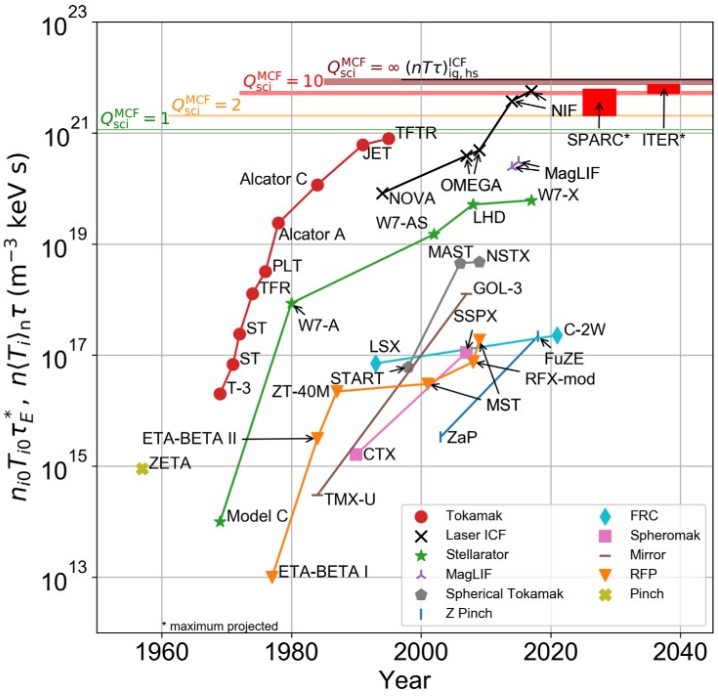

Figure 1.3: Triple products ($n_{i0}T_{i0}\tau_E$ for MCF and $n\langle T_i\rangle_n$ for ICF) that set a record for a given concept vs year achieved, illustrating the progress towards energy gain for different concepts. The horizontal lines labeled Q_{sci}^{MCF} represent the minimum required triple product to achieve the indicated values of Q_{sci}^{MCF}. The horizontal line labeled $(n\tau T)_{ig.hs}^{ICF}$ represents the required triple product to achieve ignition in an ICF hot spot, assuming $T_i = 4$ keV. The projected triple-product ranges for SPARC and ITER are bounded above by their projected peak triple products and below by the stated mission of each experiment. Adopted from Ref.[5].

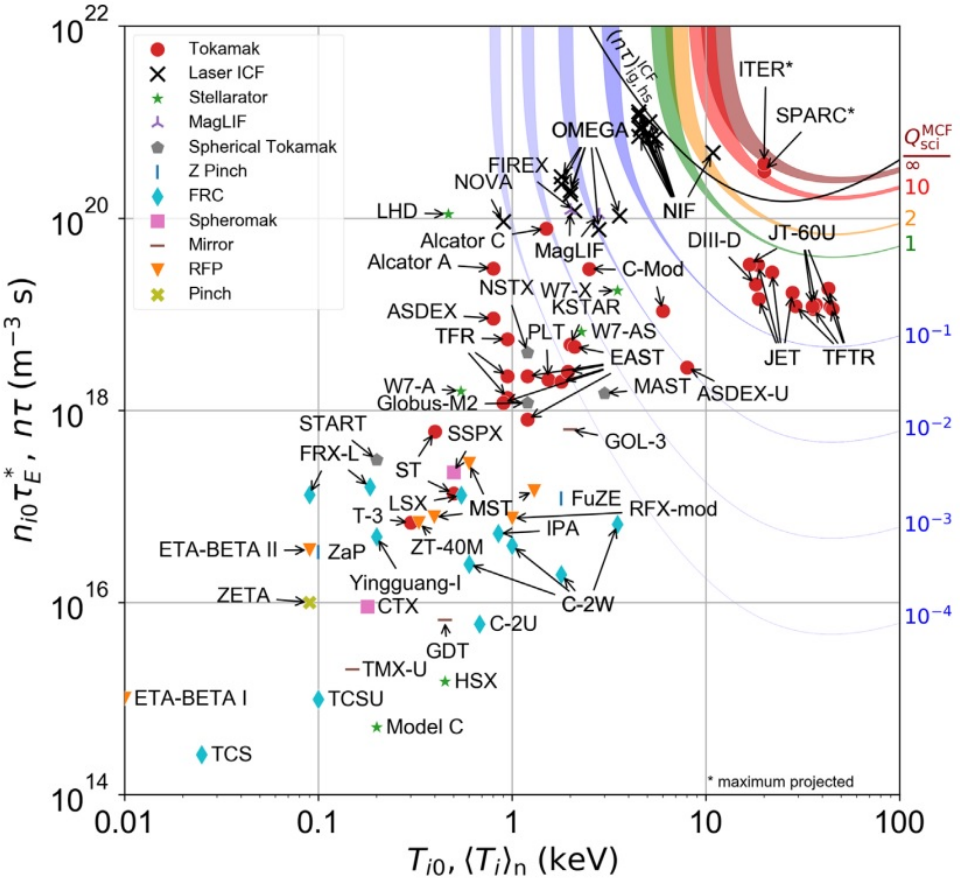

Figure 1.4: Experimentally inferred Lawson parameters ($n_{i0}\tau_E$ for MCF and $n\tau$ for ICF) of fusion experiments vs. T_{i0} for MCF and $\langle T_i \rangle_n$ for ICF, extracted from the published literature. The colored contours correspond to the Lawson parameters and ion temperatures required to achieve the indicated values of scientific gain Q_{sci}^{MCF} for MCF. The black curve labeled $(n\tau)_{ig.hs}^{ICF}$ corresponds to the Lawson parameters and ion temperatures required to achieve hot-spot ignition for ICF. D-T fuel is assumed while for experiments that do not use D-T, the contours represent a D-T-equivalent value. The finite widths of the Q_{sci}^{MCF} contours represent a range of assumed impurity levels. Adopted from Ref.[5].

In this section, the tokamak configuration is addressed more in details, being the reference technology for the development of this thesis. While ICF works primarily in a pulsed way, through microexplosions of reactant targets induced by high power laser or particle beams, in MCF charged plasma particles are trapped away from material walls through a specific magnetic field configuration. Among all the concepts that have been developed in past years, the tokamak layout is recognized to be the most successful. Plasma is shaped in the form of a torus thanks to the combination of a toroidal magnetic field, produced by a set of ring-like coils, and a poloidal magnetic field, turning around on the minor cross-section of the torus. A clarifying example of this configuration is reported in Fig.1.5.

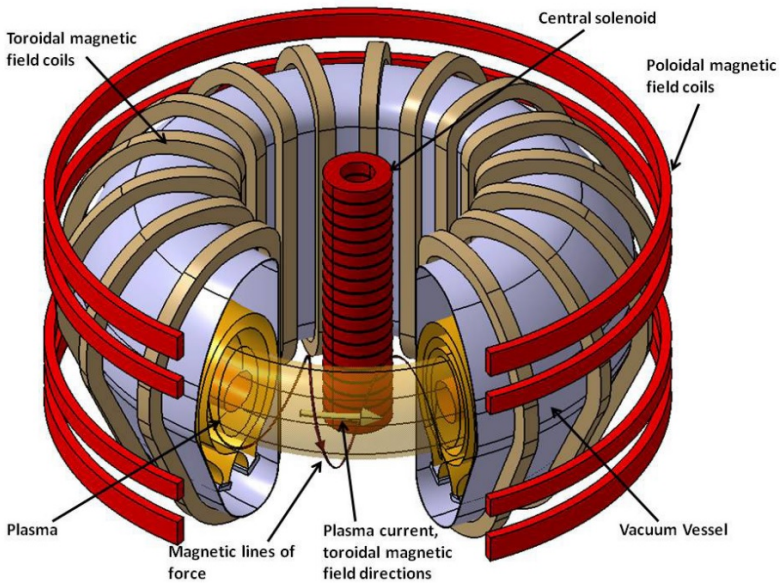

Figure 1.5: Schematic of a tokamak. Adopted from Ref.[10].

A tokamak works like a transformer, where the solenoid coils represent the primary winding while the plasma itself works as the secondary. However, inductive effects characterize plasma current as a driven-transient, while steady state discharge can be reached by driving non-inductively plasma current. The latter can be achieved by injecting high energy neutral particle beams, or using high power radiofrequency waves which resonate with natural plasma frequencies (e.g. ion cyclotron range of frequencies - ICRF, or electron cyclotron range of frequencies - ECRF, or lower hybrid range of frequencies - LHRF). These auxiliary techniques are well known and successfully used in heating the plasma to fusion relevant temperatures, but they also lead to significant degradation of the energy confinement due to turbulence and instabilities.

When dealing with MCF, the plasma pressure needs to be hindered by the magnetic force, whose strength is necessarily correlated to the intensity of the magnetic field generated inside the coils: superconducting magnets below critical temperature employed today in fusion applications can generate a magnetic field up to around 16-18 T [11]. Nevertheless, the development of high temperature superconductors promises to remarkably increase these values, leading to outstanding improvement in the MCF development [12].

To describe the efficiency of plasma heating and confinement it is common to use the β-parameter, given by the ratio of the plasma pressure to the magnetic pressure: its value is usually around few percent allowing for stability of the confined plasma. To achieve a sufficient energy confinement time, it is demonstrated that plasma major radius needs to be increased, consequently also the machine size. In fact, the construction of

bigger and bigger tokamaks is crucial to reach the condition of $Q > 1$. Moreover, a very efficient configuration when dealing with particle exhaust and energy confinement is possible through a diverted plasma cross section [13], where the magnetic field lines strike directly on a chosen target, the divertor, capable of removing helium ash and impurities. In Table 1.1, a list of main parameters (inner and outer radius, magnetic field and plasma current) of the most relevant tokamaks is reported [14].

Devisces	Location	R(m)	r(m)	B(T)	I (MA)
JT-60U	JAERI	3.4	1.1	4.2	2.5
TFTR	Princeton	2.4	0.8	5.0	2.2
JET	Abingdon	3.0	1.25	3.5	5.0
DIII-D	GA	1.67	0.67	2.1	1.6
T-10	Kurchatov	1.5	0.37	4.5	0.68
Tore Supra	Cadarache	2.37	0.8	4.5	2.0
ASDEX-U	Garching	1.65	0.5	3.9	1.4
FTU	Frascati	0.93	0.3	8.0	1.3
TEXTOR 94	Julich	1.75	0.46	2.8	0.8
TCV	Lausanne	0.88	0.24	1.4	0.17
WEST	Cadarache	2.5	0.5	3.7	1
EAST	China, Hefei	1.75	0.43	5	0.5
KSTAR	Daejeon, South Korea	1.8	0.5	3.5	2.0

Table 1.1: Abbreviations: FTU, Frascati tokamak Upgrade; GA, General Atomic Company; JAERI, Japan Atomic Energy Research Institute; JET, Joint European Toru; JT-60U, Japanese Torus 60 Upgrade; TCV, Tokamak à Configuration Variable; TEXTOR, tokamak EXperiment for Technology Oriented Research; KSTAR, Korea Superconducting Tokamak Advanced Research ; EAST, Experimental Advanced Superconducting Tokamak; TFTR, Tokamak Fusion Test Reactor

It is worth considering that tokamak technology experienced a fast and impressive growth in the past years, starting around 1960s and culminating today with the ongoing construction of the ITER project, result of the international collaboration of scientists and engineers from the European Union, China, India, Japan, the Republic of Korea, the Russian Federation and the USA. ITER's main purpose is to demonstrate technical viability of a fusion machine operating with a Q=10 and under controlled ignition, producing for the first time a sustained deuterium - tritium plasma [15]. Other technicalities and specifics of this project can be found in the available literature [16].

1.3. PFC composition and damage

Plasma-facing components (PFCs) in a fusion reactor constitute the interface between the plasma and the vessel. A PFC can be defined as an integrated material system that features a sacrificial layer exposed to plasma (tile or coating), an inner substrate which is actively cooled, and a coolant flowing liquid, see the schematic representation in Fig.1.6.

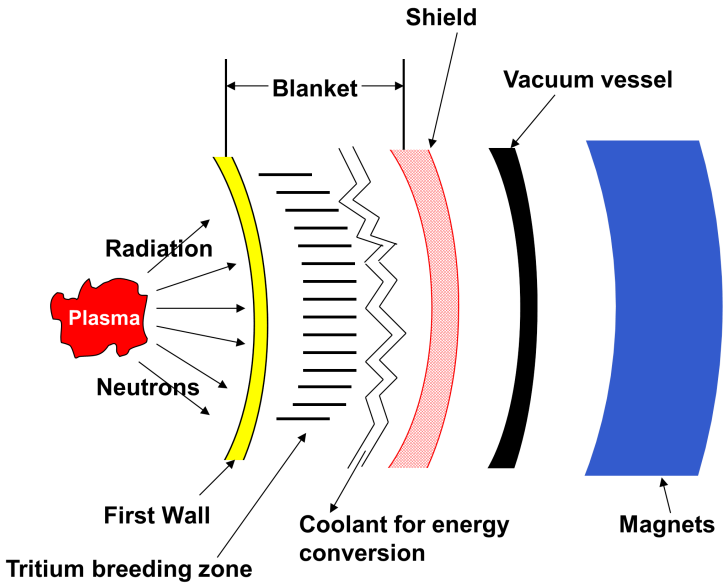

Figure 1.6: A schematic view of the arrangement of materials in a tokamak confinement wall. Adopted from Ref.[17].

At the early stage of magnetic confinement fusion experiments, glass and steel walls were utilized as the main PFCs, solutions that turned out to be inadequate and were soon replaced by carbon walls, realized with fine grain graphite or pyrolytic carbon [18]. However, graphite PFCs were deduced to be unable to guarantee safe operations and the protection of the high heat flux interfaces. More important, fuel retention is a crucial aspect to be considered when dealing with graphite PFCs [19]; short- [20] and long-term [21] tritium retention limit the lifetime of carbon components to a reduced number of possible discharges, requiring specific cleaning efforts and maintenance.

Beryllium has emerged as a suitable PFC material owing to its low atomic number, excellent thermal conductivity, oxygen gettering properties and weak reactivity with hydrogen (implying a reduced tritium inventory) [22]. On the other hand, Be is a toxic material and special costly precautions are necessary for manufacturing, installation and operation. Be is also characterized by a low melting point of $T_m = 1278°C$ [23], which implies that melt damage in the course of transient events can be an issue. Moreover, Be has a high

physical sputtering rate, while neutron-induced transmutation can lead to an increase of the tritium inventory. These drawbacks limit its applicability in tokamak first wall design for future machines, opening the way for an intense research on high-Z materials, as a possible alternative.

In particular, tungsten is nowadays considered as the most reliable material for high heat flux components [24], thanks to its resistance against erosion (low sputtering rates), its relative stability against neutron irradiation, its high melting temperature ($T_m = 3422°C$), high thermal conductivity [25] and high thermal stress resistance. On the other hand, there are disadvantages that are associated with the manufacturing below the ductile-to-brittle-transition temperature, the degradation of the mechanical properties above the relatively low recrystallization range and the risk of core contamination with W impurities given the high atomic number. Several medium sized tokamaks employ tungsten as a coating or main component for PFCs. It is worth mentioning the experience of ASDEX-Upgrade [26], where in 1995 the first W-coating was introduced, in 2007 the carbon layer was completely covered with W and in 2013 a solid W divertor was designed as well as successfully operated. The realization of the ITER project requires numerous theoretical studies and extended discharge operation with high-Z PFCs, since most likely the divertor tiles will be made of W, whereas Be will be employed for the main chamber walls.

The provision of PFCs with sufficient lifetime represents one of the major obstacles to overcome in the development of magnetic confinement fusion reactors [27, 28]. In fact, the operation of a tokamak machine implies very demanding working conditions for PFCs [29, 30]. This includes the high fluence of plasma particles (hydrogen, helium, impurities), the continuous neutron irradiation and the intense plasma heat loads (electrons and ions) during quasi-stationary normal operation. Stationary heat loads of several tens of megawatts per square meter (MW/m^2) can lead to extended recrystallization and even shallow melting in case of misalignments. Plasma particle loads can lead to excessive sputtering due to impact, embrittlement due to hydrogen retention and the formation of fuzz or bubbles due to helium implantation. Neutron-induced defects can lead to bulk embrittlement and neutron-induced transmutation can lead to a degradation of key thermophysical properties such as the thermal conductivity. Thermomechanical degradation can lead to cracking, delamination and even dust generation [31]. A summary of the wall load types relevant for burning plasmas is presented in the diagram of Fig.1.7.

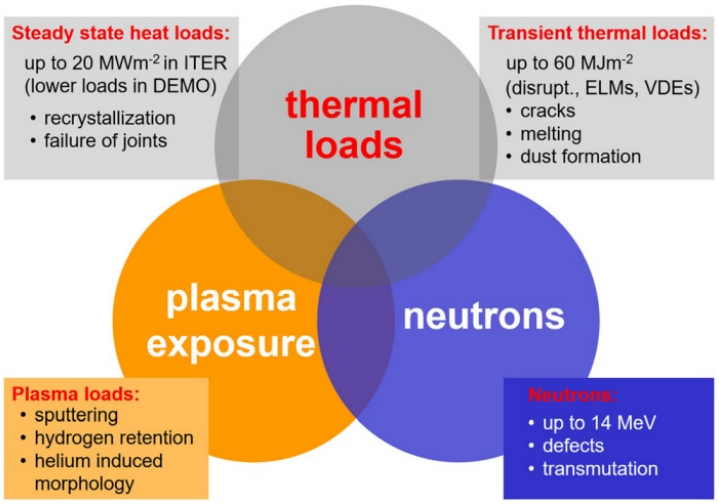

Figure 1.7: Synergistic wall loads in D-T-burning magnetic confinement experiments. Adopted from Ref.[29].

PFCs are carefully designed to withstand the aforementioned steady state conditions, allowing for a safe operation of the machine [32]. However, normal or off-normal transient events still represent a threat to their life-time expectations [27, 28]. These can be summarized as fast transient power loading due to magnetohydrodynamic instabilities such as edge-localized modes (ELMs), vertical displacement events (VDEs) or major disruptions (MDs). While the risk of PFC damage due to ELMs can be minimized through mitigation techniques [33, 34], the loss of plasma confinement caused by disruption events is a potential source of irreversible damage. Erosion, melting and explosive events characterized by permanent PFC surface topology modifications (compromising power handling in subsequent discharges) and by impurity generation and dust production (plasma contamination) are typical problems that are encountered when disruptions lead to uncontrolled energy deposition [35, 36]. In the case of ELMs, VDEs and MDs, the ions and electrons that carry the transient heat flux have thermal energies in the keV range. For such kinetic energies, depth ranges of the order of few nanometers characterize the heat deposition, which implies surface heating. Extended thin melt layers are formed, whose bulk motion is mainly dictated by volumetric Lorentz forces and whose heat transfer aspects are strongly entangled with fluid motion [37]. Though open questions remain concerning the splashing of unstable molten pools and contributions from secondary acceleration mechanisms [38, 39], it can be confidently stated that the macroscopic motion of metallic PFC melts is nowadays well understood [40]. The same cannot be stated for PFC damage induced by runaway electrons.

1.4. Runaway electrons and PFC damage

Runaway electrons (REs) are highly supra-thermal electrons that grow from a thermal energy distribution. RE generation is a basic result of the kinetic theory of plasmas. Owing to the fact that the Coulomb collision frequency decreases with the velocity, there exists a critical electric field above which the hot tail of Maxwellian electron distributions can be accelerated to relativistic energies [41]. The most crucial moments concern the plasma startup and major disruptions. The latter case is less controllable and potentially more detrimental. In the course of disruptions, after the sudden loss of plasma energy to the PFCs, there is a strong temperature drop that leads to an increase of the plasma resistivity by several orders of magnitude (thermal quench). The resulting high rate of current decay induces eddy or halo currents that flow along open field lines possibly causing strong electromagnetic loads on the PFCs, but also induces a strong electric field that can exceed the critical value for RE generation (current quench).

The growth of the RE population either occurs via diffusive leakages of electrons from the Maxwellian tail into the RE range (collective small angle scattering) [42] or via knock-on collisions that can lead to exponential growth (Maxwellian and RE large angle scattering) [43]. Combined with the high RE energy, such growth mechanisms make it possible that REs become the dominant current carrier. In fact, electric fields may convert significant fractions of the initial plasma current into runaway beams of hundreds of kiloamperes [44] and the RE density is exponentially increased by avalanche multiplications, which due to the high initial toroidal plasma current reached in ITER ($\sim$ 15 MA) could amplify the effect of runaways by a devastating factor of $\sim 10^{20}$ [45].

In the last decade, the fusion community moved from viewing REs as occasional and detrimental products of experimental campaigns to having a dedicated suite of diagnostics in nearly every relevant tokamak. Possible experimental studies are conducted in mainly two regimes: quiescent runaway electron plasmas, where the plasma density is lowered until REs begin to appear and only traces of relativistic electrons can be detected; disruptive regimes, where REs are created during disruptions and easily overtake the plasma current. Experiments have focused on RE characterization, RE avoidance and RE mitigation. Experimental evidence from the FTU tokamak [46] describe the typical spatial distribution of REs that are produced in the center of plasma and then drift toward the outer regions. In the EAST tokamak, diagnostics based on RE Bremsstrahlung emission are used to determine the average RE flux and RE energy, identified in the range of 0.2-20 MeV [47]. In particular, backward reconstruction methods based on Bremsstrahlung emission allow for the estimation of RE energy spectra, such as the one presented in Fig.1.8.

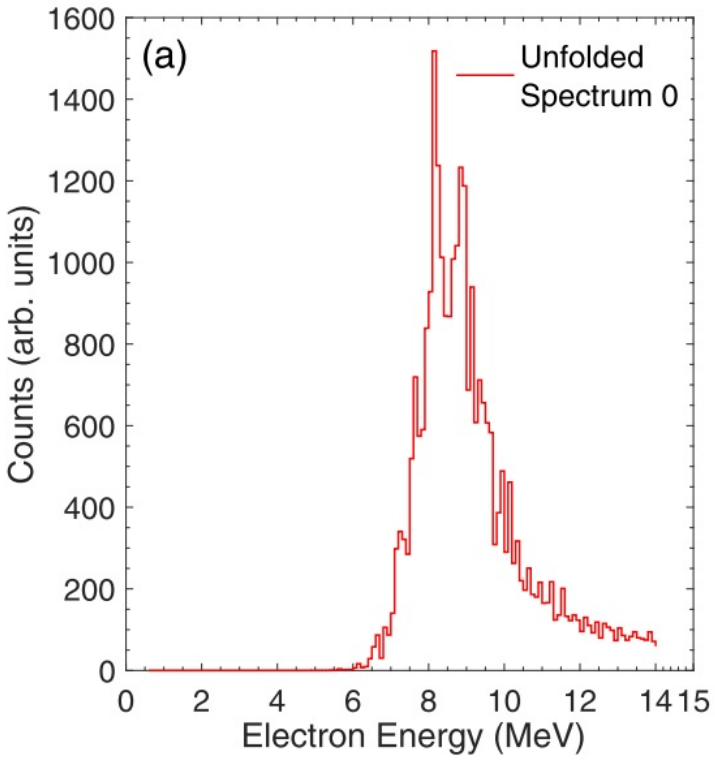

Figure 1.8: Reconstructed energy distribution of runaway electrons in the EAST tokamak. Adopted from Ref.[47].

Runaway electrons constitute the final frontier to be explored in the context of PFC damage. In contrast to other sources of PFC damage, experimental evidence are sparse and there are no dedicated modelling tools. Electrons with relativistic energies far into the MeV range have depth ranges of the order of millimetres even in high-Z metals like tungsten (W) [48]. Thus, RE heat deposition is not only localized but also volumetric in nature. Deep RE-induced melting should severely affect PFC lifetime, whereas RE penetration down to the coolant channels could lead to pipe over-pressurization and ultimately to loss-of-coolant accidents with disastrous consequences [49].

Naturally, RE-induced PFC damage strongly depends on the PFC composition and the RE impact characteristics. In the JET Be first wall, RE termination led to localized melt damage surrounded by radially distributed splash traces [50]. The splashes are observed below an upper dump plate [51] and with a size before impact estimated to be several μm. In particular, between 2011 and 2016 three experimental campaigns were carried out with the ITER-Like Wall (JET-ILW), each of them followed by a shut down allowing for in-vessel inspections [52]. During ILW-3, as illustrated in Fig.1.9, much more melting was detected on the Be dump plate DP-4 (i.e. upper limiter tile), mainly attributed to experiments dedicated to RE generation and mitigation [53].

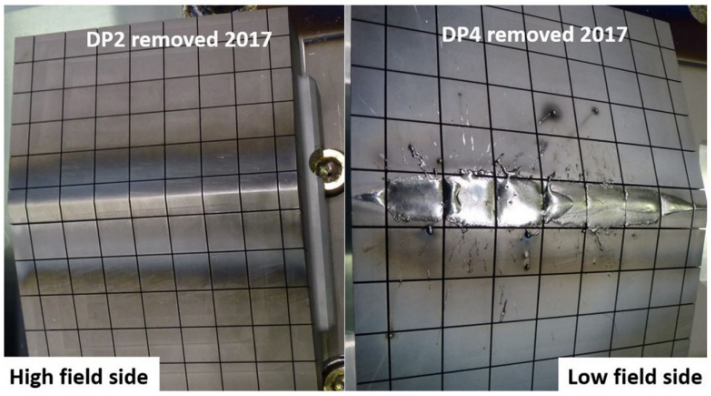

Figure 1.9: In vessel images documenting the melting of Be JET tiles that were removed for post-mortem analysis after ILW-3. Adopted from Ref.[52].

An important example concerns the FTU tokamak, a machine that features a stainless steel wall and molybdenum limiters. Post-mortem investigations revealed extensive melt damage on specific tiles of the poloidal limiter and multiple shallow craters on the line-of-sight tiles of the toroidal limiter [54]. In situ camera observations, modelling with the MIGRAINe dust dynamics code [55] and crater replication with the aid of a two-stage light gas gun [56] led to the interpretation that both the primary (poloidal tiles) and secondary (toroidal tiles) damage was caused by REs [54]. In particular, the REs drift towards the outer regions and terminate on the protruding poloidal limiter. Volumetric energy deposition has a non-monotonic energy profile which leads to a maximum temperature beneath the PFC surface. Internal stress build up, due to the uneven thermal expansion and internal boiling, leads to an explosive thermal shock event that is characterized by the expulsion of fast debris. Such fast solid particles follow straight line trajectories until they impact on the neighbouring tiles leading to excessive cratering due to their large kinetic energy. A careful examination of the evidence led to the conclusion that the fast Mo dust particles had a diameter of $\sim 50\,\mu$m and a speed of around 1 kms^{-1} [54]. The primary PFC damage is depicted in Fig.1.10, the ejected dust particles in Fig.1.11a and the secondary PFC damage in Fig.1.11b. Less conclusive evidence of explosive material detachment have been obtained in the COMPASS [57], T-10 [58] and WEST tokamaks. As we shall discuss in the final chapter, explosive material detachment is also realized in DIII-D.

Figure 1.10: Primary damage: RE-induced explosion of the Mo poloidal limiter in FTU. Adopted from Ref.[54].

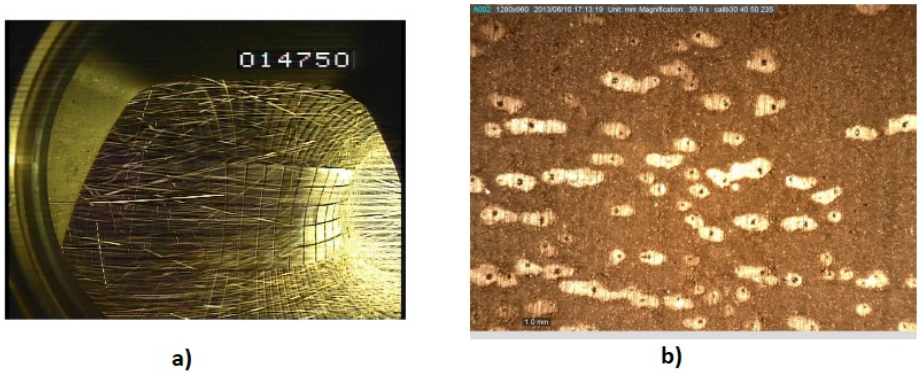

Figure 1.11: Secondary damage: craters from high velocity solid Mo dust impacts on the line-of-sight Mo toroidal limiter in FTU. Adopted from Ref.[54].

Finally, let us discuss the WEST tokamak, for an example with RE-induced damage on W PFCs. In 2016, a W-coated set of PFCs was developed and installed in the WEST machine [59]. Four experimental campaigns were conducted (C1-C4), to primarily investigate damage caused by excessive heat loads. A large fraction of performed discharges included the presence of off normal scenarios, such as REs and disruptions [60]. From post-operation inspections, it turned out that the outer limiter was the most damaged coated PFC: coating delamination and tungsten melting are visible in Fig.1.12. The damage is caused by RE beams whose impact location is concentrated for more than 50% in the mid-plane. To better cope with REs and prepare for longer pulse operations, the W-coated panels were replaced by bulk W tiles in the C4 campaign. The following *in situ* inspections confirmed the reduced PFC damage and surface modification, but still revealed material erosion and plasma footprints.

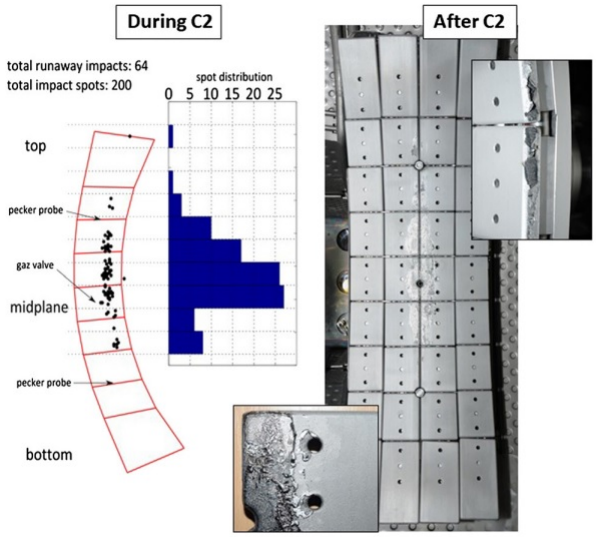

Figure 1.12: In situ images of the outer limiter in WEST. After the C2 campaign damage was mainly observed on the tiles located in the mid-plane which is highly correlated with the predicted RE impact location. Adopted from Ref.[61].

Overall, RE-induced PFC damage might be tolerable in contemporary fusion devices, but the same cannot be said for future fusion reactors, where more stored magnetic energy will be available for conversion to RE energy [62], better confinement will allow more RE energy gain prior to PFC incidence [63] and larger plasma currents will enable much more efficient multiplication. The first line of defense against major disruptions and accompanying RE events concerns the development of effective mitigation and suppression techniques. This task is threefold [64]: (1) to spatially distribute heat loads, thus preventing melting of PFCs; (2) to limit the effects of induced eddy and halo currents in vessel materials; (3) to suppress or mitigate the intensity of RE beams. Material injection in the form of shattered deuterium pellets with neon and argon [65] is a candidate for the first two goals. Moreover, it is known that the critical electric field is proportional to the electron density [66] . Hence, raising the electron density at sufficient high level through injected material constitutes a chance to achieve RE mitigation. However, it remains uncertain whether all these impurities can be assimilated into an operating machine like ITER. Other alternative mitigation techniques have additionally been proposed: resonant magnetic perturbations (RMPs) for which specific active coils are needed [67] or active control of the current in the central solenoid to dissipate the RE beam energy [68]. Still, there remains a lack of evidence on the efficiency of these methods in ITER-like scenarios [69] and none of the proposed solutions is powerful enough to achieve RE prevention. It naturally follows that predictive modelling of RE-induced PFC damage is crucial for the success of future tokamak reactors and their high performance operation.

1.5. Status of RE-induced PFC damage modelling

The primary PFC damage, realized at the RE impact location, extends deep within the material not only compromising its power handling capabilities but also posing a risk to cooling pipes. The secondary PFC damage, spread around the vessel within the line-of-sight of the RE impact location, is non-localized and might threaten the integrity of more sensitive areas of the wall that are not designed to withstand any damage. To develop reliable cost-effective predictive modeling for the complex process of RE-PFC interaction, different tools are necessary. The simplest realistic workflow includes the thermal response of the PFC, but neglects the combined thermomechanical aspects of the PFC response that lead to explosive material detachment. First, RE heat deposition into matter has to be modeled through a Monte Carlo (MC) particle transport code. Second, the extracted volumetric heat source has to be incorporated into a heat transfer code to simulate the thermal response including phase change.

One of the first attempts to understand RE energy deposition was due to Kunugi and coworkers who employed the EGS4 code to simulate RE-induced electromagnetic showers and to obtain the energy deposition profiles [70]. Several materials and RE parameters were probed. Inconsistencies between the EGS4 and GEANT3 results were observed, but the source of the discrepancy was not understood. In a similar fashion, Bartels employed the GEANT3 code to simulate RE energy deposition in different scenarios [71]. The effect of the magnetic field was also included. Rough estimates of melting were also reported for various divertor designs.

To our knowledge, the first combined MC - heating investigation was reported by Maddaluno and collaborators who combined the FLUKA MC code with the ANSYS finite element heat conduction code [72]. Different PFC configurations and RE impact parameters were considered. Unfortunately, a multiple scattering implementation was employed that is not appropriate for some of the studied scenarios. A similar investigation was carried out by Sizyuk and Hassanein, who added an MC transport model in the HEIGHTS computer package and combined with the existing HEIGHTS heat conduction module [73]. The effect of the magnetic field was included and a mixed scattering scheme was correctly introduced. Unfortunately, the adopted differential scattering cross-sections ranged from overly simplistic (Bethe-Heitler description of Bremsstrahlung and Klein-Nishina description of Compton scattering) to completely inaccurate (Rutherford description of electron-nucleus scattering), while positron generation and transport were not included. Finally, a combined MC - heating investigation was carried out also by Bazylev and coworkers, who combined the ENDEP MC code with the MEMOS melt mo-

tion code [74, 75]. Unfortunately, a concrete description of the adopted scattering models is not available.

To sum up, even as far as the simplest workflow is concerned, the several modelling attempts reported in the literature are characterized by oversimplifying assumptions and are lacking rigor. Nevertheless, the respective modelling results, though only qualitative in nature, still serve as a warning for the possible consequences of unmitigated or partially suppressed REs impacting on PFCs. The goal of this thesis is to improve the limited understanding of RE-induced damage on PFCs by providing a rigorous and reliable workflow for such predictive modelling.

The thesis starts with the standardization & validation of Monte Carlo simulations of volumetric energy deposition by relativistic REs into the PFC materials of interest. This includes all the facets of electron passage into matter including photon generation and their transport, delta electron generation and their transport, positron generation and their transport as well as atomic relaxation. For this purpose, the GEANT4 MC-code is chosen. Benchmarking activities are carried out to test the accuracy of simulated physics processes among the variety offered by GEANT4. Next, the 3D heat map outcome of MC runs is incorporated into the MEMENTO melt dynamics code (the latest numerical implementation of the MEMOS-U physics model) to provide information on the three-dimensional temperature field and the maximum temperature values reached upon RE loading.

A fundamental aspect of this thesis concerns the comparison of the entire workflow with a real case scenario coming from a controlled dedicated experiment. In particular, the modelling predictions have been correlated to the post-mortem analysis of RE-induced damage on graphite PFCs exposed to the DIII-D plasma. Results concerning temperature distributions and estimated vapor losses are in agreement with empirical observations on the exposed sample. However, the modelling of RE-induced PFC damage is still at its infancy since more elaborate physics-rich models are required to deal with compressive flows, thermoplastic stresses, shockwave propagation and solid fragmentation; elements which are necessary to achieve a complete understanding of RE-PFC interactions.

2 | Physical processes of relevance for RE passage into matter

As aforementioned, the typical energy range of REs is of the order of MeV. In ITER, RE beam energies are expected to lie between 1 and 50 MeV [76]. At this point, it is instructive to introduce the concept of the electronic depth range, i.e., the average path length traversed by an electron within a medium as it slows down from an initial energy up to an energy of the order of the lowest atomic ionization energy of the medium. The corresponding depth ranges are 0.3-9.3 cm for Be and 0.04-0.62 cm for W. These values imply deep penetration inside plasma facing components and thus the necessity to include a volumetric energy deposition.

When electrons penetrate into condensed matter, different types of interactions take place which lead to energy loss, scattering, excitation of bound electrons and generation of new particles. More specifically, electrons undergo

- inelastic collisions with bound electrons leading to the so-called ionization-excitation losses and the generation of often fast secondary electrons (delta rays);
- strong deflections in the nuclear/electronic microfields leading to the radiative losses and the generation of Bremsstrahlung photons;
- elastic scattering in collisions with nuclei.

In addition, in order to accurately describe the energy deposition process, it is important to follow the transport of all secondary particles that are created by RE matter interaction. This concerns first generation particles (delta rays, Bremsstrahlung photons), second generation particles (Auger electrons, fluorescence photons) and third generation particles (positrons). In fact, in the MeV range, primary electrons tend to move along their straight line trajectory, while secondaries at lower energies are more collisional, depositing energy more efficiently. This chapter focuses on the most relevant electromagnetic phenomena; their physics background, their state-of-the-art description and associated limitations as well as their implementation in commercial MC codes.

2.1. Electromagnetic physics processes

The construction of a rigorous and coherent list of physical processes, relevant for RE passage into matter has been given high priority. In spite of the use of a commercial MC software, the goal is to have complete control of the physics models as well as to be aware of their accuracy, their underlying approximations, their limitations and their importance depending on the material and exact RE energy. The focus lies on electromagnetic processes, nuclear processes due to the generation of neutrons via photoneutron or electro-neutron paths are beyond the scope of the present thesis. In any case, nuclear processes are not expected to affect volumetric heat deposition. A summary of the electromagnetic processes of interest is provided in Table 2.1:

INVOLVED EM PROCESSES

Particle	**Process**	**Specifics**
Electrons e-	Ionisation	δ-ray production & excited atoms
	Scattering	single / mixed / multiple scattering models
	Bremsstrahlung	photon production
Positrons $e+$	Ionisation	δ-ray production & excited atoms
	Scattering	single / mixed / multiple scattering models
	Bremsstrahlung	photon production
	Annihilation	photon production
Photons γ	Compton scattering	inelastic & excited atoms
	Rayleigh scattering	elastic
	Photo-electric effect	δ-ray production & excited atoms
	Gamma conversion	electron-positron production
Excited atoms A^*	Auger transition	δ-ray production
	Radiative transition	photon production

Table 2.1: Physics processes in the course of RE-induced electromagnetic showers.

2.1.1. Electron ionization/excitation losses

The stopping power is the average rate at which charged particles lose energy along their trajectories. Let us begin the discussion with the electronic stopping power of a singly charged ion passing through matter, whose most elementary description is given by the Bethe expression, reported in 2.1.

$$\frac{dE}{dx} = -2\pi e^4 \left(\frac{ZN_a\rho}{A}\right)\frac{1}{E}\ln\left(\frac{4m_eE}{MI}\right) \tag{2.1}$$

where Z, ρ, A denote the target atomic number, mass density and atomic weight, M the projectile mass, E the projectile kinetic energy, x the projectile path, I the so-called mean ionization and excitation energy that is characteristic of the target. The above is a non-relativistic result that is based on first-order perturbation theory and neglects the polarization of the medium and the motion of the orbital electrons. More accurate expressions are derived in Ref.[77]. The main differences between the electronic stopping power of ions and the electronic stopping power of electrons stem from exchange effects and the equal masses of the collision partners.

The Bethe stopping power for electrons reads as

$$\frac{dE}{dx} = -2\pi e^4 \left(\frac{ZN_a\rho}{A}\right)\frac{1}{E}\ln\left(\sqrt{\frac{e}{2}}\frac{E}{I}\right) \tag{2.2}$$

where the e within the logarithm is the natural base and not the electron charge. Naturally, at very high electron energies, both relativistic and spin effects need to be included. The relativistic Bethe stopping power for electrons is formally obtained by integrating the full QED electron-electron scattering cross section (known as the Møller cross-section [78]) that automatically includes relativistic, spin and exchange effects. Shell corrections (projectile velocity is not necessarily much larger than the orbital electron velocity) and density-effect corrections (target polarization) need to be included. It is pointed out that the evaluation of the electronic stopping power via the full Bethe formula requires input for two target dependent properties: the mean excitation energy I and the density effect correction $\delta(E)$. Such input (of varying levels of complexity and accuracy) is readily available for all elementary targets and many compounds.

There are two drawbacks associated with the use of variants of the Bethe expression. (1) The stopping power is the average rate at which the electrons lose energy along their trajectories. In the *continuous-slowing down approximation* (CSDA), where fluctuations in the energy loss due to discrete events are neglected, the electrons lose energy continu-

ously along their track with a mean energy loss per unit path-length given by the stopping power. The CSDA loses its usefulness when the average fractional energy loss in a single collision exceeds few percent and completely breaks down for electron energies below few keV when straggling becomes dominant. (2) Originating from scattering cross-section integration, the Bethe formula does not retain any information for the excited atomic electrons. Thus, all the energy loss has to be implicitly assumed to be deposited locally; a gross oversimplification given the known importance of energetic secondary electrons (delta rays).

Concerning commercial MC codes, it is worth singling out the semi-empirical treatment of the PENELOPE code [79]. PENELOPE employs differential scattering cross-sections from a generalized oscillator model whose parameters are optimized so that the high energy Bethe formula and tabulated mean excitation energies I are reproduced. This ensures that both shell and density effect corrections are roughly included, now at the differential cross-section level. It is noted that the model features a decomposition to distant collisions (semiclassical picture, resonant character) and to close collisions (binary collisions with free electrons at rest, full QED Møller differential cross-section). Apart from the PENELOPE model, GEANT4 also features the Livermore and MicroElec models.

2.1.2. Electron Bremsstrahlung losses

The nuclear stopping power refers to the average rate at which charged particles lose energy due to Bremsstrahlung (braking radiation), i.e. the radiation emitted by the charged particles due to their deflection in the field of another charged particle. There are two contributions: electron-nucleus Bremsstrahlung (dominant) and electron-electron Bremsstrahlung (small correction except for very high energies and very low atomic numbers Z). Very roughly, in the relativistic regime, it can be shown that the electronic stopping power scales as $Z\ln(E)$ and that the nuclear stopping power scales as Z^2E. Thus, for any material there exists a critical electron energy above which radiative losses dominate. A simple empirical formula reads as $T_c = 600/Z$ in MeV. Thus, we have $T_c = 100$ MeV (graphite, more exact calculation yields 95.4 MeV) and $T_c = 8$ MeV (tungsten, more exact calculation yields 10.7 MeV). In addition, a threshold energy can also be defined below which radiative losses can be deemed negligible. We have $T_h = 6.44$ MeV (graphite) & $T_h = 350$ keV (tungsten).

Electron-nucleus Bremsstrahlung refers to Bremsstrahlung in the field of the atomic nucleus. The respective cross-section is roughly proportional to Z^2. One of the most relevant analytical results is the Bethe-Heitler expression [80] that is valid for bare Coulomb interaction and within the Born approximation [81]. Charge screening and additional terms of the Born series are important at mildly relativistic and extreme relativistic electron energies. A numerical full QED treatment is available by Tseng and Pratt [82] with near exact results obtained for certain atomic numbers, electron energies and photon energies. In the famous Seltzer and Berger tabulations [83, 84] (employed in most commercial MC tools), these quasi-exact results are numerically interpolated and extrapolated with the aid of limiting analytical formulas and experimental results.

Electron-electron Bremsstrahlung refers to Bremsstrahlung in the field of the bound atomic electrons. The respective cross-section is roughly proportional to Z. There are two main physical differences between e-e and e-n Bremsstrahlung that concern target electron re-coil and electron exchange effects. An important analytical result is the so-called Haug expression [85] that is exact for free electrons within low-order perturbation theory. Recoil and exchange effects are treated exactly, but screening and atomic binding effects are not considered. Another important analytical result is the Wheeler and Lamb cross-section [86] that considers screening and atomic binding effects within the Born approximation and an additional high-energy, static-atom approximation. The ubiquitous Seltzer and Berger tabulations utilize the Haug expression together with an additive correction that stems from the Wheeler and Lamb cross-section.

2.1.3. Electron elastic scattering

It is instructive to first discuss *electron-proton scattering*. Different regimes can be distinguished by comparing the relativistic de Broglie wavelength λ_e of the electron with the radius of the proton r_p. In particular,

- if $\lambda_e > r_p$, the electron is elastically scattered by a point-like charge;
- if $\lambda_e \sim r_p$, the electron is elastically scattered by a charge distribution;
- if $\lambda_e < r_p$, the regime of deep inelastic scattering is reached with the possibility of shattering and hadronization.

Electron-proton elastic scattering is described with the aid of established differential scattering cross-sections.

- The Rutherford cross-section in the case of non-relativistic classical electrons scattered by a point-like proton [87].
- The Mott scattering cross-section in the case of relativistic spin 1/2 electrons scattered by a spin-less point-like proton (Dirac equation based) [88].
- The Rosenbluth scattering cross-section in the case of relativistic spin 1/2 electrons scattered by a spin 1/2 point-like proton (includes the magnetic moment interaction) [89].
- The full Rosenbluth scattering cross-section in the case of relativistic spin 1/2 electrons scattered by a spin 1/2 finite size proton. The finite size effects are included via the electric and magnetic form factors which are the spatial Fourier transforms of the proton charge distribution and the proton magnetic moment distribution.

In the RE energy range, proton recoil is negligible and scattering is indeed elastic, while the Mott scattering cross-sections are relevant.

We are now in the position to discuss *electron-nucleus scattering*. The Mott scattering cross-section is formally derived by solving the Dirac equation in a bare Coulomb field. This neglects screening by the surrounding atomic electrons. The simplest approximations to include screening consider a Yukawa-type screened Coulomb potential with a shielding length comparable to the atomic radius. The whole problem of calculating the elastic scattering cross-sections comprises defining an energy dependent spherically symmetric interaction potential between the incident electron & the atom (core electrons plus nucleus) and numerically solving the Dirac equation for it. State-of-the-art differential scattering cross-sections are those computed by the ELSEPA code [90], which are

generally valid for energies from a few tens of eV up to about 1 GeV. The ELSEPA interaction potential includes four components: an electrostatic interaction term with contributions from the nucleus and the surrounding electrons, an exchange interaction term, a correlation-polarization interaction term and an imaginary absorption interaction term. Most commercial MC codes are based on ELSEPA differential cross-sections.

2.1.4. Photons

In RE-induced electromagnetic showers, photons are secondary particles that can be generated from Bremsstrahlung emission (first generation), atomic de-excitation processes (second generation) and electron-positron annihilation (third generation). Photons in the eV-GeV range have various modes of interaction with ordinary matter with corresponding cross-sections that depend on their energy and the target material. Fig.2.1 illustrates the photon cross-sections as a function of the photon energy for lead (Pb, Z=82) and carbon (C, Z=6).

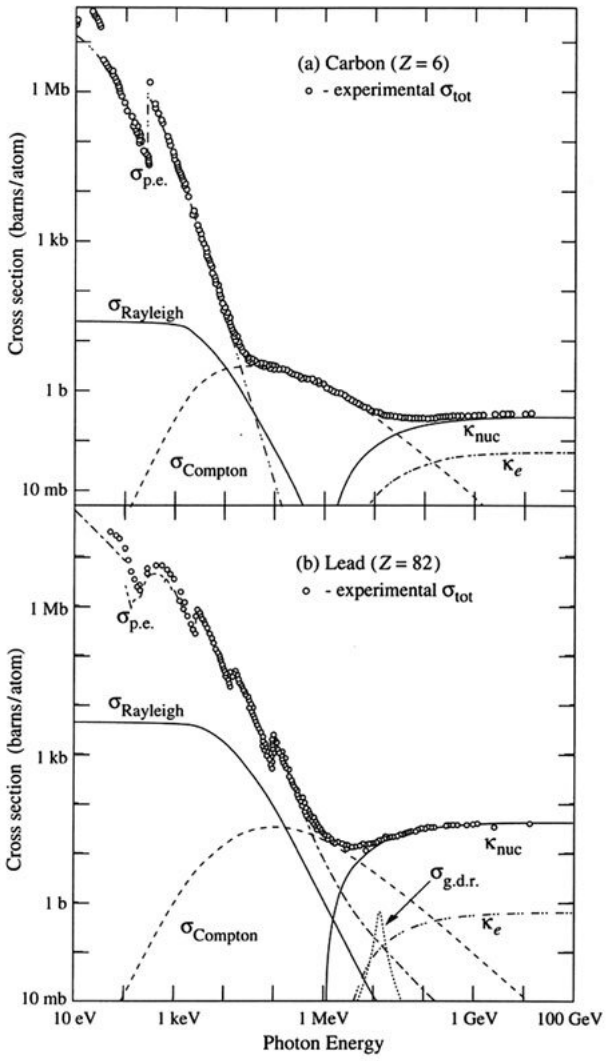

Figure 2.1: Photon total cross section as a function of the photon's energy in carbon and lead, with the contributions of different processes. Note that $\sigma_{p.e.}$ stands for photoelectric effect, $\sigma_{g.d.r}$ for giant dipole resonance effect, while κ_{nuc} and κ_e correspond to pair production in the nuclear or electron field. From [91].

Photo-absorption constitutes the dominant process at low energy (10 eV to hundreds of keV), i.e. for photon energies that are comparable to the subshell ionization energies. Rayleigh scattering is also important for photon transport in the sub-MeV range. Compton scattering becomes dominant at energies above a few hundred keV with cross sections that are connected to the electron density of the target and that increase near-linearly with the atomic number (thus more relevant in Pb than C). Pair production (mainly in the vicinity of nuclei and not electrons) comes into play above the threshold of 1.022 MeV and dominates deep in the MeV range. Finally, nuclear resonance scattering (see the giant dipole resonance - GDR [92, 93]) that is accompanied by nuclear excitation can be an important inelastic contribution around 10 MeV. With the exception of the latter process, all aforementioned processes are further analyzed in what follows.

Compton scattering (inelastic)

Compton scattering is the inelastic scattering of medium-high energy photons off electrons: the electron absorbs a photon, re-emits a secondary lower energy photon and then recoils. For a free electron at rest, the differential scattering cross-section is given by the well-known Klein-Nishina formula [94]. For atomic electrons in condensed matter, binding effects and Doppler broadening should be included.

The Waller-Hartree [95] theory for binding effects leads to a multiplicative correction factor to the Klein-Nishina expression. The relativistic impulse approximation of Ribberfors [96] can treat both binding and Doppler effects under certain assumptions. PENELOPE follows the Ribberfors theory, while GEANT4 offers several models (some of which consider both corrections).

Rayleigh scattering (elastic)

Four processes are relevant for the elastic interaction of photons with atoms: Rayleigh scattering [97] (interaction with atomic electrons), nuclear Thomson scattering [98] (interaction with a point charge nucleus at rest), Delbrück scattering [99] (non-linear interaction with the field of the nucleus), nuclear resonance scattering [100] (interaction with the internal structure of the nucleus which involves the GDR). Commercial MC tools only consider Rayleigh scattering, an approximation that is mostly accurate for photon energies below 1 MeV.

Rayleigh scattering concerns the elastic scattering of photons by bound target electrons. It is not accompanied by atomic excitation and thus there is no energy loss for the photon. The high frequency limit of Rayleigh scattering corresponds to photon energies much

higher than the K-shell ionization energy. It is described by the Thomson differential scattering cross-section (free electron at rest) multiplied by an atomic form factor [101] (connected to the atomic electron density). At low frequencies and near absorption edges, anomalous form factors need to be applied. Form factors are available for all elements in the LLNL Evaluated Photon Data Library (EPDL97). PENELOPE follows the standard treatment including anomalous form factors, while GEANT4 features many Rayleigh models, some of which are overly simplistic.

Electron-positron production

Electron-positron production is the only type of photon conversion into matter-antimatter pairs that is relevant in the MeV energy range. Simultaneous energy and momentum conservation requires the presence of another particle in the photon vicinity. If it is a nucleus, one has pair production. If it is an atomic electron, one has triplet production. The photon energy threshold for pair production is two times the electron rest energy, $2m_ec^2 = 1.022$ MeV, provided that the generated positron and electron are free (with binding effects lowering this threshold). On the other hand, the photon energy threshold for triplet production is four times the electron rest energy, $4m_ec^2 = 2.044$ MeV. The pair production cross section roughly scales as Z^2, while the triplet production cross section is roughly proportional to Z. Pair production is the dominant photon interaction for low-Z elements at photon energies above 100 MeV, and for high-Z elements at energies above a few MeV.

Since pair production can be deemed as the converse process of Bremsstrahlung , the starting point is a Bethe-Heitler expression (unscreened limit, Born approximation). The Bethe-Heitler expression [102] needs to be improved with the addition of Coulomb corrections [103] (complicated), screening corrections [104] (straightforward to introduce) and radiative corrections [105] (generally negligible). The general MC strategy is to employ a Bethe-Heitler expression with screening corrections and then to add an approximate Coulomb correction factor. The PENELOPE treatment is based on a Yukawa screening potential of optimized shielding length and a Coulomb correction valid for high energies. The GEANT4 code features different models, but none treats both screening and Coulomb corrections.

Photo-absorption

In the textbook version of the photoelectric effect, a valence surface electron absorbs a photon with energy larger than the material work function and is then emitted to

the ambient. In RE-induced electromagnetic showers, a core electron absorbs a photon with energy larger than the respective subshell ionization energy (see the characteristic sawtooth absorption edges in the cross section) and is then emitted inside the metal.

For the purposes of modelling, four ingredients should be available: atomic subshell ionization cross-sections, total photoelectric cross-sections, atomic binding energies, information on the photoelectron direction. Massive tabulations are available in the literature that are implemented in a similar manner in commercial MC codes, such as Scofield's extended cross-section tabulations [106] from 1 keV up to 1 MeV, Hubbell's extended cross-section tabulations from 1 MeV up to 100 GeV [107] and the EPDL97 library of LLNL [108]. The direction of emission of the photoelectron is typically sampled using the Sauter differential cross section [109].

2.1.5. Positrons

Positrons are high-order generation particles in RE-induced electromagnetic showers; Bremsstrahlung leading to high energy photons and photon conversion producing positrons. Above the kinematic threshold, the cross-section for electron-positron pair production increases with the photon energy up to a plateau deep in the MeV range and roughly scales with the square of the atomic number [110]. As a consequence, electron energy deposition does not depend on positron transport for low-Z materials and energies up to around 100 MeV, but positron contributions are relevant for high-Z materials and RE energies in the 10 MeV range.

Similar to electrons, positrons scatter elastically off nuclei, suffer nuclear stopping due to Bremsstrahlung and undergo electronic stopping due to ionization-excitation losses. In addition, positrons can annihilate with bound electrons. A brief summary of the relevant processes is provided below:

- **Nuclear stopping**. Electron-nucleus and positron-nucleus Bremsstrahlung are treated in an identical fashion within the Born approximation and without screening corrections. Full QED treatments constitute the basis for the parameterization of the ratio between positron and electron nuclear stopping powers as function of the atomic number and incident energy.

- **Electronic stopping**. The general treatment is the same for electrons and positrons. Due to the absence of exchange effects and attraction in lieu of repulsion, the Møller cross-section needs to be substituted with the Bhabha cross-section and the electronic Bethe formula with the positronic Bethe formula.

- **Elastic scattering**. The methodology for the numerical solution of the Dirac equation in a spherical symmetric potential is the same, but the functional form of the interaction potential differs. The differences concern all four components: electrostatic, exchange, correlation-polarization and absorption.

- **Electron-positron annihilation**. The adopted description in commercial MC codes is elementary, because positrons typically lose most of their energy prior to their annihilation. The energy equipartition between the two generated photons is determined by the Heitler differential cross-section [111], while the photon angular distributions are determined by the conservation laws.

2.1.6. Atomic relaxation

Among the processes discussed so far, three lead to atomic ionization and leave the atom in an excited state: electron/positron ionization-excitation losses, Compton scattering of photons and the photo-electric effect. The presence of a vacancy in the shell structure implies an amount of stored energy that needs to be followed for the computation of volumetric energy deposition. Such a vacancy is filled in two possible ways:

1. **radiative transitions:** where an electron drops down from an outer to an inner subshell emitting a photon whose energy corresponds to the subshell energy difference. In this manner, the single vacancy propagates upwards in the energy diagram;
2. **Auger transitions:** where an electron again drops down from an outer to an inner subshell emitting a second electron whose energy corresponds to the subshell energy difference. In this manner, the single vacancy leads to two vacancies propagating upwards in the energy diagram.

As illustrated in Fig.2.2, radiative transitions are more probable for inner shell vacancies of high-Z elements, while Auger transitions are more probable for outer shell vacancies of low-Z elements.

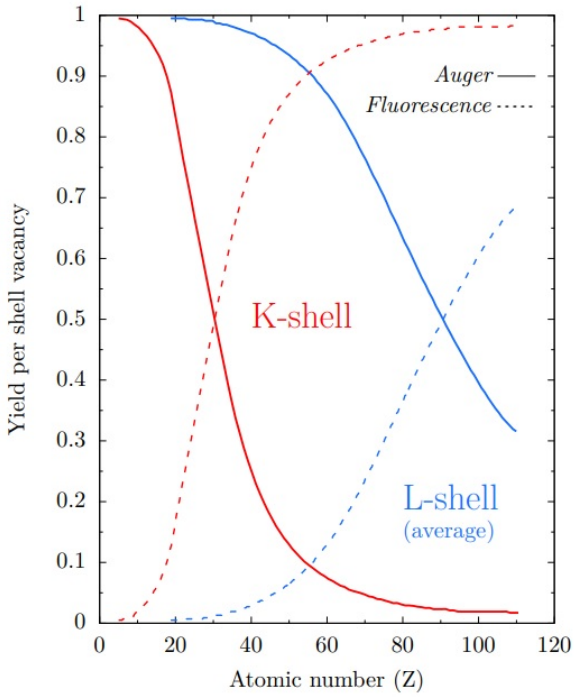

Figure 2.2: Fluorescence and Auger yield for atoms with $Z < 120$, from [112]

At what follows, we shall discuss whether it is necessary to follow the Auger electrons

and fluorescence photons produced and which cut-off should be introduced. *In case of ionization-excitation losses*, a single electron/positron can ionize many atoms with the ionization preferentially in the outer sub-shells, which implies a weakly excited nucleus. *In case of Compton scattering*, a single photon will most probably ionize an encountered atom; the probability that an inner subshell is ionized is roughly proportional to the number of electrons in the subshell, which implies a moderately excited nucleus. *In case of photo-absorption*, a single photon necessarily ionizes a single atom with the probability of absorption in the K-shell being 80% for photon energies above the K-edge, which implies a highly excited nucleus.

Given the above analysis, the stored energy can be assumed to be dissipated locally for ionization-excitation losses and Compton scattering and the generated electrons/photons from photo-absorption can be monitored up to an energy threshold. The majority of commercial MC tools offer such a possibility, including GEANT4.

2.2. Implementation of scattering events

There are three different methodologies for the numerical implementation of scattering events that are characteristic of the trade-off between accuracy and computational cost.

- **Detailed MC simulations** where all scattering events (elastic and inelastic) experienced by an electron are described in chronological succession. Within the statistical MC errors, detailed simulations are "exact", in the sense that they give the same results as the formal solution of the transport equation, and are only limited by the accuracy of the elastic and inelastic differential cross-sections followed. For very high incident energies, the average number of scattering events per trajectory drastically increases and the detailed simulations become computationally costly and ultimately unfeasible.
- **Condensed MC simulations** where approximate multiple scattering theories are introduced. These lead to systematic errors because there is no real knowledge of the spatial particle distribution after travelling a given path length. The simulation results then depend on the adopted step length. The most standard multiple scattering theories are due to Goudsmit & Saunderson [113], Moliere [114] and Lewis [115].
- **Mixed MC simulations** where the above schemes are appropriately combined. Hard events, i.e. elastic scattering at angles larger than a cutoff and inelastic energy losses larger than another cutoff, are simulated in a detailed manner, since they cause large deflections and energy losses that can only be properly reproduced with a detailed simulation. Soft events, i.e. elastic scattering at angles smaller than a cutoff and inelastic energy losses smaller than another cutoff, are simulated in a condensed manner, since they have a mild smoothed-out effect on the trajectory evolution that can be captured by multiple scattering theories.

PENELOPE features a mixed MC scheme that concerns both elastic and inelastic scattering [116]. GEANT4 features all possible schemes including all aforementioned multiple scattering models as well as mixed MC schemes.

3 | GEANT4 code

The Monte Carlo (MC) method is a numerical solution to a problem that is based on random statistical trials. Monte Carlo methods accurately model the physical interactions that take place in the course of particle transport, thus, they have a long history of application to problems relevant to particle passage through matter. Nowadays, numerous general purpose MC particle transport codes are available such as GEANT4 (particle transport) [117], FLUKA (particle transport) [118], EGSnrc (electron, positron and photon transport) [119], PENELOPE (electron, positron and photon transport) [120], MCNP (neutron, electron, positron and photon transport) [121], TRIPOLI-4 (neutron, electron, positron and photon transport) [122], Serpent (neutron and photon transport) [123], CASINO (electron transport) [124], SRIM (ion transport) [125], etc.

This chapter offers an overview of the chosen commercial MC code for the runaway electron transport simulation inside condensed matter, GEANT4, including basic technical and structural details as well as a description of the procedure followed in the simulation of particle-matter interactions. Finally, some statistical considerations are reported that reflect the trade-off between accuracy and computational cost.

3.1. GEANT4

GEANT4 (GEometry ANd Tracking) is a toolkit for the simulation of the passage of particles through matter which is based on Monte Carlo methods. It is the latest installment of the GEANT series of software tools developed by the Geant4 Collaboration at CERN, starting in December 1994 in Geneva, and the first to be based on object oriented programming (in C++). Its fields of application include high energy, nuclear and accelerator physics, as well as medical and space science. Various experiments in the high energy physics field were designed on the basis of GEANT4 contributions such as ATLAS, COMPASS, LHCb and LHC inside the CERN research center [126]. The code allows to closely mimic an experimental set up by reconstructing the geometry, specifying the material composition, as well as including detectors and eventual absorbers. Faithful reproduction of the experimental layout is important as such details affect the particle paths and thus the final quantities of interest. In addition, GEANT4 offers a series of possible visualization options such as OpenGL, Open Inventor, VRML or VTK.

One of the key aspects of the code is the possibility to track particles inside the material, through the *run manager*, considering all possible interactions / decay processes and recording all the events that occur for each *run*, i.e. the set of all the phenomena occurring from the creation of a primary particle to the death of the last secondary particle stemming from it. The flexibility of this tool is emphasized also by the wide coverage of physical processes, whose description can be based on theoretical expressions, extended cross-section tables and empirical experiment-based formulae, which can combined in an arbitrary manner when modeling a particular process. It is important to stress that the user chooses the relevant physics processes and their underlying modelling description, the integrator in presence of an external macroscopic electromagnetic field, the GUI and visualization technologies, the histogramming and the persistency mechanism, according to the scenario of interest.

In this section, some basic concepts on the working principle of Geant4 [127, 128] are presented that are important for the understanding of its structure and performance.

G4Run

As an analogy with real experiments, a run of the GEANT4 program starts with the command line "Beam On". Within a run, that in general can include the generation of more than one primary particle, all independent of each other, the user cannot change neither the detector geometry nor the settings of the physics processes: the whole detector is inaccesible during a run.

G4Event

At the beginning of a simulation, an event contains the primary particles which are pushed into a stack. When the stack gets empty, the processing of an event terminates. This includes: list of primary vertexes and primary particles, trajectory collection (momentum and position at any time) and hits collection (list of all interactions).

G4Track

A track represents a "snapshot" of a particle trajectory, retaining information on the position, momentum, energy and time as well as the mass, charge, etc. It is deleted when the particle goes out the "world" volume, decays, or is cut off. It is clear that no tracks persist at the end of an event.

G4Step

A fraction of a track, in terms of information, is given by a step. It has two endpoints and also includes partial information about the particle (energy loss on the step, time-of-flight spent in the step, etc...). In case a step is limited by a volume boundary, the end point physically stands on that boundary and it logically belongs to the next volume. Fig.3.1 illustrates the modular, hierarchical structure of the GEANT4 kernel, where each category manages a component of the software and all the sub-domains are linked by a uni-directional flow of dependencies.

G4ParticleSource

The general particle source is a class that allow to specify the spectral, spatial and angular distribution of the primary source particles. This class has proven useful for the purpose of this thesis, allowing to generate the runaway electron beam and mimic its most important features. Specifically, the user can control:

- Spatial sampling on simple 2D or 3D surfaces;
- Angular distribution: unidirectional, isotropic, cosine-law etc.;
- Energy spectrum: linear, exponential, power-law, Gaussian, etc.

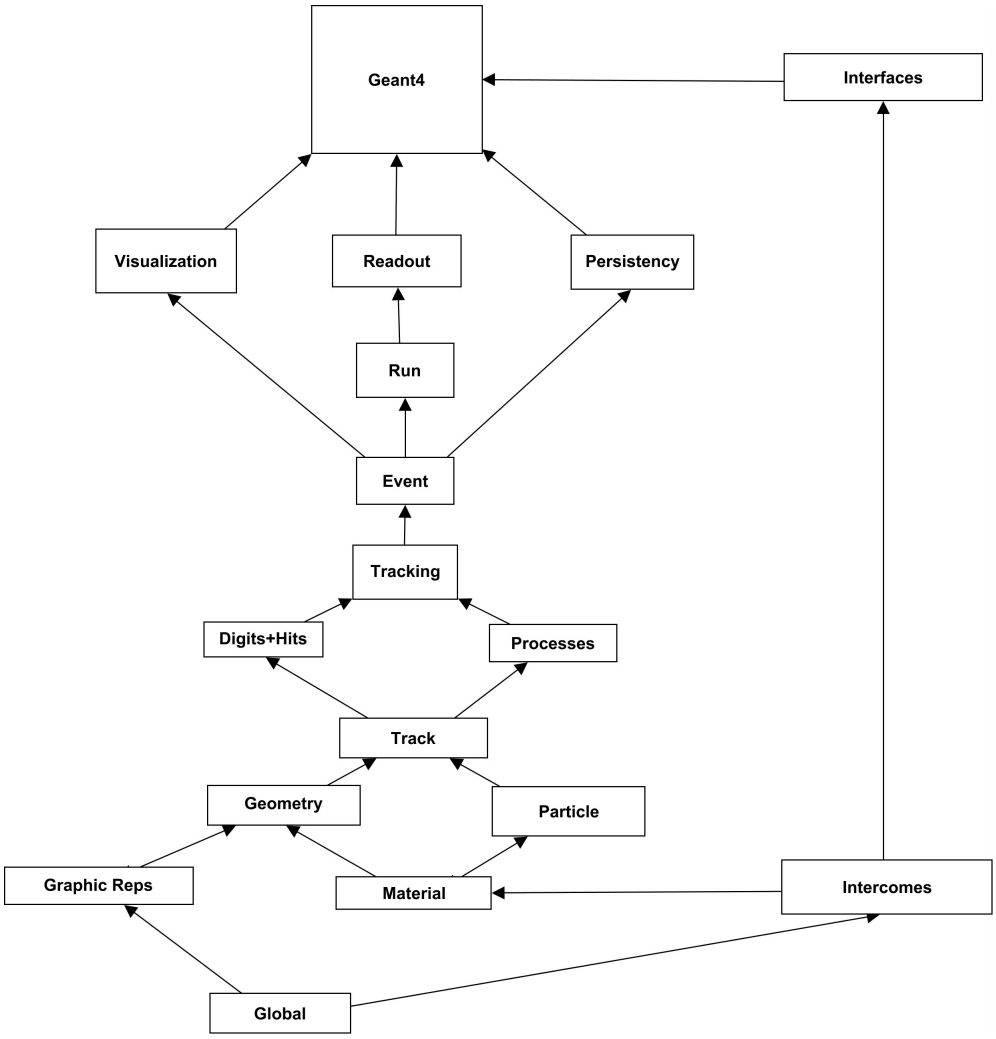

Figure 3.1: Category diagram of the GEANT4 architecture (top level). The arrow on the joining lines represents a using relationship, where the category at the arrow end uses the adjoined one. Adopted from Ref.[129].

3.2. The physics list class

The Physics List (PL) is one of the three mandatory user classes of the GEANT4 code. In this class, all particles of interest and their interaction processes should be defined. The toolkit offers the possibility to build a user-defined Physics List, or to adopt a reference Physics List, among the ones already included in the libraries, which are routinely validated and updated at each release. There are currently 28 built-in PLs, due to the many alternative physics models that can be implemented for the simulation of very different scenarios, ranging from hadronic physics to low energy or high-energy electromagnetic physics. A complete list of all the possibilities offered by GEANT4 is reported in the official website [117], with exhaustive explanations and covering a wide range of application. On the other side, if the user wants to have more flexibility and a complete control on the description of the physics processes, the user-defined PL can be adopted. In that case, one has to select, for all desired particles, the list of processes to be included as well as the models to describe them. GEANT4 has three basic types of physics processes:

1. *At rest process* (e.g. decay at rest), applied only for a particle at rest;
2. *Continuous process* (e.g. ionization), continuously applied along a step of a particle;
3. *Discrete process* (e.g. decay on the fly), called at the end point of a step.

Particle transportation is considered to be a process as well, by which a particle interacts with the geometrical volume boundaries and an external field of any kind. At each step, all processes listed for the specific considered particle are invoked to obtain the proposed physical interaction lengths.

GEANT4 also offers the possibility to manually select the cut-off for secondary particle production, so that tracks below a certain threshold are not followed anymore not to unnecessarily overload the computational effort. In contrast to the previous version (GEANT3), the cut-off can now be expressed through the length instead of the energy. For example, if the cut-off is set to be 1 mm, an electron whose expected range in the current material is less than 1 mm will not be created and its energy will be deposited locally. Moreover, the user can set different cut-offs for different particles according to the desired accuracy.

Finally, we comment on the implementation of the electromagnetic field. In general, GEANT4 allows the inclusion of a variety of fields: magnetic, electric or gravitational, both uniform or non-uniform in space, which can be specified according to the needs. In the presence of an external field, an integration of the equation of motion in the field is

performed, by default, using the Runge-Kutta method, although different solvers are also available at the discretion of the user. Moreover, for a uniform magnetic field, iterative methods might be used in order to converge to a more precise solution, if approximate analytic calculations are feasible.

3.3. Statistics

MC approaches require a meaningful statistical ensemble so that reliable results are obtained. A large enough number of particles should be launched at each run, whose number must be chosen so that the signal to noise ratio is decreased up to a level where fluctuations due to the random nature of the Monte Carlo methods do not influence the outcome of the simulation.

In simulations of volumetric heat deposition, one has to start from a volume discretization, namely to determine the 3-D mesh of the sensible domain, according to the desired accuracy. GEANT4 offers the possibility to create a 2D or 3D grid of controlled granularity and with different shape for the grid elements. For the scope of this thesis project, a cubic mesh has been adopted, whereas the number of bins, i.e. the size of the cubic cell, has been chosen according to the Continuous Slowing Down Approximation (CSDA) range at the specific energy of the considered primary particles (electrons in this case). Namely, the ESTAR database [130], which provides tabulated data for the CSDA range and stopping power of electrons penetrating a wide variety of elements and compounds [131], has been utilized. The data are expressed in g/cm^2, through a division for the selected material mass density, the CSDA range in units of length (cm) is obtained. Then, the domain of interest is subdivided into a cubic grid, where the size of each cell corresponds to one hundredth (1/100) of the CSDA range, to ensure sufficient spatial resolution, while the cut-off for secondary particle production is set to one tenth (1/10) of the cell size, i.e. to one thousandth (1/1000) of the CSDA range, not to overload the computational effort, but at the same time achieving a detailed volumetric energy deposition. Table 3.1 contains the relevant information concerning the materials studied in this thesis both for statistical assessment as well as for benchmarking purposes.

Next, a suitable statistical population is to be assessed. Specifically, when a GEANT4 run is launched with a number of electrons N, the code performs the simulation one primary particle at a time, while the energy deposition map is obtained by evaluating the energy left by each particle (both primaries and secondaries) in each of the cells belonging to the sensible volume and then summing them up. So, after calculating the average energy deposited $\bar{E}_{dep}$ cell by cell due to the passage of N primaries (and their products) and calculating the standard deviation σ_{dep} of the ensemble of N E_{dep} samples, the ratio can be employed to determine whether the number of primaries is sufficiently high to ensure an insignificant effect of fluctuations.

Material	CSDA range at 1 MeV [g/cm^2]	Density [g/cm^3]	Cell's size [μm]	Secondary cut-off [μm]
Beryllium	5.460E-01	1.85	2.95E+01	2.95E+00
Boron	5.362E-01	2.31	2.32E+01	2.32E+00
Carbon	4.964E-01	1.70	2.92E+01	2.92E+00
Yttrium	6.618E-01	4.47	1.48E+01	1.48E+00
Zirconium	6.661E-01	6.49	1.03E+01	1.03E+00
Molybdenum	6.748E-01	10.28	6.56E+00	6.56E-01
Indium	7.011E-01	7.31	9.59E+00	9.59E-01
Silver	6.896E-01	10.49	6.57E+00	6.57E-01
Cadmium	7.009E-01	8.65	8.10E+00	8.10E-01
Hafnium	7.657E-01	13.07	5.86E+00	5.86E-01
Tantalum	7.664E-01	16.65	4.60E+00	4.60E-01
Tungsten	7.686E-01	19.25	3.99E+00	3.99E-01
Platinum	7.800E-01	21.40	3.64E+00	3.64E-01
Gold	7.762E-01	19.30	4.02E+00	4.02E-01
Lead	7.843E-01	11.34	6.92E+00	6.92E-01

Table 3.1: List of studied materials together with their properties (CSDA range and density) and simulation parameters (cell size and secondary cut-off).

This quantity is determined for the first 1000 cells with the highest average energy deposited $\bar{E}_{dep}$ in the cubic sensible volume, whose length of the order of the CSDA range. The plots in Fig.3.2 show the ratio of $\sigma_{dep}/\bar{E}_{dep}$ as a function of the cell number (ordered from 1 to 1000 as the average energy deposited is decreasing) for three particle numbers: 10^4, 10^5 and 10^6. Carbon (low Z) is considered on the upper panel, tungsten (high Z) on the lower panel, while the energy of the impinging electrons is set to 1 MeV.

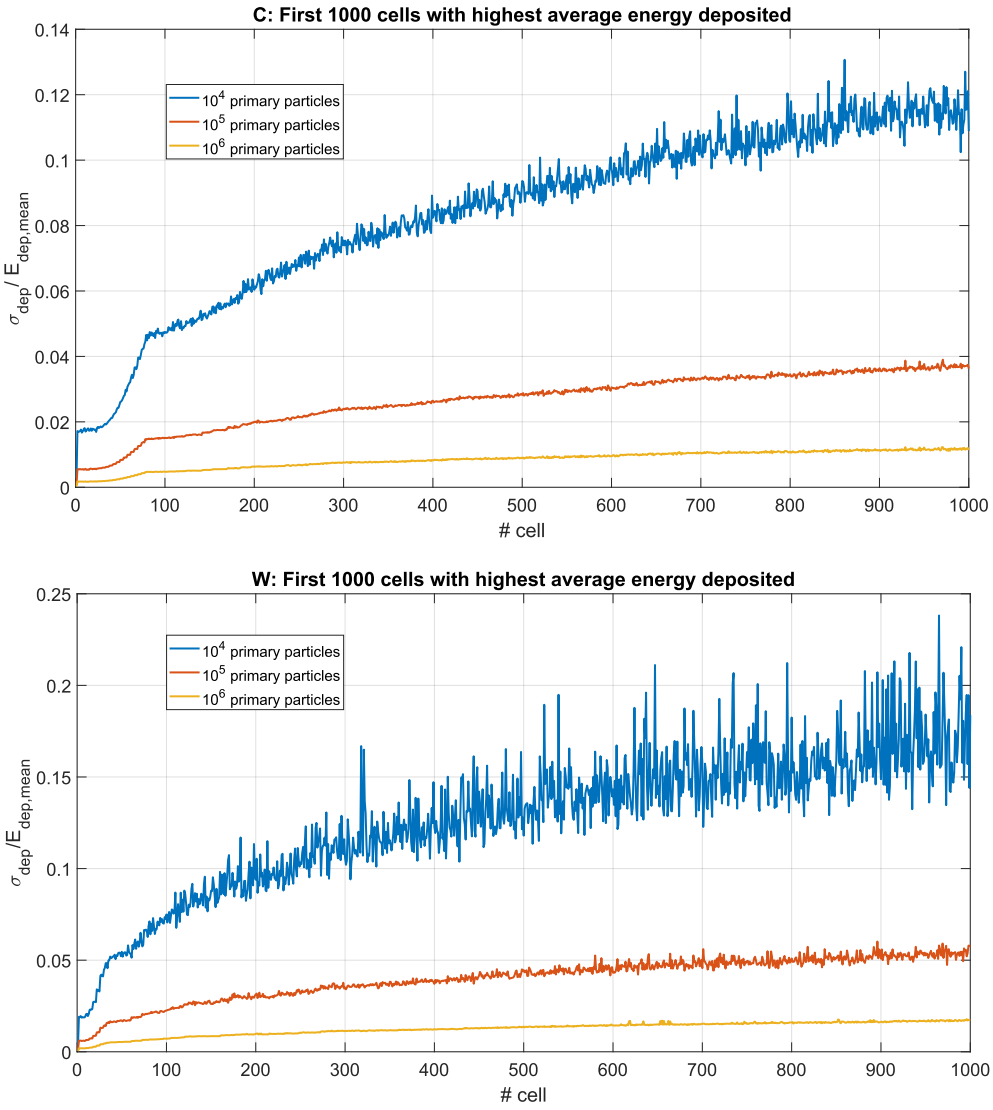

Figure 3.2: Ratio between standard deviation and average energy deposited in the first 1000 cells with highest average energy deposited. Carbon (upper panel) and Tungsten (lower panel) for different primary electron populations.

It is evident, that the fluctuations are significant for N=10^4 electrons, i.e. the standard deviation in the energy is non negligible with respect to the average energy value. On the other hand, when increasing to N=10^5 , the situation improves significantly. Thus, this value will be utilized for the benchmarking runs, providing a good compromise between accuracy and computational time. However, for production runs and simulations of real case scenarios, N=10^6 is the desired sample size.

4 | Validation activities

A peculiarity of the GEANT4 code compared to other commercial MC codes concerns the large amount of physical models that are available for the description of the same physical interaction. In addition, multiple updates are associated with each new version in order to minimize software bugs and implementation errors. Moreover, different physical models have variable sensitivities on the energy range and the target composition. Thus, the optimal model could depend on the specific application.

Given the above, it is apparent that rigorous validation activities are necessary to ensure that GEANT4 predictions are reliable. Therefore, benchmark tests constitute a central part of the present project. Apart from a comparison with available experimental data, the goal is also to quantify the sensitivity of the final results to different implementations and different physics models that describe the interactions mentioned in Chapter 2. Such an understanding will allow a degree of flexibility and accuracy control in the course of predictive studies.

The selected benchmark tests concern calorimetry measurements of the energy deposition profile and electron collection measurements of the backscattering yield. For both validation activities, a large number of materials (low-Z, medium-Z, high-Z) will be considered and an extended energy range will be probed, in accordance with what the literature provides.

This chapter aims to establish the most suitable physics libraries for charged particle and photon interactions but also to compare the available implementations of scattering events (single, mixed, multiple), since the computational cost should be considered in parallel with the accuracy. Table 4.1 reports a summary of the physics libraries employed, while Table 4.2 summarizes the available scattering models.

Library	Processes	Specifics
PENELOPE	Ionisation	electrons/positrons
	Bremsstrahlung	electrons/positrons
	Annihilation	positrons
	Gamma conversion	photons
	Photoelectric effect	photons
	Compton scattering	photons
	Rayleigh scattering	photons
Livermore	Ionisation	electrons
	Bremsstrahlung	electrons
	Gamma conversion	photons
	Photoelectric effect	photons
	Compton scattering	photons
	Rayleigh scattering	photons
G4StandardEm	standard electromagnetic processes	photons / leptons
	Bertini cascade for hadrons below ∼10 GeV	barions / mesons
	QGS model for high energies (> 20 GeV)	ions
G4StandardEmSS	Single elastic scattering	Mainly for validation
	for all charged particles	and verification

Table 4.1: List of the physics libraries employed, including the physics interactions.

Scheme	Model
Single scattering	Coulomb scattering model
	Single Coulomb scattering model
Multiple scattering	Urban model
	UrbanII model
	Goudsmit&Saunderson model
Mixed scheme	WentzelVI model

Table 4.2: List of the scattering models employed, classified by scheme.

4.1. Benchmarking against calorimetry experiments

Given the foreseen application to the volumetric energy dissipation of REs, it is natural that energy deposition measurements are selected for the first set of benchmarking activities. High precision measurements were performed at the Sandia National Laboratories [132–136] with electron beams of energies from tens of keV up to 1 MeV impinging on different materials. The goal was to provide experimental data for the benchmarking of the ITS code, one of the first MC codes for coupled electron-photon transport [137].

The experimental realization concerned the longitudinal distribution of electron energy deposited in a segmented calorimeter. An electron accelerator delivered near mono-energetic electron beams with a nominal energy corresponding to 1, 0.5, 0.3, 0.1, 0.05 MeV and a related uncertainty of 0.1%. The target was configured as a semi-infinite geometry, with a thickness larger than the depth range of the most energetic incident electrons and sufficiently wide to contain the resulting electromagnetic shower (except for possible transverse leakages of Bremsstrahlung generated photons). A front slab of "passive" material was followed by a calorimeter and a so-called "infinite plate", all realized with the same material composition. By varying the thickness of the first layer, the energy deposited could be determined as a function of the depth. A schematic representation is illustrated in Fig.4.1. A more detailed description of the experimental set up is provided in the above references. It is noted that the longitudinal direction was expressed as a fraction of the CSDA depth range at the precise energy of the incoming electron beam.

From the simulation point of view, a specific application tool has been built. The target is modeled as a cube, whose edge length is chosen to exceed the electronic depth range at the incident energy of interest. In particular, for some materials, the length is chosen to reach up to 150% of the CSDA range, so that the electromagnetic shower is effectively contained within the target. Mesh generation is important, since rough rendering might lead to misinterpretation and inaccuracies in the outcome of the simulations, as stated in Ref.[138]. As discussed in the previous chapter, a cubic discretization equal to 1/100 of the CSDA range and a secondary cut-off set to 1/10 of the cell size is adopted. The benchmarking activities focused on normal electron beam incidence, i.e. the beam angle in Fig.4.1 is always equal to zero. The energy deposition in the longitudinal direction is obtained by summing the energy deposited in each plane (with the thickness of a cell) perpendicular to the incident electron.

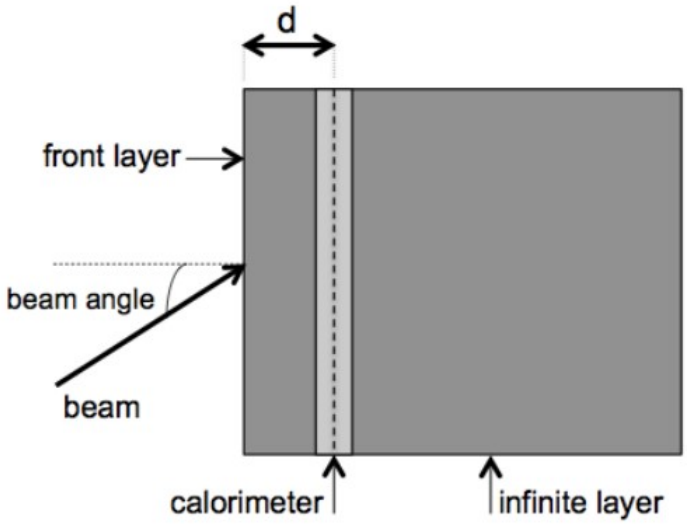

Figure 4.1: Sketch of the geometrical configuration corresponding to the experimental set-up of Ref.[132] for the measurement of the longitudinal energy deposition of high energy electrons. Adopted from Ref.[139]. The dimension designated by "d" represents the depth at which the energy deposition is measured.

Table 4.3 contains a list of all simulated materials and incident electron energies. Several sets of GEANT4 simulations were performed by modifying the PhysicsList; different libraries are combined with different scattering implementations. It was also verified that Auger and radiative de-excitation processes do not affect the energy deposition. Thus, in all the tested scenarios, the time-consuming atomic relaxation processes were disabled, reducing the computational cost. Moreover, as aforementioned, the statistics concern 10^5 electrons. Finally, it is noted that the standard deviation of the experimental data is not represented by the usual error bars, but is instead included in the dimension of the black dots.

Material	**Energies [MeV]**
Beryllium	0.1 0.3 0.5 1.0
Carbon	1.0
Molybdenum	0.1 0.3 0.5 1.0
Tantalum	0.3 0.5 1.0

Table 4.3: List of the material - electron beam combinations considered in the calorimetry validation tests.

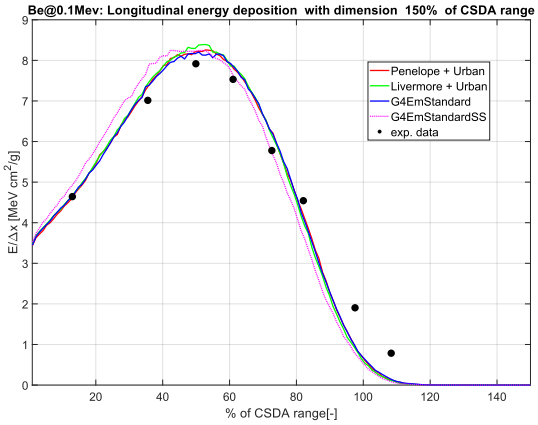

Figure 4.2: Beryllium @ 0.1 MeV

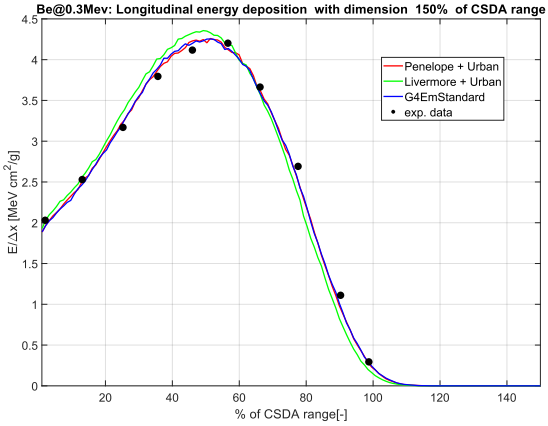

Figure 4.3: Beryllium @ 0.3 MeV

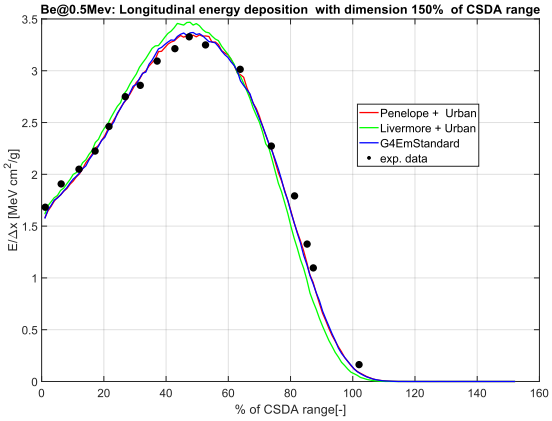

Figure 4.4: Beryllium @ 0.5 MeV

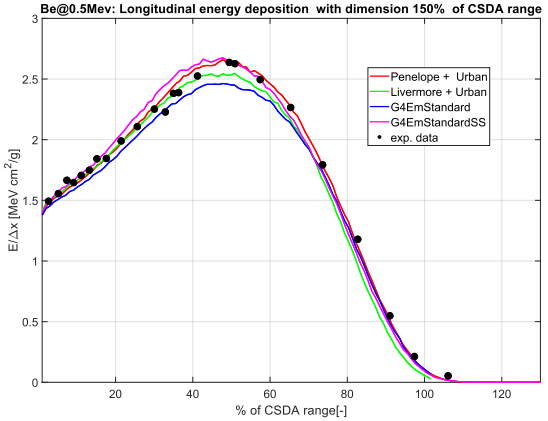

Figure 4.5: Beryllium @ 1.0 MeV

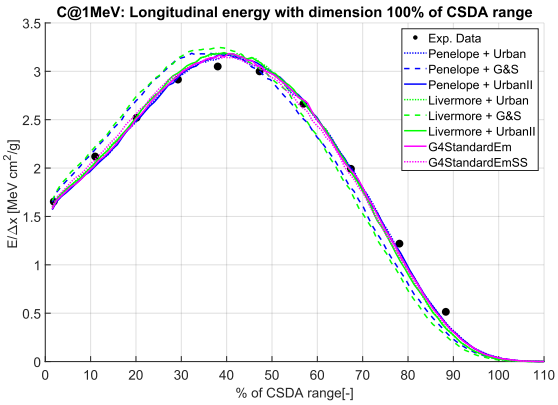

Figure 4.6: Carbon @ 1.0 MeV

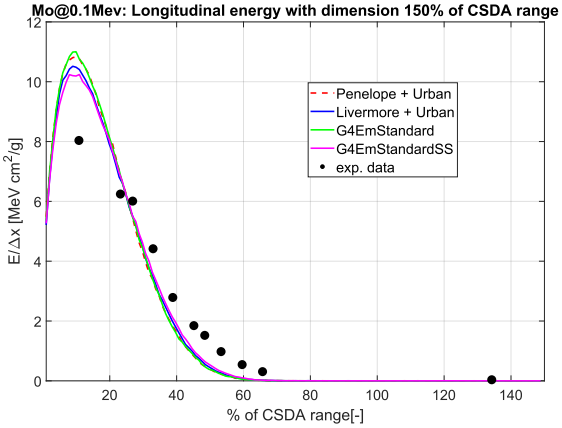

Figure 4.7: Molybdenum @ 0.1 MeV

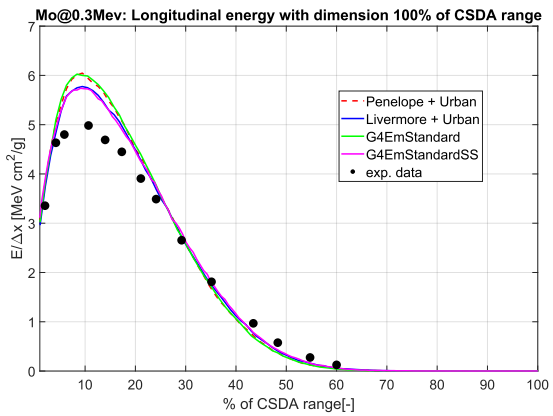

Figure 4.8: Molybdenum @ 0.3 MeV

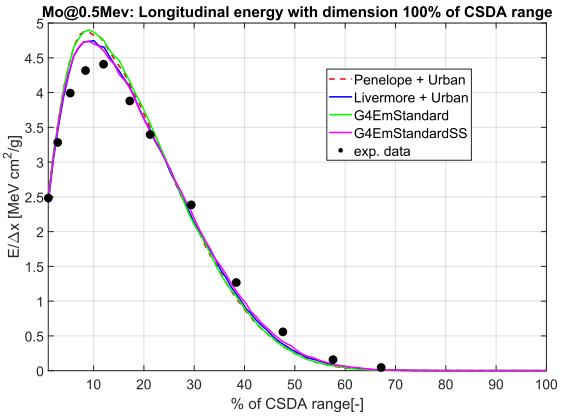

Figure 4.9: Molybdenum @ 0.5 MeV

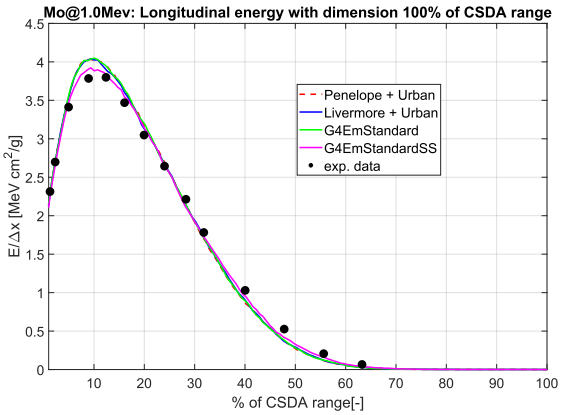

Figure 4.10: Molybdenum @ 1.0 MeV

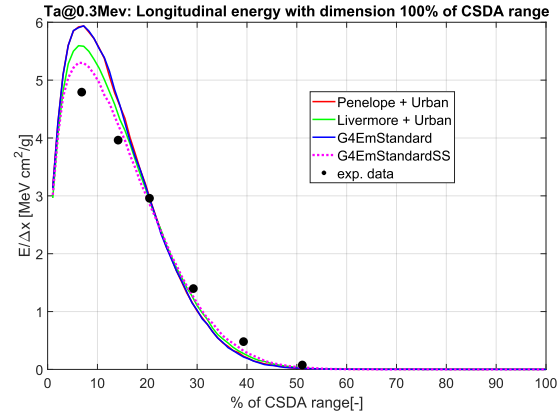

Figure 4.11: Tantalum @ 0.3 MeV

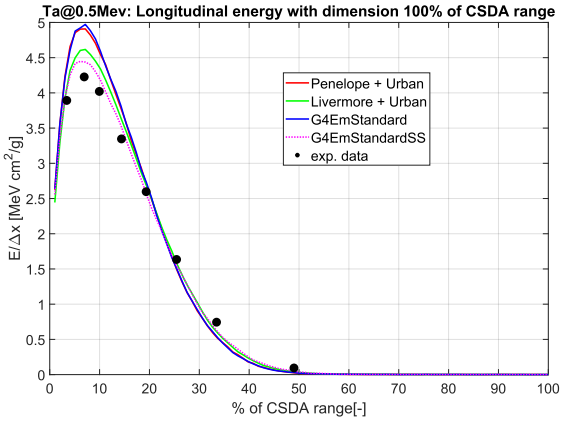

Figure 4.12: Tantalum @ 0.5 MeV

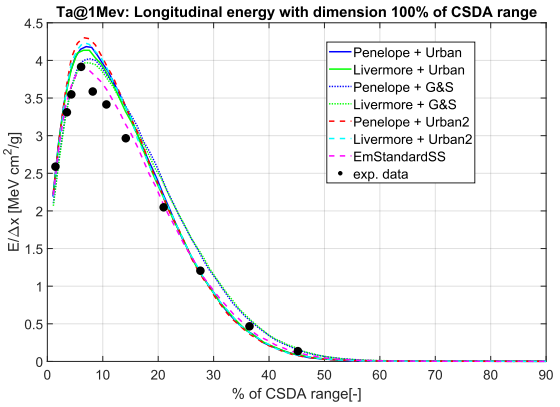

Figure 4.13: Tantalum @ 1.0 MeV

Furthermore, an investigation of the accuracy and computational cost of mixed MC simulations has been carried out, based on the Wentzel theory. In the respective GEANT4

implementation, the presence of both a multiple scattering model (G4WentzelVIModel) and a single scattering model (G4eCoulombScatteringModel in this case) is required. The implementation also involves a user-defined angular threshold Θ_{lim}, with interactions that lead to scattering angles above this threshold being simulated as a single scattering process and with interactions that lead to scattering angles below this threshold being simulated in a condensed manner. Consequently, by varying the angular threshold from the maximum of 180°, corresponding to a multiple scattering run, to the minimum of 0°, corresponding to a single scattering run, the sensitivity and accuracy of the energy deposition profile can be observed. The different curves obtained are shown in Fig.4.14 and Fig.4.15, where the Wentzel model is first coupled to the PENELOPE library and then to the Livermore library. For the sake of completeness, the effect on the computational cost has also been investigated, with the simulation duration reported in Table 4.4.

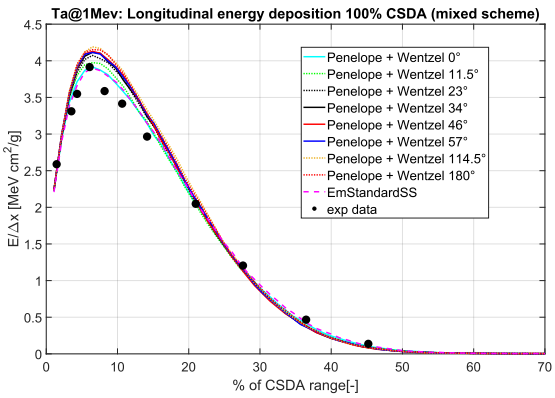

Figure 4.14: Tantalum @ 1.0 MeV Wentzel model combined with the PENELOPE library.

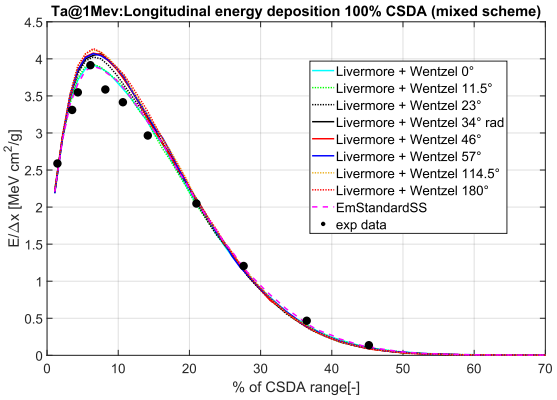

Figure 4.15: Tantalum @ 1.0 MeV Wentzel model combined with the Livermore library.

Θ_{lim} [deg]	Run time (PENELOPE)	Run time (Livermore)
180	3 min.	3 min.
114.5	4 min.	3 min.
57	4 min.	5 min.
46	15 min.	18 min.
34	26 min.	26 min.
23	28 min.	29 min.
11.5	46 min.	51 min.
0	3 h. 45 min.	3 h. 54 min.

Table 4.4: Scaling of the computational time with the threshold angle in Wentzel-based mixed schemes.

The focus is mainly on two available models in the GEANT4 physics library: the PENELOPE and Livermore. These are manually implemented by the user and will be compared with the already compiled physics lists, i.e. G4EmStandard and G4EmStandardSS, the last used to test the single scattering implementation.

For low-Z metals (Be, C), nearly all simulation sets accurately reproduce the experimental data; there are small deviations that are confined to large depths and there is a small overshoot of the extended maximum which is located at approximately half the CSDA range. The PENELOPE+Urban set is nearly indistinguishable from the G4EmStandardSS simulations. The Livermore+Urban set is less accurate with the small deviations concentrated in the vicinity of the energy deposition maximum.

For medium-Z metals (Mo), no simulation is able to reliably reproduce the lowest incident energy results (0.1 and 0.3 MeV). The situation improves as the incident energy increases, at 1.0 MeV all combinations accurately reproduce the experimental data. In this case, the Livermore+Urban set is nearly indistinguishable from the G4EmStandardSS simulations, while the PENELOPE+Urban set is less accurate with the small deviations exclusively confined to the vicinity of the energy deposition maximum.

For high-Z metals (Ta), there are marked differences between the single scattering and multiple scattering implementations that are again mainly concentrated near the maximum. The G4EmStandardSS simulations are the most reliable with their level of accuracy increasing with the incident energy. The Livermore+Urban set is more accurate than the PENELOPE+Urban set. Alternative multiple scattering implementations do not improve the agreement with the experimental data.

Finally, let us discuss the performance of mixed simulations that are based on the Wentzel theory, where the scattering cross section is calculated with the assumption of a screened Yukawa potential [140], for 1.0 MeV electrons normally incident on Ta. It is evident that the neighbourhood of the maximum is controlled by the angular cut-off whose value does not affect the asymptotic behavior. As the threshold is decreased, the respective curve gradually moves from the multiple scattering curve to the single scattering curve. For both the PENELOPE and the Livermore libraries, it is observed that angular thresholds of the order of 10° in the mixed implementation lead to indistinguishable results compared to the single scattering implementation, at a fraction (roughly one fifth) of the computational cost.

Overall, the observed trends suggest that the experimental data can be reproduced more accurately at incident energies in the MeV range and for low-Z materials; the simulations tend to overshoot the energy deposition peak at low energies and high atomic numbers. In

addition, the differences between multiple, mixed and single scattering implementations are important only in the case of low energies and for high-Z materials. In the light of the unavoidable uncertainties that are associated with the RE energy range and intensity, it can be safely concluded that computationally efficient multiple scattering implementations suffice.

4.2. Benchmarking against backscattering experiments

The electron backscattering yield η constitutes an observable that is very sensitive on the numerical implementation of elastic scattering events (single/mixed/multiple scattering) [141]. Given the fact that the scattering implementation controls the computational cost, electron backscattering has been selected for the second set of benchmarking activities.

The incidence of an electron beam on the surface boundary of condensed matter (solids, liquids) is typically accompanied by the re-emergence of electrons, a phenomenon known as *electron-induced electron emission* (EIEE). There are three major processes that contribute to EIEE [142, 143]. In *secondary electron emission* (SEE), the emitted electrons correspond to bound electrons that were excited by the incident electrons, see the ionization-excitation losses [144, 145]. In *electron backscattering* (EBS), the emitted electrons correspond to incident electrons that were inelastically reflected in the material interior [146, 147]. In *low energy electron reflection* (LEER), the emitted electrons correspond to incident electrons that were quasi-elastically quantum-mechanically reflected at the material interface [148–150]. Each process is quantified by its respective emission yield that is simply defined as the average number of the emitted electrons belonging to the process of interest over the number of incident electrons and that strongly depends on the incident energy, the incident angle and the material composition [55, 151, 152]. For instance, the EBS yield η is naturally defined by the ratio between the total number of backscattered electrons to the total number of incident electrons

$$\eta = \frac{N_{BSE}}{N_{inc}} \,. \tag{4.1}$$

Depending on the incident electron energies of interest, a single process can dictate the overall EIEE electron fluxes. EBS is dominant above 10 keV, SEE is dominant within 0.1-2 keV and LEER is prominent below 10 eV. The three emitted electron groups are characterized by different energy distributions [151, 153]; reflected electrons have mean exit energies very close to the incident electron energies, backscattered electrons have mean exit energies of the order of 2/3 of the incident electron energies and secondary electrons have mean exit energies of the order of two times the work function. There is an asymptotic overlap between the energy distributions of the backscattered electrons and the secondary electrons, which is negligible provided that the incident electron energies are larger than 100 eV. The experimental convention is that all emitted electrons with energies below 50 eV are classified as secondaries and all emitted electrons with energies above 50 eV are classified as backscattered [153]. The distinction can be easily realized by

biasing the electron collector at a negative voltage of $-50\,\mathrm{eV}$.

After this introduction, let us exclusively focus on electron backscattering. It is noted that EBS is central to different scanning electron microscopy (SEM) techniques such as Electron Backscatter Diffraction for the characterization of the crystallographic structure and Backscattered Electron Imaging for the characterization of the material composition. It is emphasized that, given the respective electronic depth ranges, the EBS yields within the keV range and especially the sub-keV range are very sensitive to the surface conditions. Thus, reliable measurements of the EBS yield of pure materials require not only very high purity specimen and effective pre-cleaning methods but also ultra-high vacuum conditions and provisions for in-situ surface cleaning [145, 154]. In the low energy range, $0.2 - 5\,\mathrm{keV}$, the normal incidence measurements of Bronshtein–Fraiman [151] and El Gomati–Walker [155] have been selected as reliable, since they combine ultra-high vacuum with in-situ cleaned samples (evaporated films and Argon sputtering, respectively). In the less demanding intermediate energy range, $5 - 100\,\mathrm{keV}$, the normal incidence measurements of Hunger–Kuchler [156], Heinrich [157], Reimer–Tollkamp [158], Drescher [159] and Cosslett–Thomas [160] as well as the oblique incidence measurements of Neubert–Rogaschewski [161] have been selected as reliable. In the high energy range, $0.1 - 15\,\mathrm{MeV}$, the Tabata ionization chamber measurements [162] at normal incidence have been selected as reliable.

Considering the application to RE termination on plasma-facing components (Be, C, Mo, W), the materials of interest concern low-Z metals (Be, B, C), medium-Z metals (Y, Nb, Zr, In, Ag, Cd, Mo) and high-Z metals (Hf, Ta, W, Pt, Au). At normal incidence, the primary electron energy is scanned from $0.1\,\mathrm{keV}$ up to $15\,\mathrm{MeV}$. Within the keV range, the electron angle of incidence is scanned from $0°$ to $85°$. Table 4.5 contains a list of all simulated materials and incident electron parameters.

From the simulation point of view, a specific application tool has been built. The target dimensions are chosen to exceed the electronic depth range at the incident energy of interest. Outside the target and at the side of electron incidence, a detector is placed that is able to capture all the backscattered electrons and that obtains information on their energy and angular distribution. By utilizing the GEANT4 "step" class, it is possible to isolate those emitted electrons whose energy is above $50\,\mathrm{eV}$. It is noted that, in contrast to the calorimetry runs, Auger and radiative de-excitation processes have been enabled in the backscattering runs.

Material	Low energy 0.1 - 50 keV	High energy 1 - 15 MeV	Angular incidence 0° - 85°
Beryllium		✓	✓
Boron	✓		
Carbon	✓	✓	✓
Yttrium	✓		
Niobium			✓
Zirconium	✓		
Indium	✓		
Silver	✓	✓	✓
Cadmium	✓		
Molybdenum	✓		
Hafnium	✓		
Tantalum	✓		✓
Tungsten	✓		
Platinum	✓		
Gold	✓	✓	✓

Table 4.5: List of the material - electron beam combinations considered in the backscattering validation tests.

In order to eliminate spikes due to statistical fluctuations and to ensure a smooth behavior in the EBS yield curves as a function of the incident electron energy and the angle of incidence, the statistics have been increased to 10^6. The uncertainty of the experimental data is adopted from the respective references (when available), while the uncertainty of the GEANT4 data is calculated in a post-processing analysis. Both uncertainties are represented by error bars that are often not visible to the naked eye.

Aiming to understand the sensitivity to the scattering implementation, three sets of GEANT4 simulations are carried out for each material, incident electron energy and incident electron angle combination. The three sets utilize: (1) a pure multiple scattering model (Urban) combined with the PENELOPE library, (2) a Coulomb single scattering model combined with the PENELOPE library, (3) the G4EmStandardPhysicsSS library.

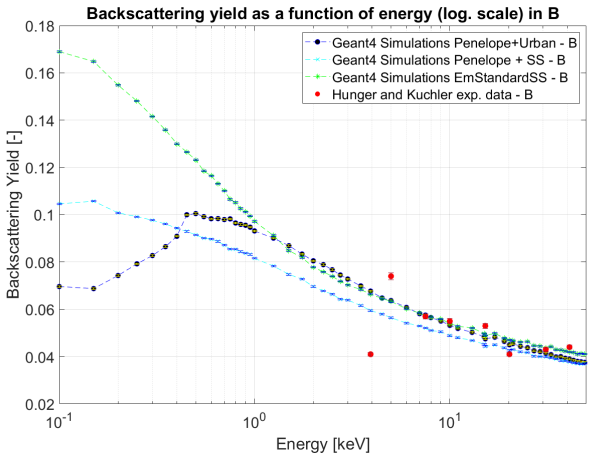

Figure 4.16: B, normal incidence, keV range

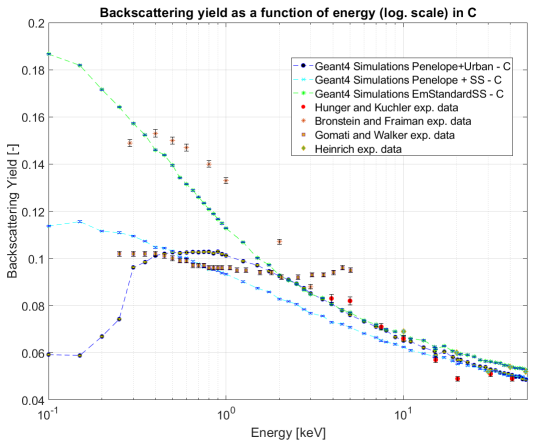

Figure 4.17: C, normal incidence, keV range

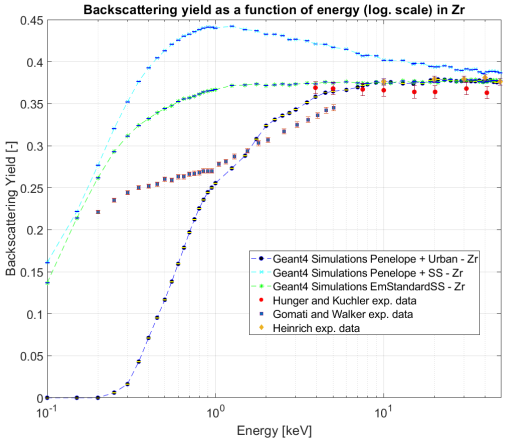

Figure 4.18: Zr, normal incidence, keV range

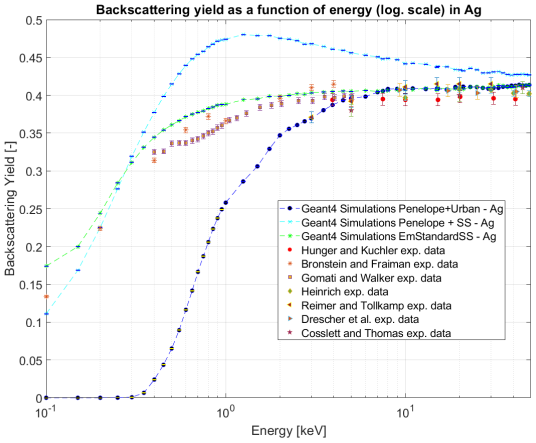

Figure 4.19: Ag, normal incidence, keV range

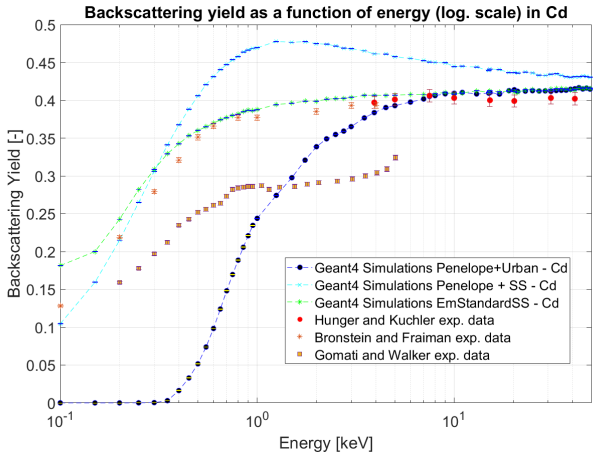

Figure 4.20: Cd, normal incidence, keV range

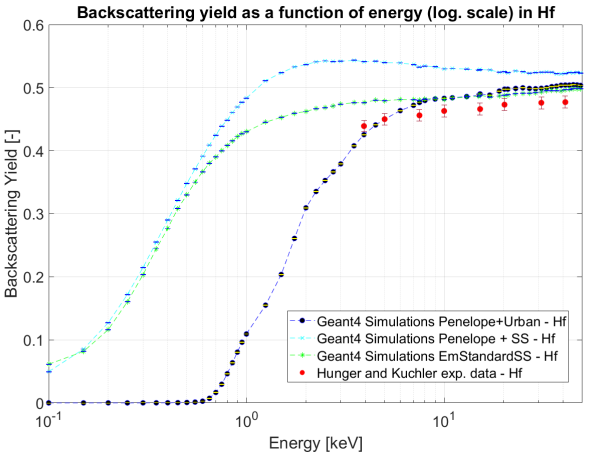

Figure 4.21: Hf, normal incidence, keV range

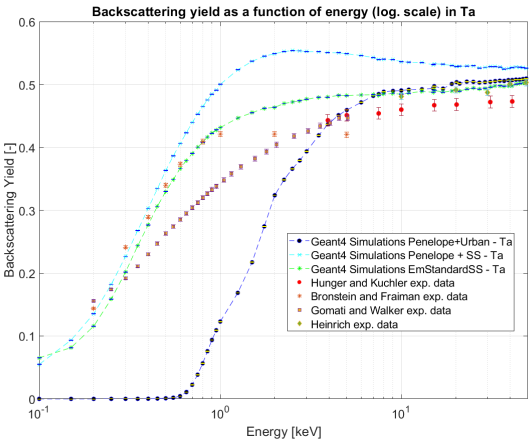

Figure 4.22: Ta, normal incidence, keV range

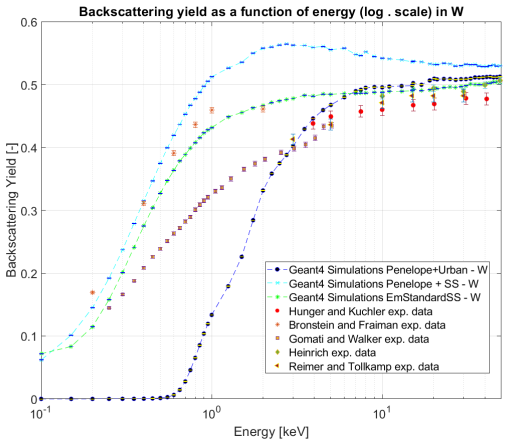

Figure 4.23: W, normal incidence, keV range

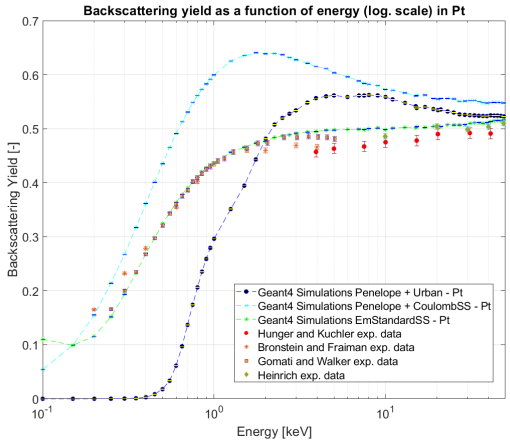

Figure 4.24: Pt, normal incidence, keV range

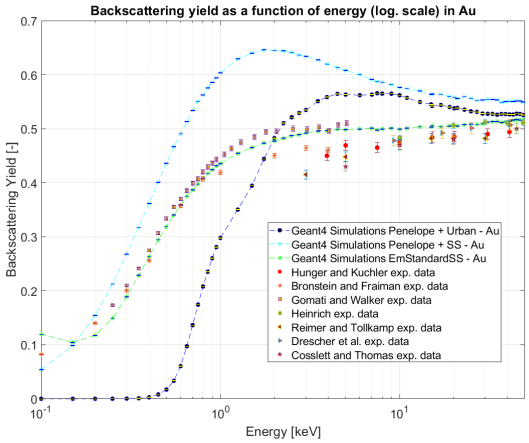

Figure 4.25: Au, normal incidence, keV range

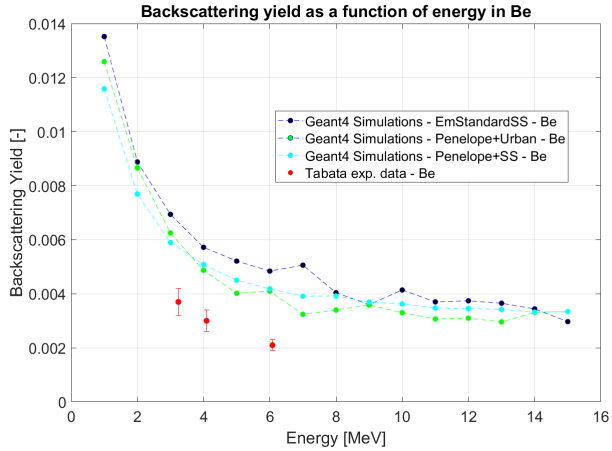

Figure 4.26: Be, normal incidence, MeV range

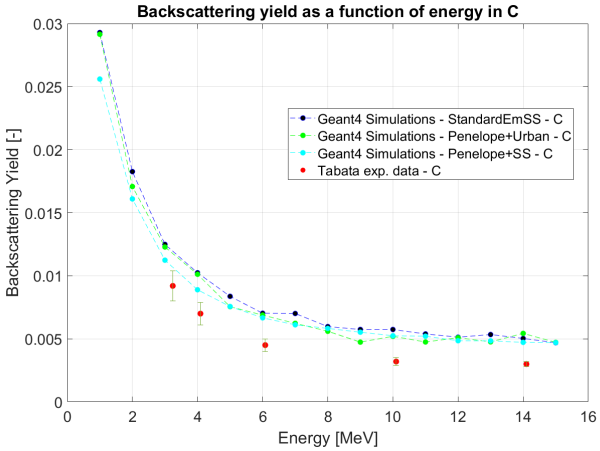

Figure 4.27: C, normal incidence, MeV range

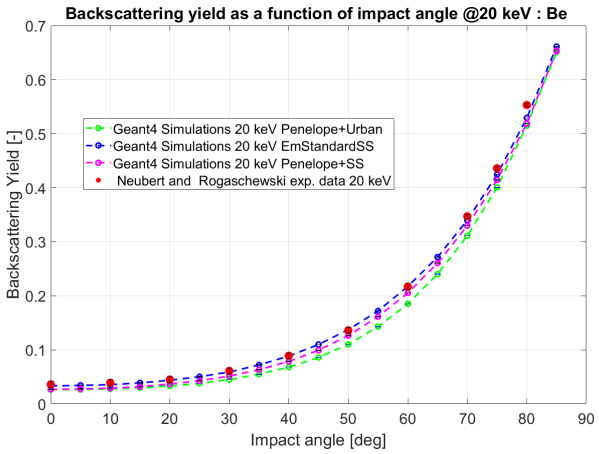

Figure 4.28: Be, angular incidence @20 KeV

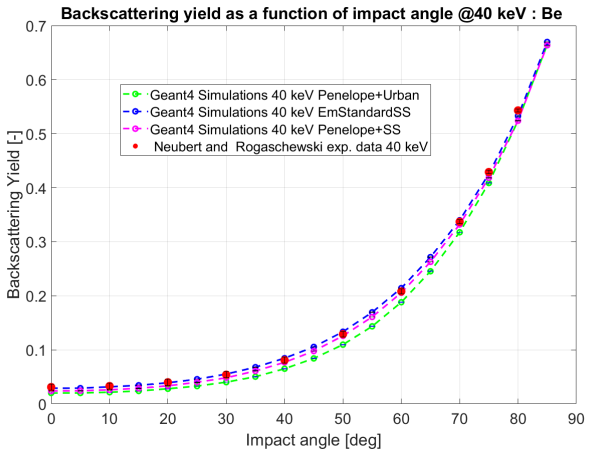

Figure 4.29: Be, angular incidence @40 KeV

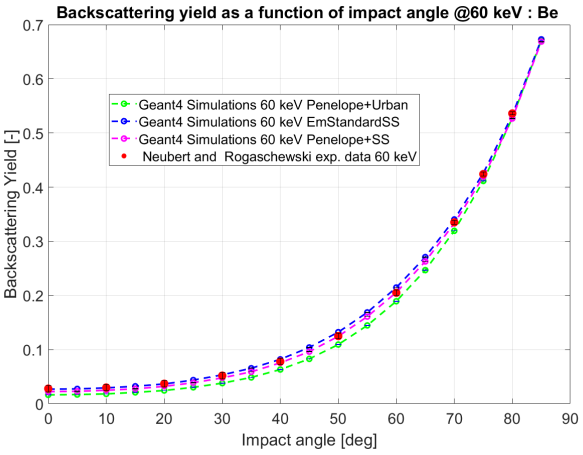

Figure 4.30: Be, angular incidence @60 KeV

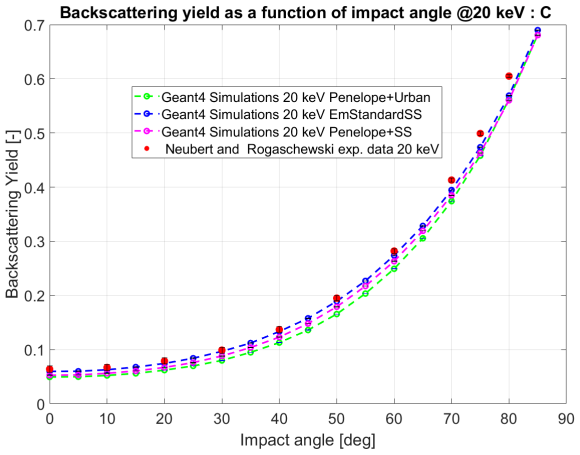

Figure 4.31: C, angular incidence @20 KeV

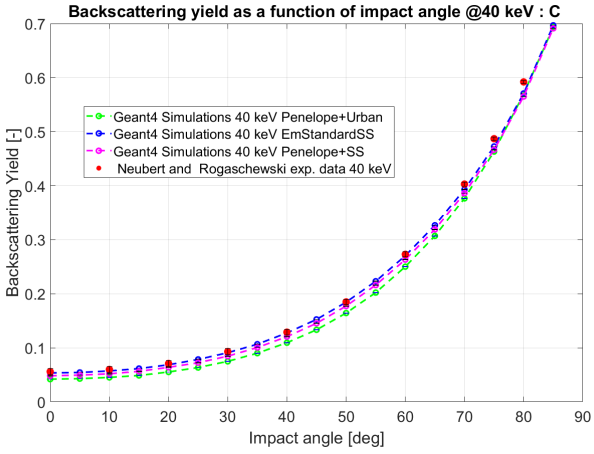

Figure 4.32: C, angular incidence @40 KeV

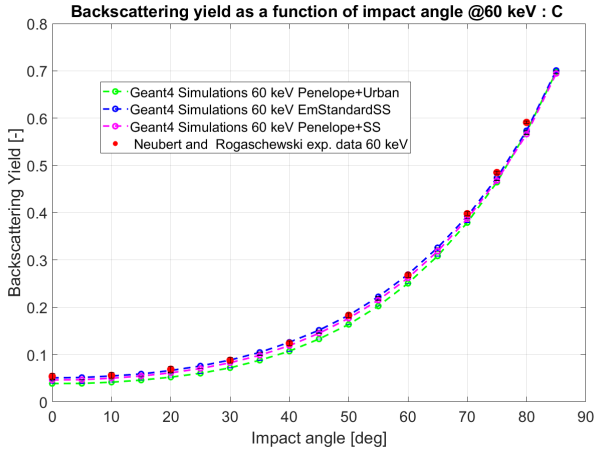

Figure 4.33: C, angular incidence @60 KeV

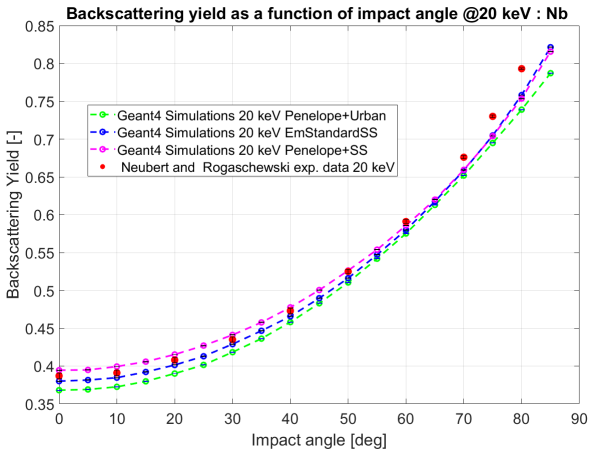

Figure 4.34: Nb, angular incidence @20 KeV

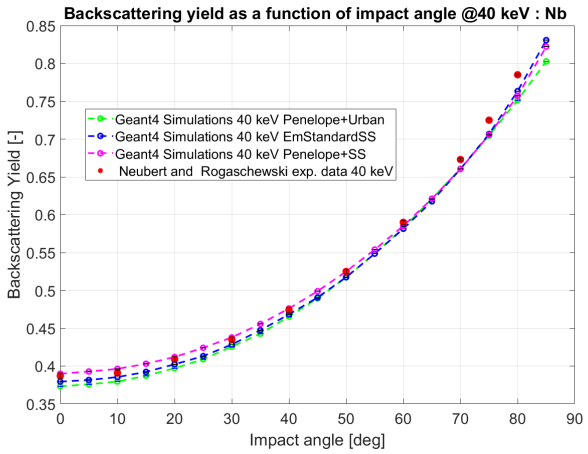

Figure 4.35: Nb, angular incidence @40 KeV

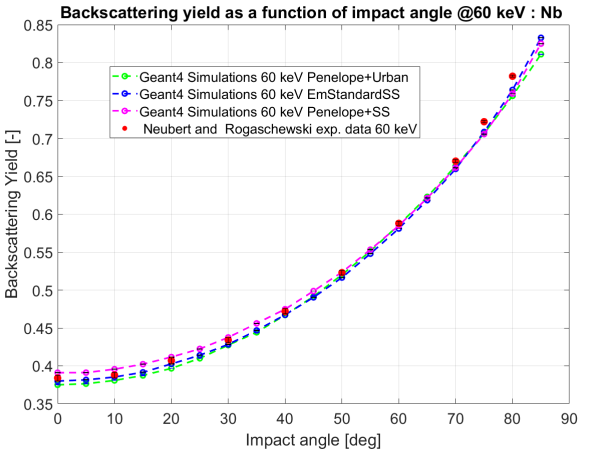

Figure 4.36: Nb, angular incidence @60 KeV

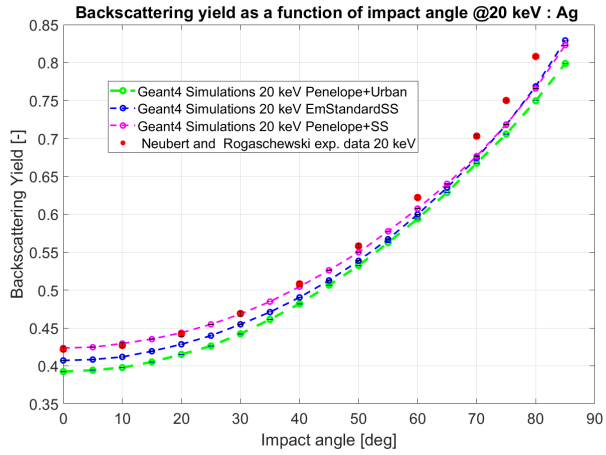

Figure 4.37: Ag, angular incidence @20 KeV

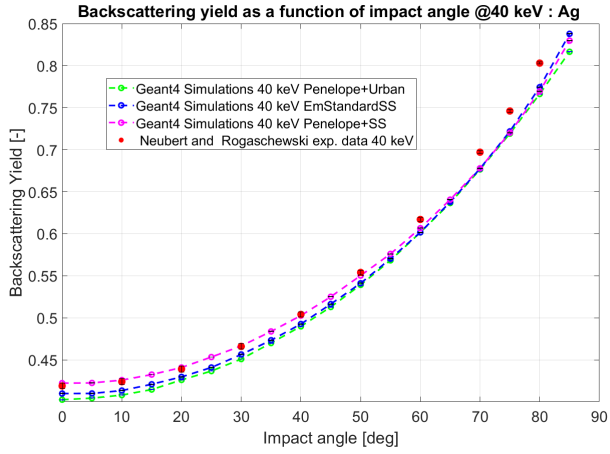

Figure 4.38: Ag, angular incidence @40 KeV

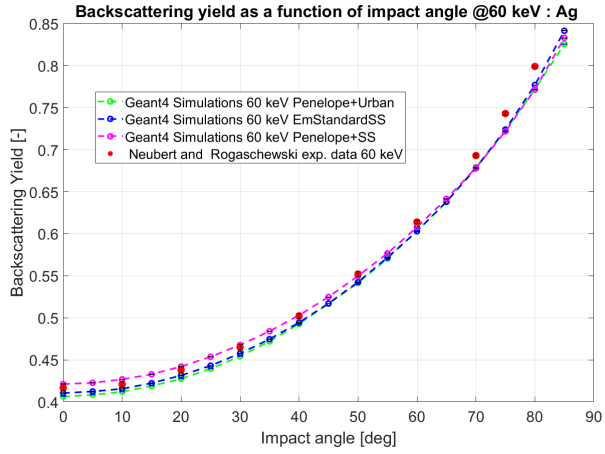

Figure 4.39: Ag, angular incidence @60 KeV

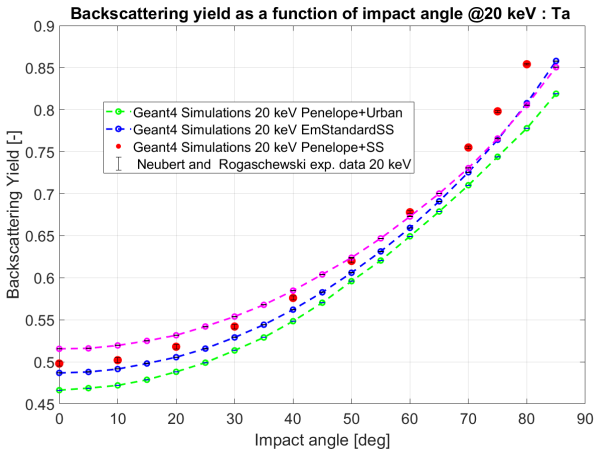

Figure 4.40: Ta, angular incidence @20 KeV

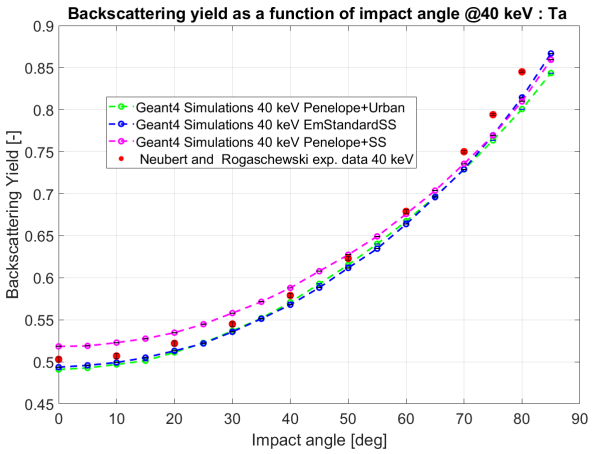

Figure 4.41: Ta, angular incidence @40 KeV

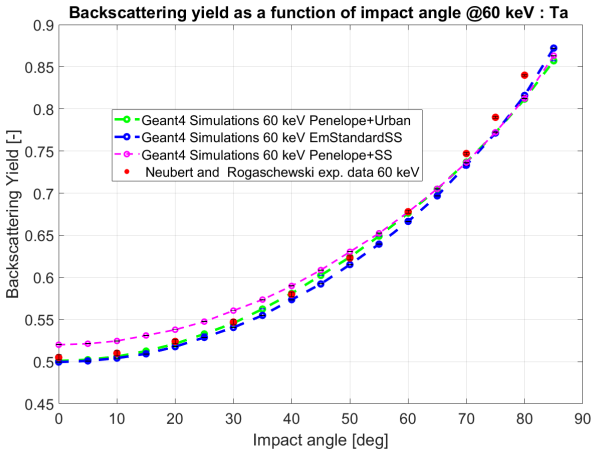

Figure 4.42: Ta, angular incidence @60 KeV

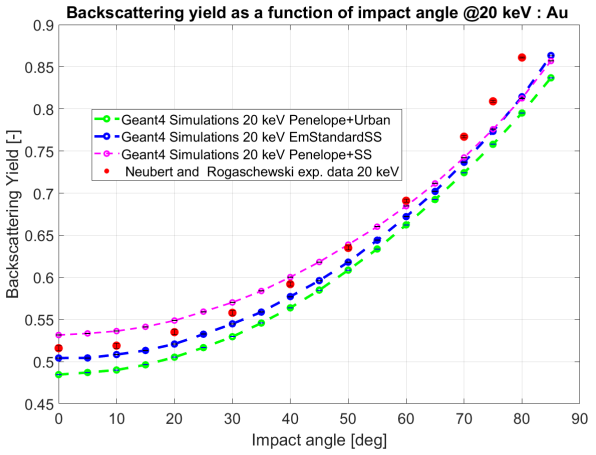

Figure 4.43: Au, angular incidence @20 KeV

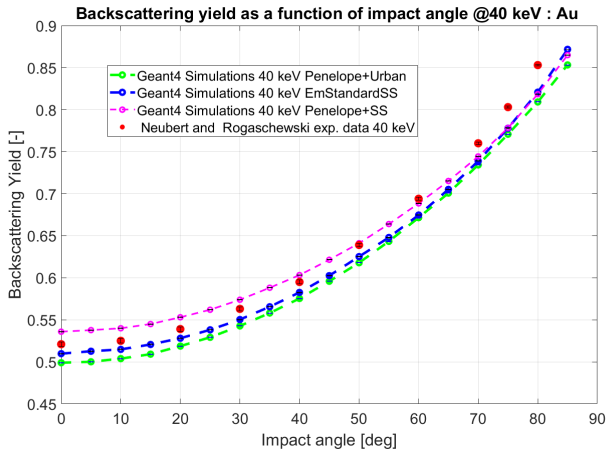

Figure 4.44: Au, angular incidence @40 KeV

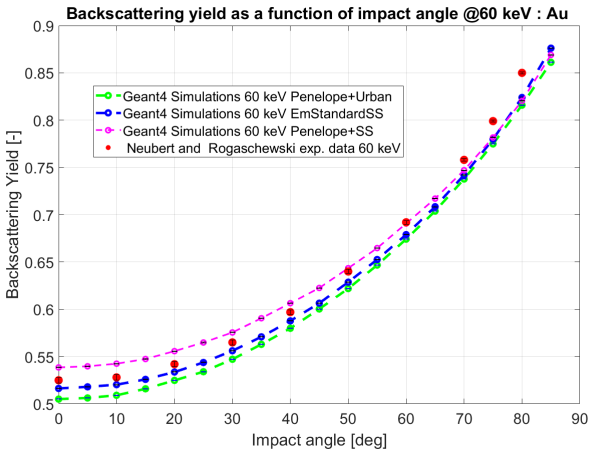

Figure 4.45: Au, angular incidence @60 KeV

We begin our discussion with the general trends that characterize the dependence of the EBS yield on the incident energy and incident angle. *At normal incidence*; In the sub-keV range, the EBS yield of low-Z elements has a shallow local maximum, while the EBS yield of medium-Z and high-Z elements is monotonically increasing with the incident energy. In the keV range, the EBS yield of low-Z elements is monotonically decreasing at a weak rate, while the EBS yield of medium-Z and high-Z elements is nearly independent of the incident energy. In the MeV range, regardless of atomic number, the EBS yield is monotonically decreasing with the incident energy seemingly reaching zero at asymptotically high energies. *At any given incident energy*, regardless of atomic number, the EBS yield is a monotonically increasing function of the incident angle reaching a value close to unity at near tangential incidence. This is a rather intuitive outcome, since, as the incident angle increases, the electron paths in the interior of the target are closer to the surface implying that electrons reflected with a direction toward the surface will have a larger probability to cross it prior to losing their energy in inelastic collisions [147].

We continue with the main results of this validation test, focusing on the comparison between single scattering and multiple scattering models. *First*, we shall inspect the normal incidence results in the keV range. It is apparent that G4EmStandardPhysicsSS provides the most satisfactory description of the EBS yield. Regardless of the atomic number, it manages to describe the keV energy η plateau in a very accurate fashion. Even more remarkably, it accurately reproduces the Bronshtein–Fraiman sub-keV dataset, which is considered to be the most reliable. This is particularly valid for Pt, Au, Cd and Ag. Moreover, the single scattering model coupled with the PENELOPE library leads to an extended η overshoot for all medium-Z and high-Z materials. Such overshoots also emerge in the EBS yields of other MC codes [163, 164]. Finally, the multiple scattering model coupled with the PENELOPE library yields an erroneous collapse of the EBS yield towards zero in the entire sub-keV range for medium-Z and high-Z materials. Nevertheless, also this simulation set results in a keV energy η plateau close to the experimental one.

Second, we shall inspect the normal incidence results in the MeV range. It is apparent that all three simulation sets reproduce the experimental results with a satisfactory accuracy. It is also encouraging that the monotonic decrease exhibited by the simulation results and the experimental data has a similar functional form. It appears that the single scattering model coupled with the PENELOPE library deviates slightly less from the experimental data. Overall, the single and multiple scattering models that are coupled with the PENELOPE library are indistinguishable within the level of the statistical MC fluctuations. This is a particularly promising result, since the single scattering implementation comes at a one to two orders magnitude higher computational cost.

Third, we shall inspect the oblique incidence results at different incident energies. Given the relatively large probed incident energies (20 keV, 40 keV and 60 keV), the three simulations sets yield very similar results. Overall, the agreement with the experimental data is very good; the deviations increase as the incident angle becomes more tangential, the incident energy decreases and the atomic number increases. For Be and C, the three simulation sets are practically indistinguishable from each other and from the experimental results. For all the medium-Z and high-Z materials, the experimental results lie between the results of the G4EmStandardPhysicsSS set and the results of the single scattering model coupled with PENELOPE library.

As expected, single scattering implementations always yield the most accurate results. More important, it can be firmly concluded that the deviations between the single and multiple scattering models increase as the atomic number increases and as the incident energy decreases. Finally, it can also be stated that multiple scattering models exhibit an acceptable level of accuracy as far as direct RE backscattering is concerned, which naturally implies a massive reduction of the computational cost. Note that this level of accuracy is compromised as far as the re-backscattering of promptly re-deposited backscattered REs is concerned. However, such an electron population would be negligible to begin with, given the very small values of the EBS yield in the MeV range.

5 | Application to controlled DIII-D exposure

With a reliable list of physical processes selected and the sensitivity with respect to the scattering implementation assessed, the procedure is to be applied to a real case scenario. Specifically, this chapter discusses the modeling of RE-induced damage inflicted on a graphite sample inserted in DIII-D with the Divertor Material Evaluation System (DiMES).

The workflow is described, starting from the empirical data in terms of sample geometry, magnetic field topology and RE beam characteristics, proceeding with the GEANT4 implementation of the experimental layout for volumetric energy deposition extraction, translating it to volumetric heat maps that are employed as input to MEMENTO simulations that yield temperature profiles as well as estimates of the vaporization loss.

While the results of the developed work flow cannot be directly compared with the experimental observations, they shed some light to the realized damage mechanism since the resulting temperature profiles are consistent with explosive material detachment and the vapor losses are negligible compared to the material loss through the release of solid debris. Moreover, the effect of the toroidal magnetic field on the energy deposition and the sample thermal response is also assessed by comparing simulations with and without the presence of the B-field.

5.1. Experimental input data

The DiMES manipulator allows the exposure of arbitrarily shaped samples in the lower divertor of DIII-D under well-diagnosed and repeatable plasma conditions. During shot #191366, a dome-shaped sample, composed of ATJ graphite (with $\rho = 1.76\,\mathrm{g/cm^3}$ density), was exposed. Its geometry is shown in Fig.5.1, namely a dome of a curvature radius of 3.3 cm coming out the divertor shelf floor by 1 cm that is equipped with a thermocouple sensor mounted 1.5 cm below the floor level.

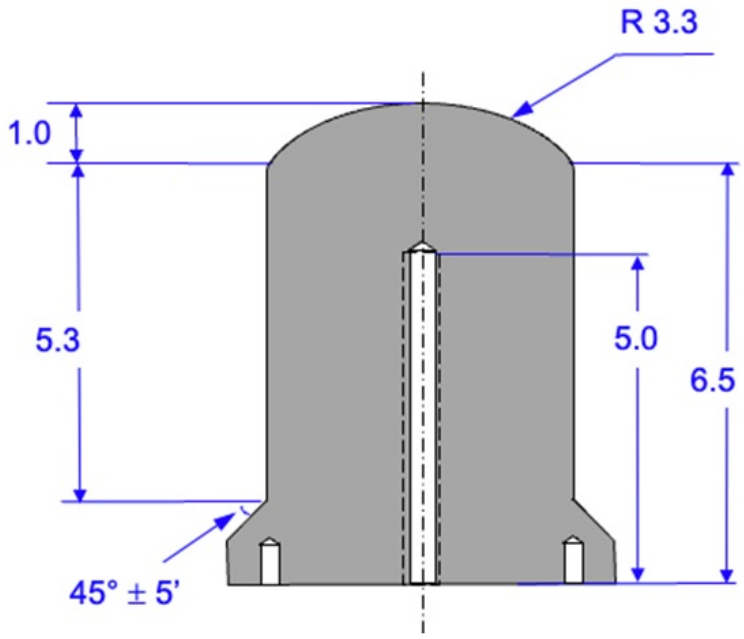

Figure 5.1: Domed graphite DiMES sample exposed to DIII-D plasma. Dimensions are reported in cm. Images courtesy of C. Lasnier and I. Bykov.

The RE beam is formed with Ar pellet injection and is drifted down into the plasma floor, where it is radially dumped on the sample. The RE beam termination is analyzed with a series of diagnostics, which provide information on the time evolution and intensity of the event. The plasma current, hard X-ray emission and radiated power signals are shown in the graphs of Fig.5.2: the correlation between the I_p drop and the surge of activity in HXR and P_rad is obvious, starting at $t = 1764\,\mathrm{ms}$ and exhausted in about 1-1.5 ms. The expected RE energy distribution is nearly mono-energetic of 1 MeV at the impact zone. It is estimated that the beam has deposited a total amount of energy around 10 kJ inside the sample [165]. Moreover, the magnetic field is given by a mostly toroidal contribution of $B = 2.4\mathrm{T}$, in a direction opposite to the plasma current. Its spatial orientation, together with the expected RE impact angles as inferred from the post-mortem analysis of the

sample, are reported in Fig.5.3.

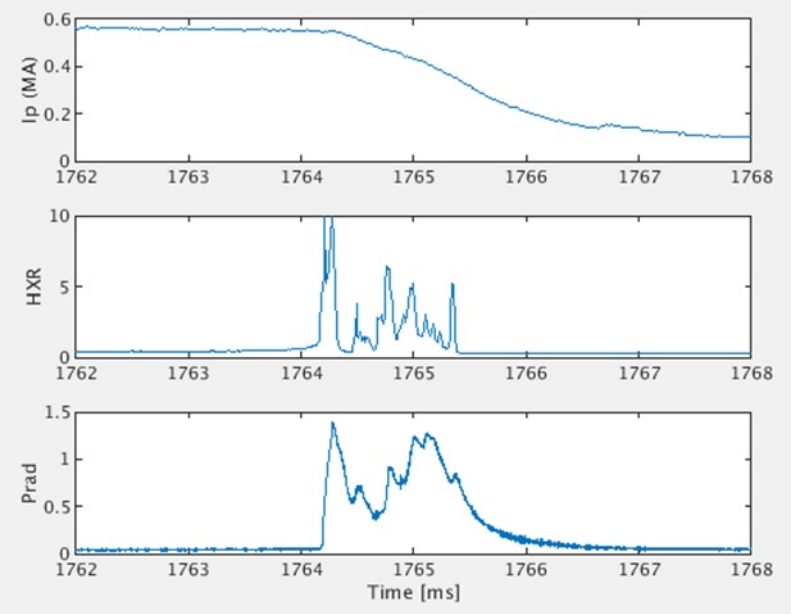

Figure 5.2: RE impact timing on DiMES: plasma current, HXR signal and radiated power signal. Images courtesy of C. Lasnier and I. Bykov.

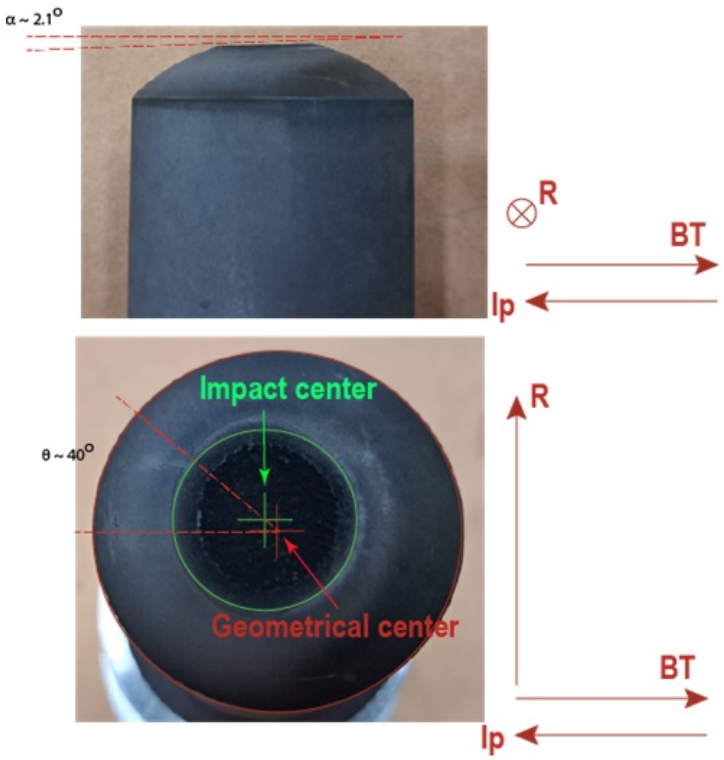

Figure 5.3: Impact angle on the DiMES dome and the B-field orientation. Images courtesy of C. Lasnier and I. Bykov.

Aiming to account for cross-field transport effects, it is assumed that the RE flux decays exponentially along the vertical direction (z-axis), following an estimated distribution given by

$$\Phi_{REs} \sim \exp\left\{-\left[\frac{(z-h)}{\lambda_q}\right]^2\right\} \tag{5.1}$$

where $h = 1$ cm represents the exposed height of the dome, while $\alpha = 0.2$ is the grazing impact angle and $\lambda_q = 2h\alpha$ is a decay length [165]. The spatial dependence of Eq.5.1 is presented in Fig.5.4.

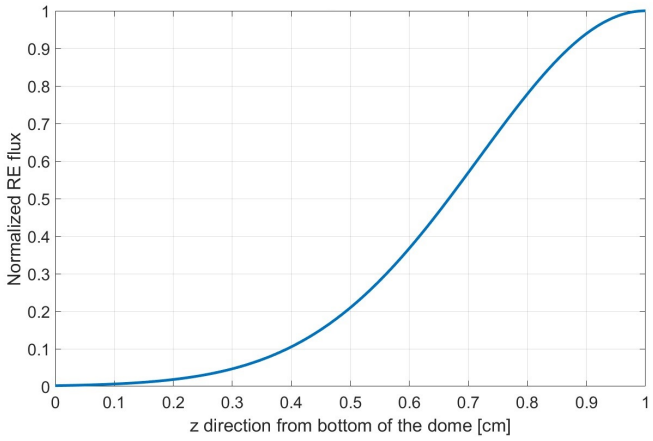

Figure 5.4: Spatial variation of RE flux along the z-axis; $z = 0$ represents the bottom of the graphite dome, $z = 1\,\text{cm}$ the top.

As discerned from Fig.5.3, a considerable amount of material is lost during the exposure. This took place in the course of an explosion-type event accompanied by the release of high-velocity solid debris, as observed by the IR camera. The IR data suggest that these debris are predominantly moving away from the lower divertor, as depicted in Fig.5.5, with speeds of the order of 100 - 200 m/s.

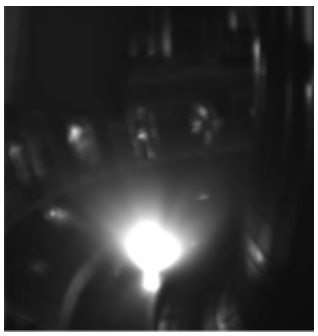

Figure 5.5: IR camera snapshot documenting material detachment from the DiMES sample. Images courtesy of C. Lasnier and I. Bykov.

The next step is to implement this empirical input (geometry, energy distribution, spatial flux distribution, impact angle) into a specialized GEANT4 set-up. The goal is to mimic as closely as possible the experimental layout in order to achieve a realistic modeling of the RE-induced damage, to be finally compared with the post-mortem analysis of the exposed sample.

5.2. GEANT4 implementation

The first step concerns the definition of the sensible volume, *i.e.* the construction of the geometry class. A precise reconstruction is possible thanks to the variety of tools provided by the GEANT4. The density of carbon (graphite) has been manually set to that corresponding to the nominal value of the sample nuclear grade.

The second step concerns the particle source class which has to be designed to mimic the experimental RE flux and the wetting geometry. To reproduce the exponential decay distribution in space, the particle source assumes the shape of a vertical rectangular plane divided into 20 horizontal stripes. From each of these stripes, a number of electrons N is released, that respects the guidelines discussed in chapter 3 for negligible statistical noise and simultaneously satisfies the exponential decay. Fig.5.6 shows both the sample geometry and the stripe subdivision, including the impact on the sample, while the spatial distribution of N stripe by stripe is shown in the histogram presented in Fig.5.7. As aforementioned, the experimental results suggest that the total energy received by the sample is about 10 kJ. To match this energy the total number of electrons is multiplied by a factor of around 10^{10}.

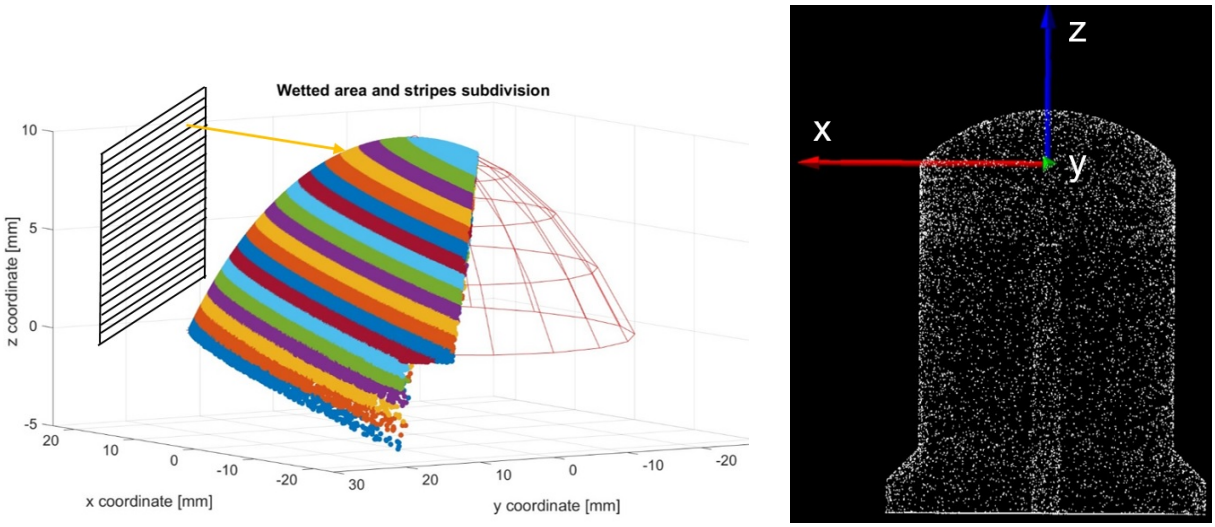

Figure 5.6: Left panel: the particle source with its stripe subdivision (in black) and the respective wetting stripes on the sample (in color). Right panel: the simulation frame of reference and the sample geometry visualized through the OGL software in GEANT4.

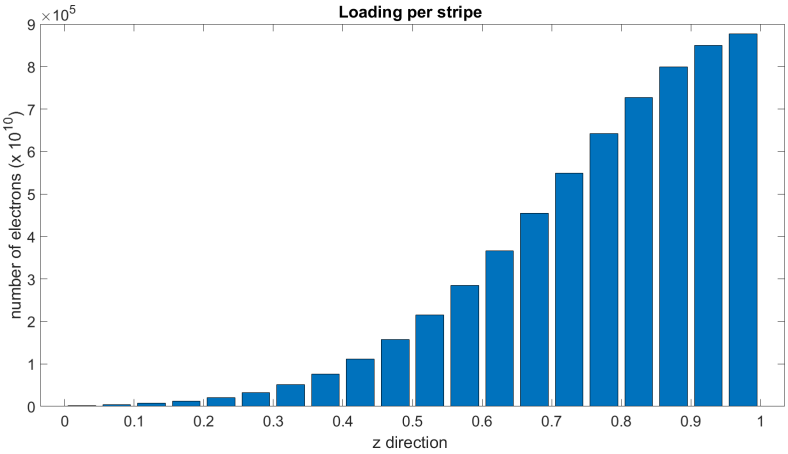

Figure 5.7: Discretization of the spatial distribution in terms of electron number. Each bin is released from each of stripes shown in Fig.5.6.

The third step concerns the implementation of the magnetic field. According to the experimental input, the RE direction can be described by means of two angles [165]: an inclination of $\alpha = 11.46°$ with respect to the yz plane and an angle of $\theta = 40.1°$ in the xy plane, as illustrated in Fig.5.8. In the experiment, the magnetic field of $B = 2.4\,\mathrm{T}$ is oriented along the y-axis, in the opposite direction to the incoming RE flux. Its effect on the electron trajectories outside the DiMES sample is already accounted for by the empirical impact angles. Thus, here, in the simulations when $\vec{B}$ field is included, it is implemented only within the graphite sample. Clearly, this is not fully self-consistent, as for example such implementation excludes the possibility that backscattered electrons return into the sample in the course of their Larmor gyration. Nevertheless, the assumption is justified from the point of view of energy deposition, since the backscattering yield at normal incidence for bulk graphite at 1 MeV is merely of the order of 0.01.

Given the results of the previous section, the PENELOPE physics model together with the Urban multiple scattering implementation suffice to provide accurate results for the energy deposition of 1MeV REs on graphite. The energy deposited by the RE impact on the spherical surface of the sample is plotted in Fig.5.9, revealing a non-uniform profile. This can be attributed to a combination of effects such as the exponential decay along the z-axis, the inclination of the impinging REs and the curved surface of the dome. Moreover, to reach a total energy deposited of 10 kJ it has been necessary to load 12.41 kJ. Such energy losses (12.5%) stem from particles that leave the sensible volume without depositing their whole kinetic energy due to electron backscattering, electron transmission and Bremsstrahlung leakage.

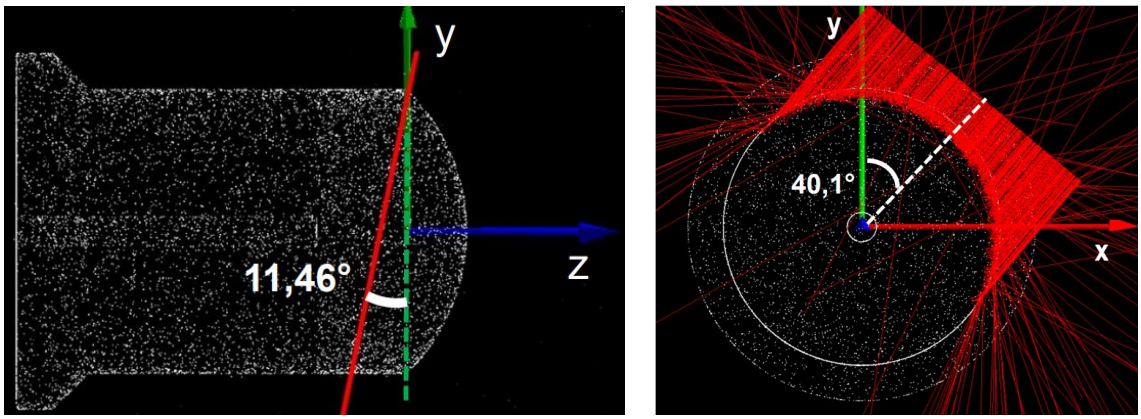

Figure 5.8: OGL representation of the direction of impact of REs in the yz plane (left) and the xy plane (right). The red trajectories represent primary electrons. Physical processes are disabled in the figure on the left for the sake of clarity.

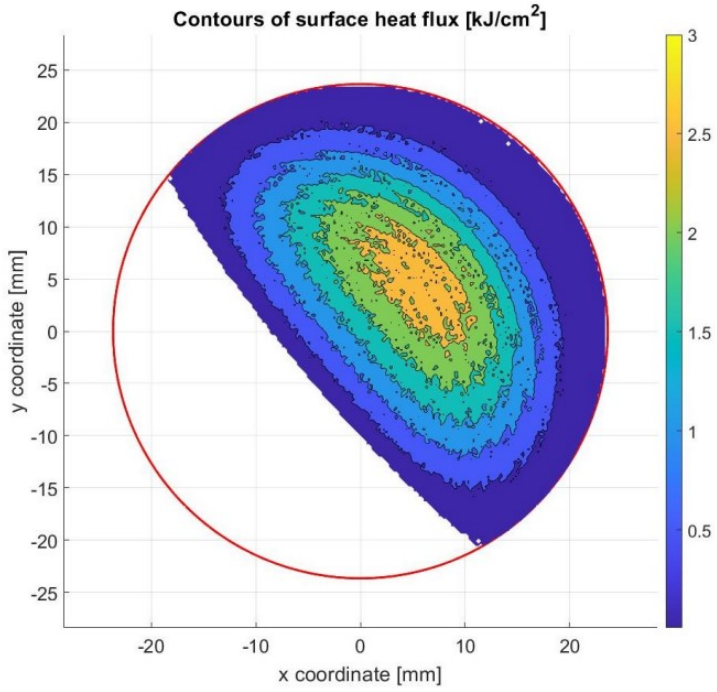

Figure 5.9: Contour plots of energy deposition on the DIII-D graphite sample.

5.3. Volumetric heat map

The main output of the GEANT4 simulations concerns the three-dimensional heat maps, expressed in [J/cm^3]. Two cases are presented: one with $B = 0$ and the other assuming the presence of magnetic field only inside the sensible volume. Results are shown in Fig. 5.10, reporting the cross section planes at $x = 0$. Note that, in order to provide a detailed view of the heat maps, only the cells with energy deposited larger than one order of magnitude below the maximum have been included.

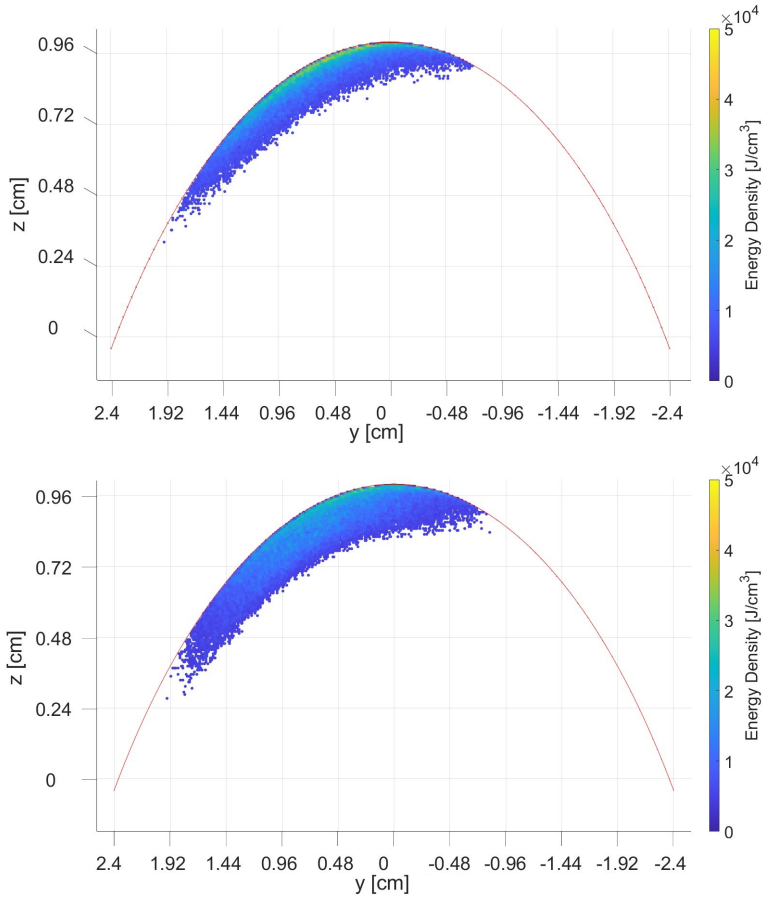

Figure 5.10: Results of GEANT4 simulations: $x = 0$ cross section of the volumetric heat map. Top panel: no magnetic field. Bottom panel: toroidal magnetic field only inside the sample. The same color bar is employed in both figures to facilitate the comparison.

The main difference lies in the energy spatial distribution. Without the magnetic field, the energy map is more concentrated in the first layers underneath the surface, with a high peak value represented by the bright yellow color in the upper panel of Fig.5.10. When the B-field is present inside the sample (lower panel), one can observe a much more spread energy distribution, more uniform and peaking at a lower magnitude. Moreover,

in spite of the identical loading (12.41 kJ), the total amount of energy deposited in this case increases by 11.4%, as reported in Table 5.1,

	No $\vec{B}$ field	**$\vec{B}$ field inside the sample**
Total energy deposited	10 kJ	11.4 kJ

Table 5.1: Total energy deposited with and without magnetic field, for identical loading.

In order to gain some insights on the effect of the $\vec{B}$ field on the volumetric heat map, it is instructive to plot some trajectories of primary electrons inside the graphite sample. Such graphs are presented in Fig.5.11 for the case with (right) and without (left) magnetic field. It is evident that, in the latter case, the trajectories are bent due to a counter-clock gyration. Thus, the electrons are less likely to leave the volume, and gyrate inside the sample with a radius depending on their velocity component perpendicular to the field direction. This leads to an increased energy deposition, as well as to a more uniform and spread spatial distribution.

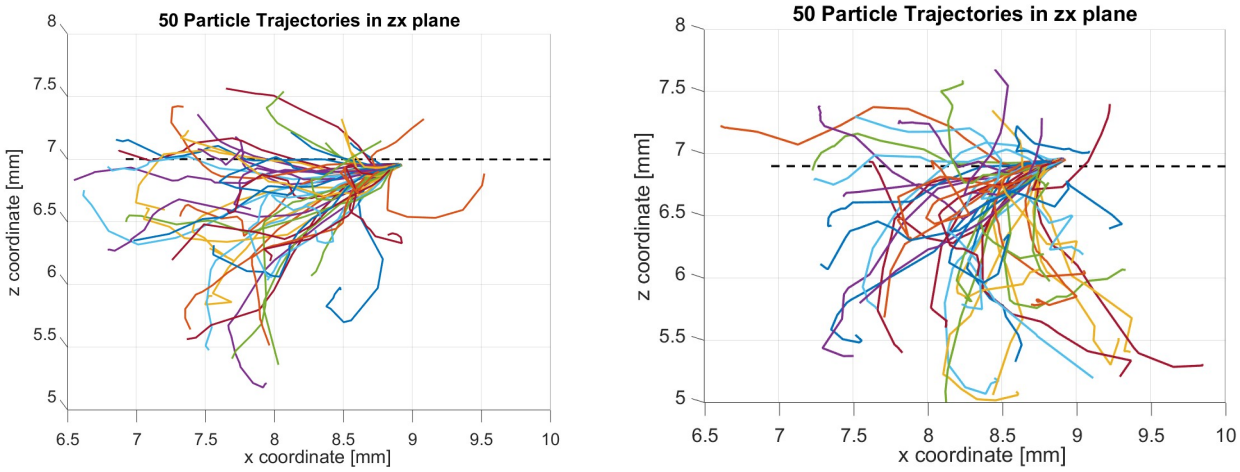

Figure 5.11: 2-D plot of 50 primary electron trajectories in the zx plane. Two cases are shown, with (right panel) and without (left panel) magnetic field. Dashed lines indicate the circumference of the dome surface where electrons impinge in this example.

5.4. MEMENTO results

5.4.1. MEMENTO code

The obtained volumetric heat maps alone are not sufficient to provide an insight on the thermo-mechanical response of the material. Thus, it is necessary to employ another numerical tool capable to simulate such response with the GEANT4 produced volumetric maps as an input. In this thesis, the MEMENTO code has been used for simulations of the thermal response.

MEMENTO (**ME**tallic **M**elt **E**volution in **N**ext-step **TO**kamaks) [166, 167] is a code that is developed and maintained at the KTH Space Plasma Physics Division for the assessment of melt damage of plasma facing components in fusion machines. It is an implementation of the MEMOS-U physics model [37, 40, 168, 169] which describes PFC thermal response and macroscopic melt motion and has been thoroughly validated against numerous dedicated EUROfusion experiments [167, 170–175]. The model is derived from the thermolectric magnetohydrodynamic equations coupled with heat diffusion and phase transitions. Taking advantage of the typical fusion-relevant melt pool dimensions, the fluid equations are formulated within the shallow water approximation resulting in a drastic reduction of the computational cost. The electromagnetic field equations are formulated in the magnetostatic limit and for uniform material composition.

5.4.2. Implementation in MEMENTO

For the MEMENTO simulations, the spherical cap geometry has been mapped onto a rectilinear grid. Additionally, the volumetric energy deposition, obtained by the GEANT4 simulations, is translated to a power flux and passed as input to MEMENTO. For its translation to power, the energy is spread out over a certain time period. Two different possibilities were investigated; one was to deposit the energy in one time-step while the other was to spread out the energy over 1 ms, which is the duration of the RE termination event, as reported in section 5.1. Preliminary runs indicated that the results are rather close, thus here only the second option is presented in detail.

Since graphite does not melt at low pressures, the MEMENTO physics model can be reduced. In particular, the momentum equation and current propagation equation do not need to be solved. Thus, the model reduces to the heat diffusion coupled with the column height equation, which describes the conservation of mass as the sample is eroded due to

vaporization. The resulting two equations are

$$\frac{\partial b_2}{\partial t} = -\dot{x}_{\mathrm{vap}}, \tag{5.2}$$

$$c_{\mathrm{p}}\rho_{\mathrm{m}}\frac{\partial T}{\partial t} = \nabla\cdot(k\nabla T) + V, \tag{5.3}$$

with the boundary condition

$$-k\frac{\partial T(\boldsymbol{r})}{\partial n} = \begin{cases} q_{\mathrm{vap}} + q_{\mathrm{rad}}, \text{ on } b_2 \\ 0, \text{ otherwise} \end{cases} \tag{5.4}$$

Here b_2 is the top surface of the sample, $\dot{x}_{\mathrm{vap}}$ is the rate of erosion due to vaporization, c_{p} the heat capacity, ρ_{m} the mass density, k the thermal conductivity while q_{vap} and q_{rad} refer to the cooling fluxes due to vaporization and thermal radiation.

5.4.3. Temperature profiles and vaporization loss

Two-dimensional temperature profiles, corresponding to the loading shown in Fig.5.10, are presented in Fig.5.12, for the cases without (upper) and without (lower) magnetic field.

Naturally, the temperature profiles reflect the volumetric heat source. The plots employ the same color-bar to facilitate comparison, however it is worth noting that the color-bar is saturated in the upper panel (no $\vec{B}$ field case), where temperatures far above 9000K are reached. As evident from the lower panel, the magnetic field results in a lower peak temperature value beneath the surface, and a more extended elevated temperature region, up to several millimeters in depth. For further comparison, a 1-D temperature profile along the white dashed line, is presented in Fig.5.13.

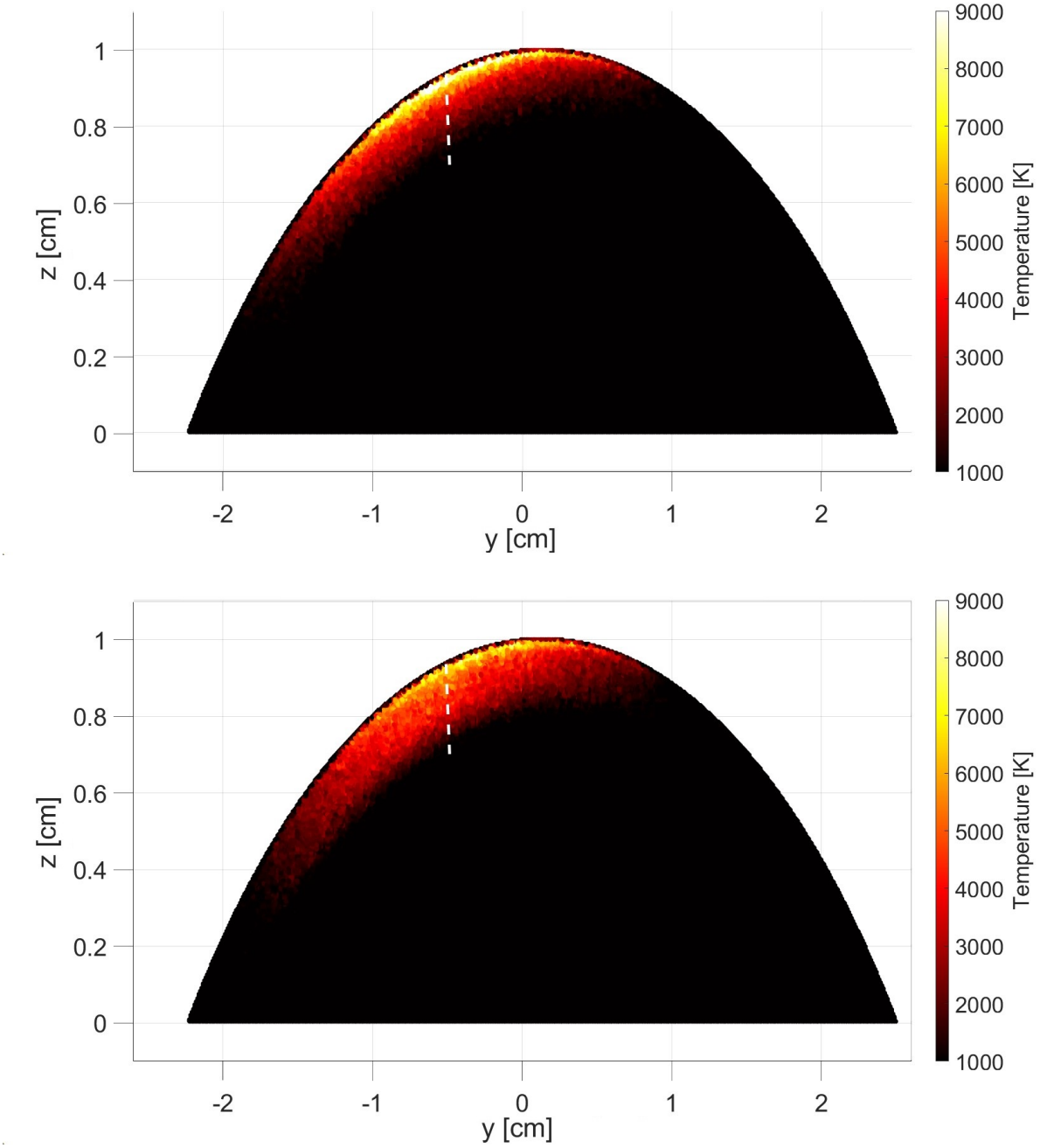

Figure 5.12: MEMENTO simulation results: 2-D temperature profiles at the x=0 plane. The cases with (lower panel) and without (upper panel) magnetic field are presented.

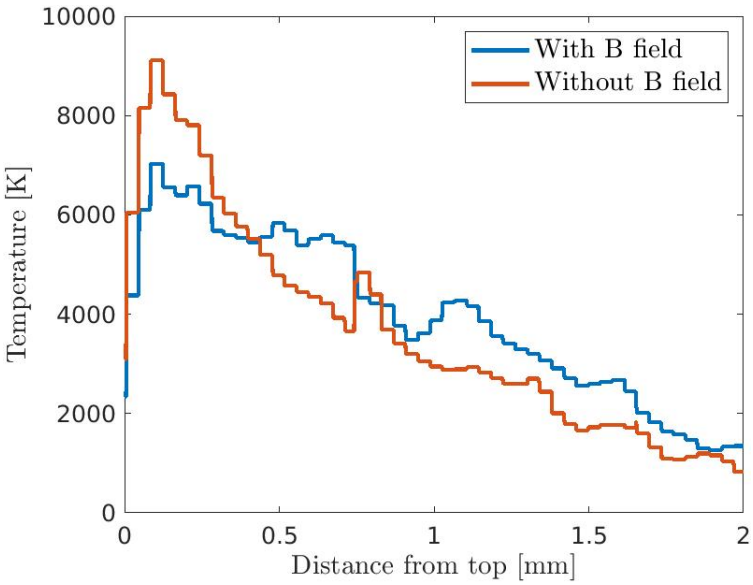

Figure 5.13: 1-D temperature profiles with and without magnetic field. The x-axis corresponds to the vertical white dashed line in Fig.5.12.

Other than the effect of the magnetic field, the temperature profiles shed light on the mechanism responsible for the material loss during the sample exposure. In both cases, with and without $\vec{B}$ field, the surface temperature is quite modest $\sim$ 3000K, about 900K below graphite's sublimation point. The vapor pressure of graphite at 3000 K is $\sim$ 60 Pa resulting in a negligible erosion rate. The top surface of the spherical cap at the beginning and the end of the MEMENTO simulation is shown in Fig.5.14 with the two surfaces almost overlapping as the predicted erosion depth is ~ 1 μm. In contrast, in the experiment, as can be discerned from Figs.5.15 and 5.16, the depth of the deformation reaches about 1 mm. A mechanism other than vaporization has to lead to such significant material loss. Indeed, the simulated temperature profiles are non-monotonic and peak inside the sample with the strong gradients confined within the detached volume, see Fig.5.16. Such profiles lead to stress build-up (due to the uneven thermal expansion possibly combined with the large stresses due to internal boiling) [176] and eventual explosion-like release of the material, as seen in the IR camera observations of the flying debris discussed in section 5.1.

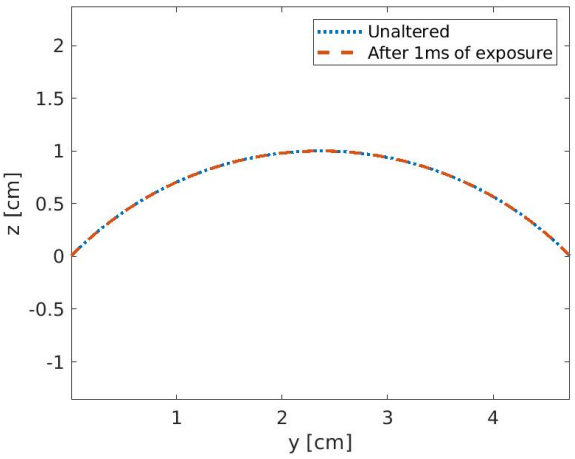

Figure 5.14: Comparison of the sample free surface as modelled in MEMENTO at the beginning of the simulation and after 1 ms of RE impact.

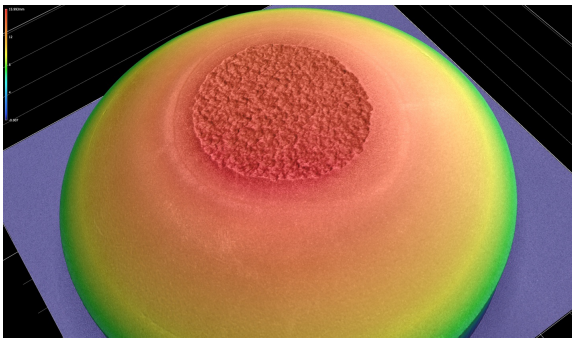

Figure 5.15: Confocal imaging of the sample after the exposure. Image courtesy of C. Lasnier and I. Bykov

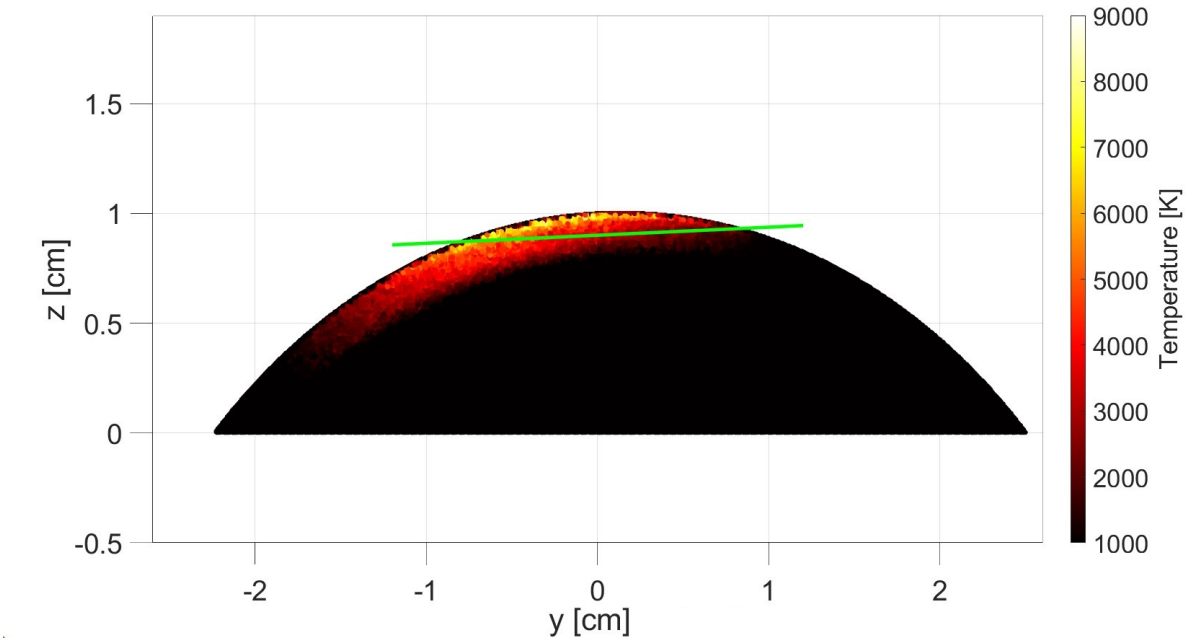

Figure 5.16: MEMENTO simulation result with magnetic field: 2-D temperature profile at the x=0 plane. The green line delimits the material losses as estimated from the post-mortem analysis shown in Fig.5.3

6 | Conclusions

Runaway electrons pose a serious threat for the safety of fusion devices. In the course of RE termination, intense heat fluxes are incident on PFCs which can cause extensive damage, as documented in numerous tokamaks. Characteristic examples concern the localized stationary melting of the Be dump plates in JET and the thermal shock-induced explosion of the poloidal TZM limiters in FTU. This has motivated an intense research on the understanding of runaway electron formation, control and mitigation, particularly in the context of the ITER project. Despite the remarkable progress concerning RE avoidance, suppression and benign termination, RE-induced damage remains an important issue, especially in future fusion reactors. As a consequence, the reliable predictive modelling of the PFC damage triggered by REs is rather imperative.

This thesis project focuses on predictions of the volumetric energy deposition caused by the incidence of intense relativistic RE beams and on estimates of the associated thermal PFC response. The goal is to validate the most relevant physics models and numerical tools available against experimental evidence. The workflow combining these tools can then be employed for predictive studies of RE-induced PFC damage in future reactors. More specifically; the GEANT4 Monte Carlo code has been selected to simulate RE transport inside condensed matter, including all aspects of the accompanying electromagnetic shower, yielding three-dimensional heat maps; the MEMENTO macroscopic melt motion code has been employed to model the PFC thermal response to the volumetric RE heat load. The combination of these two tools is tested against experimental evidence from controlled exposures carried out in the DIII-D tokamak.

The use of GEANT4 requires a meticulous validation activity due to the abundance of available physics models which might be characterized by inaccuracies and implementation bugs. The benchmarking work was subdivided into two sections: one dedicated to calorimetry measurements of the energy deposition and one dedicated to charge collection measurements of the electron backscattering yield for different materials, incident energies and angles of incidence. The accuracy of user-selected libraries and pre-compiled libraries available in GEANT4 has been tested. Particular attention has been given to the

efficiency of multiple, mixed and single scattering models, given the trade-off between accuracy and computational cost. It is demonstrated that GEANT4 offers a vast flexibility to adapt with high accuracy to different experimental scenarios.

To gain confidence in applications to real case scenarios, the GEANT4-MEMENTO workflow has been employed for the modelling of the RE-induced damage inflicted on a graphite sample exposed inside the DIII-D tokamak. Experimental input data (PFC geometry, magnetic field topology, RE energy distribution, RE wetting specifics) have been successfully implemented in GEANT4. The GEANT4 volumetric heat loads have been used as an input for MEMENTO heat transfer simulations to assess the temperature distribution inside the sample. A non-monotonic temperature profile emerges, reflecting the spatial dependence of the volumetric energy deposition, that is characterized by a modest surface temperature and by a strong peak beneath the surface. The first result allows us to exclude vaporization as the mechanism responsible for the sample erosion, whereas the second result is consistent with the explosive material detachment revealed in the post-mortem analysis. Particular attention is given to the effect of the magnetic field, which alters the charged particle trajectories modifying the energy distribution and even the total amount of energy absorbed. In particular, the magnetic field reduces the peak temperature and extends the temperature gradient.

In order to complete the development of the GEANT4 simulations, the inclusion of neutron production via electro-neutron (first generation) or photo-neutron (second generation) paths is envisaged together with all physics processes associated with neutron transport. In order to optimize the development of the GEANT4 simulations, further benchmarking activities are planned against integrated quantities which concern the electron backscattering yield from thin (semi-transparent) targets, the electron transmission yield from thin targets, the Bremsstrahlung efficiency from thick/thin targets and the photoneutron yield from thick/thin targets. In the prospect of GEANT4 comparison with embedded or external electromagnetic shower diagnostics, more demanding validation tests are also viable against energy or angular distributions of backscattered or transmitted electrons, emitted Bremsstrahlung photons and ejected neutrons.

As far as the comparison with the DIII-D experiment is concerned, new simulations are required aiming at a more self consistent approach. Specifically, the magnetic field will also be included outside the exposed sample (to fully account for gyration effects) and the results of KORC simulations will be utilized to mimic the wetting specifics more closely (spatial profile and momentum distribution).

Bibliography

[1] S. Yican Wu, Fusion Energy Production, Comprehensive Energy Systems, 2018.

[2] R. V. Petrescu, R. Aversa, S. Kozaitis, A. Apicella, F. I. Petrescu, Some basic reactions in nuclear fusion, American Journal of Engineering and Applied Sciences Volume 10, Issue 3 ((November 19, 2017)).

[3] J. D. Lawson, Some criteria for a useful thermonuclear reactor, Atomic Energy Research Establishment (December 1955).

[4] J. D. Lawson, Some criteria for a power producing thermonuclear reactor, Proceedings of the Physical Society. Section B 70 (1) (1957) 6.

[5] S. E. Wurzel, S. C. Hsu, Progress toward fusion energy breakeven and gain as measured against the Lawson criterion, Physics of Plasmas 29 (6) (2022) 062103.

[6] J. Lyman Spitzer, The stellarator concept, Physics of Fluids 1, 253–264 (1958).

[7] A. H. Boozer, Stellarator design, Journal of Plasma Physics 81 (6) (2015) 515810606.

[8] M. Yamada, M. Ellis, R. Furth, Experimental investigation of the spheromak configuration, Plasma physics and controlled nuclear fusion research (1983).

[9] R. Post, The magnetic mirror approach to fusion, Nuclear Fusion 27 (10) (1987) 1579.

[10] M. Kikuchi, K. Lackner, T. M. Quang, Fusion physics (2012).

[11] P. Haubenreich, M. Lubell, D. Cornish, D. Beard, Superconducting magnets for fusion, Nuclear Fusion 22 (9) (1982) 1209.

[12] P. Bruzzone, W. H. Fietz, J. V. Minervini, M. Novikov, N. Yanagi, Y. Zhai, J. Zheng, High temperature superconductors for fusion magnets, Nuclear Fusion 58 (10) (2018) 103001.

[13] T. Boinnard, A. Coelho, J. Loizu, P. Ricci, Plasma turbulence simulations in a diverted tokamak with applied resonant magnetic perturbations, Nuclear Fusion 63 (7) (2023) 076005.

[14] All the world's tokamaks. the tokamak information website. available from: http://www.tokamak.info.

[15] A. C. C. Sips, Advanced scenarios for iter operation (2004).

[16] ITER Physics Basis Editors , ITER Physics Expert Group Chairs and Co-Chairs , ITER Joint Central Team and Physics Integration Unit, , Chapter 1: Overview and summary, Nuclear Fusion 39 (12) (1999) 2137.

[17] A. Suri, N. Krishnamurthy, I. Batra, Materials issues in fusion reactors, Journal of Physics: Conference Series 208 (2010) 012001.

[18] G. Federici, C. Skinner, J. Brooks, J. Coad, C. Grisolia, A. Haasz, A. Hassanein, V. Philipps, C. Pitcher, J. Roth, W. Wampler, D. Whyte, Plasma-material interactions in current tokamaks and their implications for next step fusion reactors, Nuclear Fusion 41 (12) (2001) 1967.

[19] T. Loarer, Fuel retention in tokamaks, Journal of Nuclear Materials 390-391 (2009) 20–28, proceedings of the 18th International Conference on Plasma-Surface Interactions in Controlled Fusion Device.

[20] C. H. Skinner, W. Blanchard, J. Kamperschroer, P. LaMarche, D. Mueller, A. Nagy, S. Scott, G. Ascione, E. Amarescu, R. Camp, M. Casey, J. Collins, M. Cropper, C. Gentile, M. Gibson, J. Hosea, M. Kalish, J. Langford, S. Langish, R. Mika, D. K. Owens, G. Pearson, S. Raftopoulos, R. Raucci, T. Stevenson, A. Von Halle, D. Voorhees, T. Walters, J. Winston, Measurements of tritium retention and removal on the Tokamak Fusion Test Reactor, Journal of Vacuum Science Technology A 14 (6) (1996) 3267–3274.

[21] T. Loarer, C. Brosset, J. Bucalossi, P. Coad, G. Esser, J. Hogan, J. Likonen, M. Mayer, P. Morgan, V. Philipps, V. Rohde, J. Roth, M. Rubel, E. Tsitrone, A. Widdowson, J. E. contributors, Gas balance and fuel retention in fusion devices, Nuclear Fusion 47 (9) (2007) 1112.

[22] G. Federici, R. Doerner, P. Lorenzetto, V. Barabash, Beryllium as a plasma-facing material for near-term fusion devices, Comprehensive Nuclear Materials (2012) 621–666.

[23] P. Tolias, Analytical expressions for thermophysical properties of solid and liquid beryllium relevant for fusion applications, Nuclear Materials and Energy 31 (2022) 101195.

[24] G. Pinchuk, Tungsten as a plasma-facing material, Comprehensive Nuclear Materials (2012) 551–581.

[25] P. Tolias, Analytical expressions for thermophysical properties of solid and liquid tungsten relevant for fusion applications, Nuclear Materials and Energy 13 (2017) 42–57.

[26] A. Herrmann, I. Zammuto, M. Balden, H. Greuner, N. Jaksic, A. Kallenbach, M. Li, R. Neu, V. Rohde, A. U. Team, et al., Experiences with a solid tungsten divertor in asdex upgrade, Nuclear Materials and Energy 12 (2017) 205–209.

[27] R. A. Pitts, S. Bardin, B. Bazylev, M. A. van den Berg, P. Bunting, S. Carpentier-Chouchana, J. W. Coenen, Y. Corre, R. Dejarnac, F. Escourbiac, J. Gaspar, J. P. Gunn, T. Hirai, S.-H. Hong, J. Horacek, D. Iglesias, M. Komm, K. Krieger, C. Lasnier, G. F. Matthews, T. W. Morgan, S. Panayotis, S. Pestchanyi, A. Podolnik, R. E. Nygren, D. L. Rudakov, G. De Temmerman, P. Vondracek, J. G. Watkins, Physics conclusions in support of ITER W divertor monoblock shaping, Nuclear Materials and Energy 12 (2017) 60.

[28] R. A. Pitts, X. Bonnin, F. Escourbiac, H. Frerichs, J. P. Gunn, T. Hirai, A. S. Kukushkin, E. Kaveeva, M. A. Miller, D. Moulton, V. Rozhansky, I. Senichenkov, E. Sytova, O. Schmitz, P. C. Stangeby, G. De Temmerman, I. Veselova, S. Wiesen, Physics basis for the first ITER tungsten divertor, Nuclear Materials and Energy 20 (2019) 100696.

[29] J. Linke, J. Du, T. Loewenhoff, G. Pintsuk, B. Spilker, I. Steudel, M. Wirtz, Challenges for plasma-facing components in nuclear fusion, Matter and Radiation at Extremes 4 (5) (2019) 056201.

[30] C. Linsmeier, M. Rieth, J. Aktaa, T. Chikada, et al., Development of advanced high heat flux and plasma-facing materials, Nuclear Fusion 57 (2017) 092007.

[31] S. Ratynskaia, A. Bortolon, S. I. Krasheninnikov, Dust and powder in fusion plasmas: recent developments in theory, modeling, and experiments, Reviews of Modern Plasma Physics 6 (1) (8 2022).

[32] J. P. Gunn, S. Carpentier-Chouchana, F. Escourbiac, T. Hirai, S. Panayotis, R. A. Pitts, Y. Corre, R. Dejarnac, M. Firdaouss, M. Kocan, M. Komm, A. Kukushkin, P. Languille, M. Missirlian, W. Zhao, G. Zhong, Surface heat loads on the ITER divertor vertical targets, Nucl. Fusion 57 (2017) 046025.

[33] H. Zohm, Edge localized modes (elms), Plasma Physics and Controlled Fusion 38 (2) (1996) 105.

[34] T. Evans, Elm mitigation techniques, Journal of Nuclear Materials 438 (2013) S11–S18.

[35] L. Vignitchouk, S. Ratynskaia, P. Tolias, R. A. Pitts, G. De Temmerman, M. Lehnen, D. Kiramov, Survival and in-vessel redistribution of beryllium droplets after ITER disruptions, Nucl. Fusion 58 (2018) 076008.

[36] L. Vignitchouk, K. Paschalidis, S. Ratynskaia, P. Tolias, R. A. Pitts, Remobilized dust dynamics and inventory evolution in ITER-like start-up plasmas, Plasma Phys. Control. Fusion (2022) submitted.

[37] S. Ratynskaia, E. Thorén, P. Tolias, R. A. Pitts, K. Krieger, L. Vignitchouk, D. Iglesias, The ASDEX-Upgrade team, The JET Contributors, the EUROfusion MST1 Team, Resolidification-controlled melt dynamics under fast transient tokamak plasma loads, Nucl. Fusion 60 (2020) 104001.

[38] L. Vignitchouk, S. Ratynskaia, R. A. Pitts, M. Lehnen, Simulations of liquid metal flows over plasma-facing component edges and application to beryllium melt events in JET, Nucl. Fusion 62 (2022) 036016.

[39] L. Vignitchouk, S. Ratynskaia, Pitts, M. Lehnen, Beryllium melt instabilities and ejection during unmitigated current quenches in iter, Nucler Fusion 63 (2023) 016004.

[40] S. Ratynskaia, E. Thorén, P. Tolias, R. A. Pitts, K. Krieger, the ASDEX-Upgrade Team, , the EUROfusion MST1 Team, The memos-u macroscopic melt dynamics code—benchmarking and applications, Physica Scripta 96 (12) (2021) 124009.

[41] B. N. Breizman, P. Aleynikov, E. M. Hollmann, M. Lehnen, Physics of runaway electrons in tokamaks, Nuclear Fusion 59 (8) (2019) 083001.

[42] H. Dreicer, Electron and ion runaway in a fully ionized gas. i, Phys. Rev. 115 (1959) 238–249.

[43] Y. A. Sokolov, "multiplication" of accelerated electrons in a tokamak (2 1979).

[44] E. M. Hollmann, P. B. Parks, N. Commaux, N. W. Eidietis, R. A. Moyer, D. Shiraki, M. E. Austin, C. J. Lasnier, C. Paz-Soldan, D. L. Rudakov, Measurement

of runaway electron energy distribution function during high-Z gas injection into runaway electron plateaus in DIII-Da), Physics of Plasmas 22 (5) (2015) 056108.

[45] M. Rosenbluth, S. Putvinski, Theory for avalanche of runaway electrons in tokamaks, Nuclear fusion 37 (10) (1997) 1355.

[46] B. Esposito, L. Boncagni, P. Buratti, D. Carnevale, F. Causa, M. Gospodarczyk, J. Martin-Solis, Z. Popovic, M. Agostini, G. Apruzzese, W. Bin, C. Cianfarani, R. D. Angelis, G. Granucci, A. Grosso, G. Maddaluno, D. Marocco, V. Piergotti, A. Pensa, S. Podda, G. Pucella, G. Ramogida, G. Rocchi, M. Riva, A. Sibio, C. Sozzi, B. Tilia, O. Tudisco, M. Valisa, F. Team, Runaway electron generation and control, Plasma Physics and Controlled Fusion 59 (1) (2016) 014044.

[47] R. J. Zhou, Energy distribution of lost high-energy runaway electrons based on their bremsstrahlung emission in the east tokamak, Phys. Rev. E 107 (2023) 045204.

[48] S. M. Seltzer, M. J. Berger, Improved procedure for calculating the collision stopping power of elements and compounds for electrons and positrons, The International Journal of Applied Radiation and Isotopes 35 (7) (1984) 665–676.

[49] F. Maviglia, M. Siccinio, C. Bachmann, W. Biel, M. Cavedon, E. Fable, G. Federici, M. Firdaouss, J. Gerardin, V. Hauer, I. Ivanova-Stanik, F. Janky, R. Kembleton, F. Militello, F. Subba, S. Varoutis, C. Vorpahl, Impact of plasma-wall interaction and exhaust on the eu-demo design, Nuclear Materials and Energy 26 (2021) 100897.

[50] J. Coburn, E. Thoren, R. A. Pitts, H. Anand, M. Lehnen, L. Kos, M. Brank, S. Ratynskaia, P. Tolias, First wall energy deposition during vertical displacement events on iter, Physica Scripta 2020 (T171) (2020) 014076.

[51] E. Fortuna-Zaleśna, J. Grzonka, S. Moon, M. Rubel, P. Petersson, A. Widdowson, J. Contributors, Fine metal dust particles on the wall probes from jet-ilw, Physica Scripta 2017 (T170) (2017) 014038.

[52] I. Jepu, G. Matthews, A. Widdowson, M. Rubel, E. Fortuna-Zaleśna, J. Zdunek, P. Petersson, V. Thompson, P. Dinca, C. Porosnicu, P. Coad, K. Heinola, N. Catarino, O. Pompilian, C. P. Lungu, J. Contributors, Beryllium melting and erosion on the upper dump plates in jet during three iter-like wall campaigns, Nuclear Fusion 59 (8) (2019) 086009.

[53] G. F. Matthews, B. Bazylev, A. Baron-Wiechec, J. Coenen, K. Heinola, V. Kiptily, H. Maier, C. Reux, V. Riccardo, F. Rimini, G. Sergienko, V. Thompson, A. Wid-

dowson, J. Contributors7, Melt damage to the jet iter-like wall and divertor, Physica Scripta 2016 (T167) (2016) 014070.

[54] M. De Angeli, P. Tolias, S. Ratynskaia, D. Ripamonti, L. Vignitchouk, F. Causa, G. Daminelli, B. Esposito, E. Fortuna-Zalesna, F. Ghezzi, L. Laguardia, G. Maddaluno, G. Riva, W. Zielinski, Evidence for high-velocity solid dust generation induced by runaway electron impact in ftu, Nuclear Fusion 63 (1) (2022) 014001.

[55] L. Vignitchouk, P. Tolias, S. Ratynskaia, Dust-wall and dust-plasma interaction in the MIGRAINe code, Plasma Phys. Control. Fusion 56 (2014) 095005.

[56] P. Tolias, M. De Angeli, D. Ripamonti, S. Ratynskaia, G. Riva, G. Daminelli, M. De Angeli, Wall cratering upon high velocity normal dust impact, Fusion Engineering and Design 195 (2023) 113938.

[57] J. Mlynar, O. Ficker, E. Macusova, T. Markovic, et al., Runaway electron experiments at COMPASS in support of the EUROfusion ITER physics research, Plasma Physics and Controlled Fusion 61 (2019) 014010.

[58] V. P. Budaev, Y. V. Martynenko, S. A. Grashin, R. N. Giniyatulin, et al., Tungsten melting and erosion under plasma heat load in tokamak discharges with disruptions, Nuclear Materials and Energy 12 (2017) 418.

[59] M. Firdaouss, C. Desgranges, C. Hernandez, M. Richou, H. Greuner, B. Böswirth, I. Zacharie-Aubrun, T. Blay, J. Bucalossi, M. Missirlian, F. Samaille, E. Tsitrone, Overview of the different processes of tungsten coating implemented into west tokamak, Fusion Engineering and Design 124 (2017) 207–210, proceedings of the 29th Symposium on Fusion Technology (SOFT-29) Prague, Czech Republic, September 5-9, 2016.

[60] P. Moreau, S. Bremond, J. Bucalossi, C. Reux, D. Douai, T. Loarer, E. Nardon, R. Nouailletas, F. Saint-Laurent, P. Tamain, C. Bourdelle, N. Fedorczak, E. Tsitrone, J.-F. Artaud, t. Team, The commissioning of the west tokamak: Experience and lessons learned, IEEE Transactions on Plasma Science PP (2020) 1–6.

[61] M. Diez, Y. Corre, E. Delmas, N. Fedorczak, M. Firdaouss, A. Grosjean, J. Gunn, T. Loarer, M. Missirlian, M. Richou, E. Tsitrone, the WEST Team, In situ observation of tungsten plasma-facing components after the first phase of operation of the west tokamak, Nuclear Fusion 61 (10) (2021) 106011.

[62] C. Paz-Soldan, P. Aleynikov, E. Hollmann, A. Lvovskiy, I. Bykov, X. Du, N. Eidi-

etis, D. Shiraki, Runaway electron seed formation at reactor-relevant temperature, Nuclear Fusion 60 (5) (2020) 056020.

[63] X. Guan, H. Qin, N. J. Fisch, Phase-space dynamics of runaway electrons in tokamaks, Physics of Plasmas 17 (9) (2010).

[64] N. Commaux, L. R. Baylor, S. K. Combs, N. Eidietis, T. Evans, C. R. Foust, E. Hollmann, D. Humphreys, V. Izzo, A. James, et al., Novel rapid shutdown strategies for runaway electron suppression in diii-d, Nuclear Fusion 51 (10) (2011) 103001.

[65] D. Carnevale, M. Ariola, G. Artaserse, F. Bagnato, W. Bin, L. Boncagni, T. Bolzonella, F. Bombarda, P. Buratti, L. Calacci, et al., Runaway electron beam control, Plasma Physics and Controlled Fusion 61 (1) (2018) 014036.

[66] J. Connor, R. Hastie, Relativistic limitations on runaway electrons, Nuclear fusion 15 (3) (1975) 415.

[67] M. Lehnen, S. A. Bozhenkov, S. S. Abdullaev, M. W. Jakubowski, Suppression of runaway electrons by resonant magnetic perturbations in textor disruptions, Phys. Rev. Lett. 100 (2008) 255003.

[68] N. W. Eidietis, N. Commaux, E. M. Hollmann, D. A. Humphreys, T. C. Jernigan, R. A. Moyer, E. J. Strait, M. A. VanZeeland, J. C. Wesley, J. H. Yu, Control of post-disruption runaway electron beams in DIII-Da), Physics of Plasmas 19 (5) (2012) 056109.

[69] B. N. Breizman, P. Aleynikov, E. M. Hollmann, M. Lehnen, Physics of runaway electrons in tokamaks, Nuclear Fusion 59 (8) (2019) 083001.

[70] T. Kunugi, M. Akiba, M. Ogawa, O. Sato, M. Nakamura, The simulation of the energy deposition from runaway electrons in plasma facing components with egs4, Fusion Technology 21 (3P2B) (1992) 1868–1872.

[71] H.-W. Bartels, Impact of runaway electrons, Fusion engineering and design 23 (4) (1994) 323–328.

[72] G. Maddaluno, G. Maruccia, M. Merola, S. Rollet, Energy deposition and thermal effects of runaway electrons in iter-feat plasma facing components, Journal of Nuclear Materials 313-316 (2003) 651–656, plasma-Surface Interactions in Controlled Fusion Devices 15.

[73] V. Sizyuk, A. Hassanein, Self-consistent analysis of the effect of runaway electrons on plasma facing components in iter, Nuclear Fusion 49 (9) (2009) 095003.

[74] Y. Igitkhanov, B. Bazylev, I. Landman, Calculation of runaway electrons stopping power in iter, Journal of Nuclear Materials (2011).

[75] B. Bazylev, G. Arnoux, W. Fundamenski, Y. Igitkhanov, M. Lehnen, Modeling of runaway electron beams for jet and iter, Journal of Nuclear Materials 415 (1, Supplement) (2011) S841–S844, proceedings of the 19th International Conference on Plasma-Surface Interactions in Controlled Fusion.

[76] B. Bazylev, G. Arnoux, W. Fundamenski, Y. Igitkhanov, M. Lehnen, Modeling of runaway electron beams for jet and iter, Journal of Nuclear Materials 415 (1, Supplement) (2011) S841–S844, proceedings of the 19th International Conference on Plasma-Surface Interactions in Controlled Fusion.

[77] F. Salvat, Bethe stopping-power formula and its corrections, Phys. Rev. A 106 (2022) 032809.

[78] N. Beisert, Quantum Field Theory I, ETH Zurich.

[79] J. Baró, J. Sempau, J. Fernández-Varea, F. Salvat, Penelope: An algorithm for monte carlo simulation of the penetration and energy loss of electrons and positrons in matter, Nuclear Instruments and Methods in Physics Research Section B: Beam Interactions with Materials and Atoms 100 (1) (1995) 31–46.

[80] H. W. Koch, J. W. Motz, Bremsstrahlung cross-section formulas and related data, Rev. Mod. Phys. 31 (1959) 920–955.

[81] D. J. Griffiths, Introduction to quantum mechanics, Pearson Education, 1995.

[82] R. Pratt, H. Tseng, C. Lee, L. Kissel, C. MacCallum, M. Riley, Bremsstrahlung energy spectra from electrons of kinetic energy 1 kev t1 2000 kev incident on neutral atoms 2 z 92, Atomic Data and Nuclear Data Tables 20 (2) (1977) 175–209.

[83] S. M. Seltzer, M. J. Berger, Bremsstrahlung spectra from electron interactions with screened atomic nuclei and orbital electrons, Nuclear Instruments and Methods in Physics Research Section B: Beam Interactions with Materials and Atoms 12 (1) (1985) 95–134.

[84] S. M. Seltzer, M. J. Berger, Bremsstrahlung energy spectra from electrons with kinetic energy 1 kev–10 gev incident on screened nuclei and orbital electrons of neutral atoms with z = 1–100, Atomic Data and Nuclear Data Tables 35 (3) (1986) 345–418.

[85] E. Haug, Electron–electron and electron–positron bremsstrahlung, Radiation Physics and Chemistry 75 (10) (2006) 1330–1345, bremsstrahlung: Theory and Experiment.

[86] J. A. Wheeler, W. E. Lamb, Influence of atomic electrons on radiation and pair production, Phys. Rev. 55 (1939) 858–862.

[87] E. Rutherford, Lxxix. the scattering of and particles by matter and the structure of the atom, The London, Edinburgh, and Dublin Philosophical Magazine and Journal of Science 21 (125) (1911) 669–688.

[88] N. Mott, H. Massey, The theory of atomic collisions, Oxford University Press,London (1949).

[89] D. R. Yennie, The rosenbluth formula (6 1963).

[90] F. Salvat, A. Jablonski, C. J. Powell, elsepa—dirac partial-wave calculation of elastic scattering of electrons and positrons by atoms, positive ions and molecules (new version announcement), Computer Physics Communications 261 (2021) 107704.

[91] C. Fabjan, D. Fournier, Calorimetry, 2020, pp. 201–280.

[92] S. Mişicu, Giant dipole multi-resonances excited by high-frequency laser pulses, Particles 5 (3) (2022) 287–297.
URL `https://www.mdpi.com/2571-712X/5/3/25`

[93] M. Harakeh, A. Woude, Giant Resonances: Fundamental High-frequency Modes of Nuclear Excitation, Oxford science publications, Oxford University Press, 2001.
URL `https://books.google.fr/books?id=ux0JhIdbGT8C`

[94] O. Klein, Y. Nishina, Über die streuung von strahlung durch freie elektronen nach der neuen relativistischen quantendynamik von dirac, Z. Physik 52 (1929).

[95] R. Ribberfors, K. F. Berggren, Incoherent-x-ray-scattering functions and cross sections $(\frac{d\sigma}{d\Omega'})_{\text{incoh}}$ by means of a pocket calculator, Phys. Rev. A 26 (1982) 3325–3333.

[96] C.-K. Qiao, H.-C. Chi, L. Zhang, P. Gu, C.-P. Liu, C.-J. Tang, S.-T. Lin, K.-N. Huang, Relativistic impulse approximation in compton scattering, Journal of Physics B: Atomic, Molecular and Optical Physics 53 (7) (2020) 075002.

[97] L. Kissel, R. H. Pratt, S. C. Roy, Rayleigh scattering by neutral atoms, 100 ev to 10 mev, Phys. Rev. A 22 (1980) 1970–2004.

[98] Z. Berant, R. Moreh, S. Kahane, Nuclear thomson scattering of 5.5–7.2 mev photons, Physics Letters B 69 (3) (1977) 281–283.

[99] M. Schumacher, Delbrück scattering, Radiation Physics and Chemistry 56 (1) (1999) 101–111.

[100] R. Rüffer, Nuclear resonance scattering, Comptes Rendus Physique 9 (5) (2008) 595–607, synchrotron x-rays and condensed matter.

[101] D. Rao, R. Cesareo, G. Gigante, Atomic rayleigh scattering cross-sections and the associated anomalous dispersion in the x-ray regions, Eur. Phys. J. D 7 (1999).

[102] H. Bethe, W. Heitler, P. A. M. Dirac, On the stopping of fast particles and on the creation of positive electrons, Proceedings of the Royal Society of London. Series A, Containing Papers of a Mathematical and Physical Character 146 (856) (1934) 83–112.

[103] I. Øverbø, K. J. Mork, H. A. Olsen, Pair production by photons: Exact calculation for unscreened atomic field, Phys. Rev. A 8 (1973) 668–685.

[104] H. Olsen, L. C. Maximon, H. Wergeland, Theory of high-energy bremsstrahlung and pair production in a screened field, Phys. Rev. 106 (1957) 27–46.

[105] K. Mork, H. Olsen, Radiative corrections. i. high-energy bremsstrahlung and pair production, Phys. Rev. 140 (1965) B1661–B1674.

[106] J. H. Scofield, Theoretical photoionization cross sections from 1 to 1500 kev.

[107] J. H. Hubbell, H. A. Gimm, I. O/verbo/, Pair, Triplet, and Total Atomic Cross Sections (and Mass Attenuation Coefficients) for 1 MeV-100 GeV Photons in Elements Z=1 to 100, Journal of Physical and Chemical Reference Data 9 (4) (1980) 1023–1148.

[108] D. E. Cullen, J. H. Hubbell, L. Kissel, Epdl97: the evaluated photo data library '97 version (9 1997).

[109] U. Fano, J. R. Albers, K. W. McVoy, Sauter theory of the photoelectric effect, Physical Review (U.S.) Superseded in part by Phys. Rev. A, Phys. Rev. B: Solid State, Phys. Rev. C, and Phys. Rev. D.

[110] J. Hubbell, S. Seltzer, Cross section data for electron–positron pair production by photons: a status report, Nuclear Instruments and Methods in Physics Research Section B: Beam Interactions with Materials and Atoms 213 (2004) 1–9, 5th Topical Meeting on Industrial Radiation and Radioisotope Measurement Applications.

[111] W. Heitler, The quantum theory of radiation, Courier Corporation, 1984.

[112] A. Puglisi, Ab-initio study of x-ray spectroscopy of molecular ions, Ph.D. thesis (09 2017).

[113] S. Goudsmit, J. L. Saunderson, Multiple scattering of electrons, Phys. Rev. 57 (1940) 24–29.

[114] U. Fano, Inelastic collisions and the molière theory of multiple scattering, Phys. Rev. 93 (1954) 117–120.

[115] H. W. Lewis, Multiple scattering in an infinite medium, Phys. Rev. 78 (1950) 526–529.

[116] J. Baró, J. Sempau, J. Fernández-Varea, F. Salvat, Penelope: An algorithm for monte carlo simulation of the penetration and energy loss of electrons and positrons in matter, Nuclear Instruments and Methods in Physics Research Section B: Beam Interactions with Materials and Atoms 100 (1) (1995) 31–46.

[117] Geant4 collaboration, guide for physics lists.
URL `https://geant4-userdoc.web.cern.ch/UsersGuides/PhysicsListGuide/html/index.html`

[118] G. Battistoni, T. Boehlen, F. Cerutti, P. W. Chin, L. S. Esposito, A. Fasso, A. Ferrari, A. Lechner, A. Empl, A. Mairani, A. Mereghetti, P. G. Ortega, J. Ranft, S. Roesler, P. R. Sala, V. Vlachoudis, G. Smirnov, Overview of the fluka code, Annals of Nuclear Energy 82 (2015) 10.

[119] I. Kawrakow, E. Mainegra-Hing, D. W. O. Rogers, F. Tessier, B. R. B. Walters, The egsnrc code system: Monte carlo simulation of electron and photon transport.
URL `https://nrc-cnrc.github.io/EGSnrc/doc/pirs701-egsnrc.pdf`

[120] F. Salvat, PENELOPE-2018: A Code System for Monte Carlo Simulation of Electron and Photon Transport.
URL `https://www.oecd-nea.org/upload/docs/application/pdf/2020-10/penelope-2018__a_code_system_for_monte_carlo_simulation_of_electron_and_photon_transport.pdf`

[121] J. A. Kulesza, T. R. Adams, J. C. Armstrong, S. R. Bolding, et al., MCNP Code Version 6.3.0 Theory and User Manual.
URL `https://mcnp.lanl.gov/pdf_files/TechReport_2022_LANL_LA-UR-22-30006Rev.1_KuleszaAdamsEtAl.pdf`

[122] E. Brun, F. Damian, C. M. Diop, E. Dumonteil, F. X. Hugot, C. Jouanne, Y. K. Lee, F. Malvagi, A. Mazzolo, O. Petit, J. C. Trama, T. Visonneau, A. Zoia, Tripoli-

4, CEA, EDF and AREVA reference Monte Carlo code, Annals of Nuclear Energy 82 (2015) 151.

[123] J. Leppanen, M. Pusa, T. Viitanen, V. Valtavirta, T. Kaltiaisenaho, The Serpent Monte Carlo code: Status, development and applications in 2013, Annals of Nuclear Energy 82 (2015) 142.

[124] P. Hovington, D. Drouin, R. Gauvin, CASINO: A New Monte Carlo Code in C Language for Electron Beam Interaction — Part I: Description of the Program, Scanning 19 (1997) 1.

[125] J. F. Ziegler, SRIM-2003, Nucl. Instrum. Meth. Phys. Res. B 219-220 (2004) 1027.

[126] Geant4 community, Geant4, a simulation toolkit, available on line.
URL `https://geant4.web.cern.ch/about/`

[127] M. Asai, Introduction to geant4, Hiroshima Institute of Technology, Hiroshima, Japan (2000).

[128] Geant4 Collaboration, Book For Application Developers, Sep 27, 2017.

[129] S. Guatelli, D. Cutajar, B. Oborn, A. Rosenfeld, Introduction to the geant4 simulation toolkit, AIP Conference Proceedings 1345 (2011) 303–322.

[130] Nist, national institute of standards and technologies, estar: stopping power and range for electrons.
URL `https://physics.nist.gov/PhysRefData/Star/Text/ESTAR.html`

[131] M. J. Berger, Estar pstar astar, stopping power and range of electrons, protons, alpha (Jun 1995).

[132] G. J. Lockwood, L. E. Ruggles, G. H. Miller, J. A. Halbleib, Calorimetric measurement of electron energy deposition in extended media. theory vs experiment.

[133] G. J. Lockwood, G. H. Miller, J. A. Halbleib, Absolute measurement of low energy electron deposition profile in semi- infinite geometries, IEEE Trans. Nucl. Sci., v. NS-20, no. 6, pp. 326-330 (12 1973).

[134] G. J. Lockwood, L. E. Ruggles, G. H. Miller, J. Halbleib, Electron energy and charge albedos-calorimetric measurement vs monte carlo theory, Tech. rep., Sandia National Lab.(SNL-NM), Albuquerque, NM (United States) (1981).

[135] G. J. Lockwood, G. H. Miller, J. A. Halbleib, Simultaneous integral measurement of electron energy and charge albedos, IEEE Transactions on Nuclear Science 22 (6) (1975) 2537–2542.

[136] G. J. Lockwood, G. H. Miller, J. A. Halbleib, Electron energy deposition in multilayer geometries, IEEE Transactions on Nuclear Science 23 (6) (1976) 1862–1866.

[137] J. A. Halbleib, T. A. Mehlhorn, ITS: The Integrated TIGER Series of coupled electron/photon Monte Carlo transport codes (Nov. 1984).

[138] A. Lechner, M. G. Pia, M. Sudhakar, Validation of geant4 low energy electromagnetic processes against precision measurements of electron energy deposition, IEEE Transactions on Nuclear Science 56 (2) (2009) 398–416.

[139] M. Batic, G. Hoff, M. G. Pia, P. Saracco, G. Weidenspointner, Validation of geant4 simulation of electron energy deposition, IEEE Transactions on Nuclear Science 60 (4) (2013) 2934–2957.

[140] A. Bednyakov, On the molière theory of multiple scattering of charged particles (1947–1948) and its critique in subsequent years, Physics of Particles and Nuclei 45 (2014) 991–999.

[141] T. Basaglia, M. C. Han, G. Hoff, C. H. Kim, S. H. Kim, M. Grazia Pia, P. Saracco, Quantitative test of the evolution of Geant4 electron backscattering simulation, IEEE Trans. Nucl. Sci. 63 (2016) 2849.

[142] H. Bruining, Physics and Applications of Secondary Electron Emission, McGraw-Hill, New York, 1954.

[143] A. J. Dekker, Secondary Electron Emission (solid State Physics vol 6), Academic, New York, 1958.

[144] H. Seiler, Secondary electron emission in the scanning electron microscope, J. Appl. Phys. 54 (1983) R1.

[145] P. Tolias, On secondary electron emission and its semi-empirical description, Plasma Phys. Control. Fusion 56 (2014) 123002.

[146] H. Niedrig, Electron backscattering from thin films, J. Appl. Phys. 53 (1982) R15.

[147] P. Tolias, On electron backscattering from dust grains in fusion plasmas, Plasma Phys. Control. Fusion 56 (2014) 045003.

[148] L. A. MacColl, Numerical calculations of the reflection of electrons by metals, Phys. Rev. 56 (1939) 699.

[149] I. H. Khan, J. P. Hobson, R. A. Armstrong, Reflection and diffraction of slow electrons from single crystals of tungsten, Phys. Rev. 129 (1963) 1513.

[150] P. Tolias, Low energy electron reflection from tungsten surfaces (2016). arXiv:1601.02047.

[151] I. M. Bronshtein, B. S. Fraiman, VTORICHNAYA ELEKTRONNAYA EMISSIYA. (Secondary Electron Emission), Nauka, Moscow, 1969.

[152] P. Tolias, M. Komm, S. Ratynskaia, A. Podolnik, Origin and nature of the emissive sheath surrounding hot tungsten tokamak surfaces, Nucl. Mater. Energy 25 (2020) 100818.

[153] L. Reimer, Scanning Electron Microscopy: Physics of Image Formation and Microanalysis, Springer, Berlin, 1998.

[154] C. G. H. El-Gomati, M. M. Walker, Toward Quantitative Scanning Electron Microscopy (Advances in Imaging and Electron Physics, Vol 183), Elsevier, Amsterdam, 2014.

[155] M. El Gomati, C. Walker, A. Assa'd, M. Zadražil, Theory experiment comparison of the electron backscattering factor from solids at low electron energy (250–5,000 ev), Scanning: The Journal of Scanning Microscopies 30 (1) (2008) 2–15.

[156] H.-J. Hunger, L. Küchler, Measurements of the electron backscattering coefficient for quantitative epma in the energy range of 4 to 40 kev, physica status solidi (a) 56 (1) K45–K48.

[157] D. C. Joy, A database on electron-solid interactions, Scanning 17 (1995) 270.

[158] L. Reimer, C. Tollkamp, Measuring the backscattering coefficient and secondary electron yield inside a scanning electron microscope, Scanning 3 (1980) 35.

[159] H. Drescher, L. Reimer, M. Seidel, Backscattering and secondary electron emission of 1o-1oo kev electrons and correlations to scanning electron microscopy, Z. Angew. Physik 29 (1970) 331.

[160] V. E. Cosslett, R. N. Thomas, Multiple scattering of 5 -30 kev electrons in evaporated metal films III: Backscattering and absorption, Br. J. Appl. Phys. 16 (1965) 779.

[161] G. Neubert, S. Rogaschewski, Backscattering coefficient measurements of 15 to 60 kev electrons for solids at various angles of incidence, physica status solidi (a) 59 (1) (1980) 35–41.

[162] T. Tabata, Backscattering of electrons from 3.2 to 14 mev, Physical Review 162 (2) (1967) 336.

[163] L. Yang, A. Hussain, S. Mao, B. Da, K. Tokesi, Z. J. Ding, Electron backscattering coefficients of molybdenum and tungsten based on the Monte Carlo simulations, J. Nucl. Mater. 553 (2021) 153042.

[164] H. Chen, Y. Zou, S. Mao, M. S. S. Khan, K. Tokesi, Z. J. Ding, Influence of energy loss function to the Monte Carlo simulated electron backscattering coefficient, Sci. Rep. 12 (2022) 18201.

[165] Private communication with E.M. Hollmann and M. Beidler, 2023.

[166] K. Paschalidis, S. Ratynskaia, F. Lucco Castello, P. Tolias, Melt dynamics with MEMENTO – code development and numerical benchmarks, Nucl. Mater. Energy [Submitted] (2023).

[167] S. Ratynskaia, K. Paschalidis, P. Tolias, K. Krieger, et al., Experiments and modelling on ASDEX Upgrade and WEST in support of tool development for tokamak reactor armour melting assessments, Nucl. Mater. Energy 33 (2022) 101303.

[168] E. Thorén, S. Ratynskaia, P. Tolias, R. A. Pitts, the JET contributors, the EUROfusion MST1 team, The MEMOS-U code description of macroscopic melt dynamics in fusion devices, Plasma Physics and Controlled Fusion 63 (3) (2021) 035021.

[169] E. Thorén, P. Tolias, S. Ratynskaia, R. Pitts, K. Krieger, Self-consistent description of the replacement current driving melt layer motion in fusion devices, Nuclear Fusion 58 (07 2018).

[170] Y. Corre, A. Marie-hélène, A. Durif, J. Gaspar, K. Krieger, T. Loewenhoff, M. Richou, S. Ratynskaia, Q. Tichit, Y. Anquetin, R. Dejarnac, M. Diez, L. Dubus, M. Firdaouss, J. Gerardin, A. Grosjean, J. P. Gunn, T. Loarer, C. Martin, K. Paschalidis, P. Maget, E. Tsitrone, M. Wirtz, Testing of iter-like plasma facing units in the west tokamak: progress in understanding heat loading and damage mechanisms, Nucl. Mater. Energy [Submitted] (2023).

[171] Y. Corre, A. Grosjean, J. Gunn, K. Krieger, S. Ratynskaia, O. Skalli-Fettachi, C. Bourdelle, S. Brezinsek, V. Bruno, N. Chanet, J. Coenen, X. Courtois, R. Dejarnac, E. Delmas, L. Delpech, C. Desgranges, M. Diez, L. Dubus, A. Durif, A. Ekedahl, N. Fedorczak, M. Firdaouss, J.-L. Gardarein, J. Gaspar, J. Gerardin, C. Guillemaut, M. Houry, T. Loarer, P. Maget, P. Mandelbaum, R. Mitteau, M. Missirlian, P. Moreau, R. Nouailletas, E. Nardon, C. Pocheau, A. Podolnik, P. Reilhac, X. Regal-Mezin, C. Reux, M. Richou, F. Rigollet, J.-L. Schwob, E. Thorén, P. Tolias, E. Tsitrone, The WEST Team, Sustained W-melting experiments on actively cooled ITER-like plasma facing unit in WEST, Phys. Scr. 96 (2021) 124057.

[172] K. Krieger, B. Sieglin, M. Balden, J. W. Coenen, B. Göths, F. Laggner, P. de Marne, G. F. Matthews, D. Nille, V. Rohde, R. Dejarnac, M. Faitsch, L. Giannone, A. Herrmann, J. Horacek, M. Komm, R. A. Pitts, S. Ratynskaia, E. Thorén, P. Tolias, The ASDEX-Upgrade Team, The EUROfusion MST1 Team, Investigation of transient melting of tungsten by ELMs in ASDEX Upgrade, Phys. Scr. T170 (2017) 014030.

[173] K. Krieger, M. Balden, J. W. Coenen, F. Laggner, G. F. Matthews, D. Nille, V. Rohde, B. Sieglin, L. Giannone, B. Göths, A. Herrmann, P. de Marne, R. A. Pitts, S. Potzel, P. Vondracek, The ASDEX-Upgrade Team, The EUROfusion MST1 Team, Experiments on transient melting of tungsten by ELMs in ASDEX Upgrade, Nucl. Fusion 58 (2018) 026024.

[174] J. W. Coenen, G. Arnoux, B. Bazylev, G. F. Matthews, A. Autricque, I. Balboa, M. Clever, R. Dejarnac, I. Coffey, Y. Corre, S. Devaux, L. Frassinetti, E. Gauthier, J. Horacek, S. Jachmich, M. Komm, M. Knaup, K. Krieger, S. Marsen, A. Meigs, P. Mertens, R. A. Pitts, T. Puetterich, M. Rack, M. Stamp, G. Sergienko, P. Tamain, V. Thompson, the JET-EFDA Contributors, ELM-induced transient tungsten melting in the JET divertor, Nucl. Fusion 55 (2015) 023010.

[175] I. Jepu, G. F. Matthews, A. Widdowson, M. Rubel, E. Fortuna-Zaleśna, J. Zdunek, P. Petersson, V. Thompson, P. Dinca, C. Porosnicu, P. Coad, K. Heinola, N. Catarino, O. G. Pompilian, C. P. Lungu, The JET Contributors, Beryllium melting and erosion on the upper dump plates in JET during three ITER-like wall campaigns, Nucl Fusion 59 (2019) 086009.

[176] H. Bolt, V. Barabash, W. Krauss, J. Linke, R. Neu, S. Suzuki, N. Yoshida, ASDEX Upgrade Team, Materials for the plasma-facing components of fusion reactors, Journal of Nuclear Materials 329-333 (2004) 66–73, proceedings of the 11th International Conference on Fusion Reactor Materials (ICFRM-11).

List of Figures

List of Tables

List of Symbols

Variable	Description	SI unit
A	mass number	-
c	light's speed	m/s
m_e	electron's mass	kg
n_e	electron's density	m^{-3}
e	electron's charge	C
E	kinetic energy	J
Z	atomic number	-
I	ionization energy	J
σ	cross section	m^2
λ_e	electron's De Broglie wavelength	m
η	backscattering yield	-
b_2	sample's top surface	m
$\dot{x}_{\mathrm{vap}}$	erosion rate	m/s
c_{p}	heat capacity	$\mathrm{J\ kg^{-1}K^{-1}}$
ρ_{m}	mass density	$\mathrm{kg/m^3}$
k	thermal conductivity	$\mathrm{Wm^{-1}K^{-1}}$
q_{vap}	vaporization cooling flux	$\mathrm{W/m^2}$
q_{rad}	radiation cooling flux	$\mathrm{W/m^2}$

Acknowledgements

A major thank goes to my supervisors at KTH, Prof. Svetlana Ratynskaia and Dr. Panagiotis Tolias. Without their leadership, rigour and extremely wide experience this project could not arrive to an end. They guided me in this process of personal and scientific growth like the wisest mentors do. Despite the hard work required, they were always able to maintain a joyful and charming climate inside the office, making me enthusiastic and passionate. I would like to mention also PhD. student Konstantinos Paschalidis, my future colleague, for his help and patience when explaining the MEMENTO code and for taking care of the MEMENTO runs presented in this thesis. I hope to give it back to you in the future years that will see us working side by side.

A special gratitude goes to Prof. Richard Pitts, Leader of the Experiments and Plasma Operation Section of ITER. During these months of work, he offered me the unique occasion to visit the ITER site for a presentation of my research results. He also guided me in a tour of the ITER construction site, fascinating me with his knowledge and erudition.

I have had pleasure to interact with Dr. Eric Hollmann, associate researcher in the Center for Energy Research, University of California and other colleagues at DIII-D and would like to thank them for the opportunity to work together on this excellent experiment on runaway electrons in DIII-D and for providing us the necessary empirical input.

I am also grateful to my Italian supervisor, professor Maffini, for his support and collaboration.

Finally, the city of Stockholm needs a special mention. An infinite list of memories belongs to the last 12 months, including those special people that made my experience the best I could ask for. Last but not least, I owe my family the biggest gratitude. Despite not seeing me for almost a year, they have always been supportive, encouraging me in every step, small or big, I walk through.